Non-volatile programmable photonics based on phase-change materials

Zhuoran Fang

A dissertation

submitted in partial fulfillment of the

requirements for the degree of

Doctor of Philosophy

University of Washington

2023

Reading committee:

Arka Majumdar, Chair

Mo Li

Sajjad Moazeni

Program Authorized to Offer Degree:

Electrical and Computer Engineering

University of Washington

Abstract

Non-volatile programmable photonics based on phase-change materials

Zhuoran Fang

Chair of the Supervisory Committee:
Arka Majumdar
Department of Electrical and Computer Engineering

Programmable photonics can enable a plethora of exciting applications from next-generation optical interconnects to quantum information technologies. Conventionally, photonic systems are tuned by mechanisms such as thermos-optic effect, free carrier dispersion, electro-optic effect, or mechanical movement. Although these physical effects allow either fast (> 100GHz) or large contrast (> 60dB) switching, they are not optimal for programmability which does not require frequent switching. Phase-change materials (PCMs) can offer an ideal solution thanks to their reversible switching, large index contrast, and non-volatile behavior, enabling a truly 'set-and-forget' switch element with no static power consumption. Recent years, we have indeed witnessed the fast adoption of PCMs in programmable photonic systems, from photonic integrated circuits (PICs) to meta-optics. Despite the tremendous progress in the field, a few remaining challenges must be addressed before the technology can be scalable and ultimately commercialized. For example, the high optical loss of the traditional PCMs, such as $Ge_2Sb_2Te_5$ (GST), is prohibitive for large-scale PICs. Secondly, the energy required to electrically switch PCMs remains to be high (~tens of nano-joules), and

the device footprint is still large (> 64μm). Lastly, so far there has not been an ideal solution towards non-volatile phase-only control in the free-space due to the high loss of the PCMs and microheaters. In this dissertation, we aim to circumvent these limitations. First, we demonstrated non-volatile phase modulation ($\Delta\phi\sim0.17\pi$) with near zero insertion loss in both Si and SiN integrated photonics using a low-loss PCMs Sb_2S_3. Through device engineering, an ultra-compact (33μm coupling length) directional coupler switch was realized based on Sb_2Se_3. Individual control of the phase and coupling in racetrack resonator was achieved. We further showed that ultra-low switching energy down to 8.7±1.4aJ/nm^3 can be achieved using graphene microheaters for tuning the PCMs with excellent endurance over 1,000 cycles. Finally, leveraging a high-*Q* metasurface, we demonstrated non-volatile phase-only modulation of free-space light with ~0.2π phase shift and near zero change in intensity. Our work represents a crucial step in the development of disruptive non-volatile photonic technologies based on PCMs.

Acknowledgement

As my PhD journey comes to an end soon, I would like to express my gratitude to people who have helped and given me guidance over the 4+ years. The first person I would like to thank is my advisor, Arka Majumdar. Thank you for being such a great mentor and friend. You show me how to do proper scientific research and you always push me to work harder. Your work ethics and passion for research inspired me when I first joined as a new PhD student and will continue to influence me in my future career. Most importantly, you truly care about every student's goal and are happy to provide any support when needed. Thank you for your endless support in my research and career endeavor! Secondly, I would like to thank my parents - my mother Rong Yu and my father Chuangxin Fang – for their faith in me to succeed in my education and career. Despite some disagreement at the beginning, I really appreciate that you supported my decision to do a PhD in a foreign country and pursue my dream. What I have become may not be what you hope for, but I am very grateful that you believe in my determination and celebrate my research achievements! Thirdly, I would like to thank my fiancé Han Li who accompanied me throughout my entire PhD and listen patiently to my complaint after work when the experiment did not go well. You are my greatest support outside research! Lastly, I would like to thank my fellow PhD teammates for their kind help and guidance in my research, study, and job searching. These include but are not limited to Jiajiu Zheng, Rui Chen, Johannes Fröch, Quentin Tanguy, Abhi Saxena, Max Zhelyeznyakov, Forrest Miller, and Elyas Bayati etc.

Table of Contents

List of Figures

the SET and RESET operation as red and blue shift of the resonance dip. **e** I-V curve (red) and power (blue) during a 0-1V DC sweep that triggered the SET operation. **f** Temperature distribution under stationary heating at 1V (top) and after 200ns pulse at 6V (bottom). Scale bar is 500nm. *Page 23*

Figure 2. 5: Thermo-optic effect of SbS on SOI. a Spectral shift caused by raising the temperature from 297K to 317K of microring capped with 10µm-long, 66nm-thick SbS. **b** Extracted thermo-optic coefficient of aSbS and cSbS compared with silicon. Page 31

Figure 2. 6: SbS on SiN microrings in near visible wavelength. a Simulated fundamental quasi-TE mode profiles of 20nm aSbS/cSbS on SiN hybrid waveguide at 750nm. Note here that the SbS is only place on top of the waveguide. **b** Transmission spectrum of SiN ring resonators capped with 5µm aSbS and cSbS near 750nm.

Figure 3. 1: Design of the directional coupler switch. a Schematic of the directional coupler switch. Inset below shows the cross-section of the device. **b** Coupling length against gap for aSb_2Se_3 and cSb_2Se_3-loaded hybrid waveguide. The ratio is the coupling length of aSb_2Se_3 over that of cSb_2Se_3. **c** FDTD simulated electric field intensity of the directional coupler in cross (amorphous) and bar (crystalline) states. **d** FDTD simulated transmission spectrum of the directional coupler in cross (top) and bar (bottom) states. Page 42

Figure 3. 2: Coupled mode simulation of bare waveguide and hybrid waveguide. a Simulated effective index of the bare Si, aSb_2Se_3-loaded, and cSb_2Se_3-loaded waveguides. The dash line indicates where the phase matching condition is satisfied between the aSb_2Se_3-loaded waveguide (w_h=462nm) and bare Si waveguide (w=500nm). **b** Simulated fundamental quasi-TE supermodes of aSb_2Se_3-loaded waveguide (top) and cSb_2Se_3-loaded waveguide (bottom) next to a Si waveguide. w_h is 462nm and w is 500nm. Gap is 374nm. Page 43

Figure 3. 3: Electrical control of the directional coupler switch. a Optica micrograph (top) and SEM (bottom) of the fabricated switch. **b** Experimental transmission spectrum of the reversible switching between cross and bar states. 3.6V, 1.5ms width, 0.5ms trailing edge is used for SET. 8.2V, 400ns width, 8ns trailing edge is used for RESET. The spectrum is normalized by the spectrum of a

Figure 4. 1: A graphene-PCM reconfigurable silicon photonic platform. a Schematic of the device structure. SLG stands for single-layer graphene. S (G), signal (ground) electrode. **b** Layered structure of the device. Note that an additional 10nm sputtered SiO_2 is used to encapsulate the Sb_2Se_3 which is not shown in the Figure. Such SiO_2 capping is not used for GST. **c** Optical micrograph of the waveguide switch. **d** False color SEM of the waveguide area where the GST is patterned. The SLG area is enclosed by the black dashed lines. **e** Operating principle of the device. T_l denotes the melting temperature and T_x denotes the crystallization temperature. *n* is the refractive index and *k* is the extinction coefficient. Page 56

Figure 4. 2: Graphene-assisted broadband waveguide switch based on GST. a Reversible switching of GST using graphene heater on SOI waveguide. The switching conditions are 3V, 100μs pulse width, 120μs trailing edge for SET and 5V, 400ns pulse width, 8ns trailing edge for RESET. 8 consecutive cycles are plotted where the shaded area indicates the standard deviation between the cycles and the solid line indicates the average. The device spectrum is normalized with the spectrum of a bare waveguide. **b** Cyclability of the switch for 1,500 switching events. The pulse conditions are the same as in **a**. Each pulse is temporally separated by 2s to ensure long thermal relaxation. The transmission is normalized with the transmission of a bare waveguide. aGST (cGST), amorphous (crystalline) GST. Page 58

Figure 4. 3: Graphene sheet resistance and I-V curve. a Device schematic for characterizing the SLG sheet resistance. *W* is the SLG width while *L* is the SLG length. **b** Resistance of SLG of different widths against lengths. The resistance is measured at DC applied bias of 0.1mV. **c** The extracted sheet resistance and contact resistance of SLG against the width. **d** I-V curve of the SLG-GST device tested in the main text from 2V to 5.2V. Page 61

Figure 4. 4: Graphene-assisted phase shifter based on Sb2Se3 in a microring. a Schematic of the graphene-Sb_2Se_3 phase shifter in a microring. **b** Optical micrograph of the microring resonator integrated with a phase shifter. **c** False-color SEM of the microring area where the Sb_2Se_3 is patterned. The graphene area is enclosed by the black dashed lines. **d** Reversible switching of Sb_2Se_3 using

graphene heater on microrings. The switching conditions are 4V, 100μs pulse width, 120μs trailing edge for SET and 6.8V, 400ns pulse width, 8ns trailing edge for RESET. Three consecutive cycles are plotted where the shaded area indicates the standard deviation between the cycles and the solid line indicate the average. The spectrum is normalized with the spectrum of a bare waveguide. **e** Cyclability of the switch for 2000 switching events. The switching conditions are 4V, 100μs pulse width, 120μs trailing edge for SET and 6.4V, 400ns pulse width, 8ns trailing edge for RESET. Each pulse is temporally separated by 2s to ensure long thermal relaxation. The transmission is normalized with the transmission of a bare waveguide. The data is filtered by a 50-point moving average to reduce fluctuation caused by thermal noises. Page 64

Figure 4. 5: Optical mode and heat transfer simulations of the SLG-PCM photonic switch. a Simulated fundamental TE mode profiles of 23nm GST (left panel) and 30nm Sb_2Se_3 (right panel) on planarized SOI waveguides at 1550nm. The optical constants of GST and Sb_2Se_3 at 1550nm are extracted from cutback measurements using microring resonators. The white dashed lines indicate the presence of SLG in the simulation. The red dashed lines indicate the boundaries between the device layer (220nm Si) and the buried oxide. **b** Simulated temperature variation with time under the measured current for amorphization (top) and crystallization (bottom). The red curves indicate the injecting current while the blue curves indicate the temperature of GST. **c** Simulated temperature distribution at 400ns under injecting current of 2.78mA (top) and at 100μs under current of 1.89mA (bottom). Page 67

Figure 4. 6: Extracting the insertion loss and effective index change of Sb2Se3 using microrings. **a** SEM showing the Sb_2Se_3 material is patterned on top the silicon microring resonators. **b** AFM measured cross-section of the waveguide with 20nm Sb_2Se_3 on top. **c** The extracted insertion loss of the Sb_2Se_3 in both the amorphous and crystalline states against the length. **d** The extracted spectral shift caused by the Sb_2Se_3 phase change against the length. Page 68

Figure 4. 7: Comparison to other nonvolatile electrically reconfigurable photonic platforms. Comparison of number of cycles demonstrated versus the programming energy density for doped

Si[28], [58], PIN[27], TCOs[32], [62], [63], and graphene heaters[52]. The reference number is denoted inside the parenthesis. 'Not PICs' indicates that the reversible switching of PCM was not achieved on a PIC platform. The diamond markers indicate that the heaters are compatible with Si_3N_4. The no-fill diamond markers indicate the programming energy calculated by considering only the graphene sheet resistance, also denoted by 'R_s'. The grey shaded area includes only the doped Si heaters that are compatible with SOI only. The red shaded areas include only the graphene heaters. 'GST', 'GSST', and 'SbSe' in the legend denote $Ge_2Sb_2Te_5$, $Ge_2Sb_2Se_4Te$, and Sb_2Se_3 respectively. The * in the legend indicates that the numbers are quoted for microrings. Page 71

Figure 4. 8: Quasi-continuous phase modulation using the graphene-Sb2Se3 phase shifter. a Quasi-continuous tuning of microring resonance by step amorphization. The SET conditions are 4V, 100μs pulse width, 120μs trailing edge. For RESET, the amplitude is increased monotonically from 5.5V to 6.4V and the pulse width and trailing edge are fixed at 400ns and 8ns. **b** Temporal trace of a continuous programming iteration with a monotonically increasing RESET pulse amplitude from 5.5V to 6.9V followed by a SET pulse. Eight transmission levels are clearly resolved. The pulse width and trailing edge of the RESET pulse are fixed at 400ns and 8ns. The SET conditions are the same as in **a**. **c** Change in phase shift ($\Delta\varphi$) with respect to the programming energy. 14 phase levels can be resolved where the phase shift increases linearly with the programming energy. **d** Change in transmission caused by the phase shift with respect to the programming energy. 14 transmission levels can be resolved. The transmission contrast increases linearly with the programming energy, matching very well with **c**. Page 73

Figure 4. 9: Fabrication flow schematics of SLG-PCM reconfigurable silicon photonic platform. a Fabrication process flow of the SLG-PCM photonic switch. **b** The cross-section of the final fabricated device. Page 76

Figure 4. 10: Temporal trace of SLG-PCM photonic switch and phase shifter. a Temporal trace of SLG-GST photonic switch for ten reversible switching events. The switching conditions are 3V, 100μs pulse width, 120μs trailing edge for SET and 5V, 400ns pulse width, 8ns trailing edge for

RESET. **b** Temporal trace of SLG-Sb_2Se_3 phase shifter for ten reversible switching events. The switching conditions are 4V, 100μs pulse width, 120μs trailing edge for SET and 6.4V, 400ns pulse width, 8ns trailing edge for RESET. A two-second interval is used in **a** and **b** between consecutive switching events. Page 77

Figure 4. 11: Real-time voltage of the applied electrical pulse and the corresponding change in transmission for a crystallization and **b** amorphization. Page 78

Figure 4. 12: Multilevel operation in waveguide switches and reproducibility. Page 79

Figure 5. 1: High-Q silicon diatomic metasurfaces. a Schematics of the high contrast gratings (top) and diatomic gratings (bottom). Λ_{HCG} and Λ are the periods of the high contrast gratings and diatomic gratings respectively. The spacing between the gratings are denoted as a, a_1, and a_2. w is the grating width. **b** Simulated transmission spectrum of the high contrast gratings (blue) and diatomic gratings (orange) under normal incident TM polarized light. Silicon thickness is 220nm, Λ=900nm and Γ=0.7. Inset: Experimental spectrum of a resonance fitted by Fano equation, Λ=950nm and Γ=0.7. **c** SEM of fabricated silicon diatomic gratings. **d** Experimental spectrum of diatomic gratings with different periods from 900nm to 1000nm, where δ=0.05 and Γ=0.7. Page 86

Figure 5. 2: Electric field amplitude of the high contrast gratings vs. diatomic gratings. a Electric field amplitude of the high contrast gratings when δ is zero. **b** Electric field amplitude of the diatomic gratings when δ=0.05. Structures in **a** and **b** consist of 220nm thick silicon gratings (Λ=900nm and Γ=0.7), cladded with 20nm aSb_2Se_3 and capped with 40nm Al_2O_3. The gratings sit on 2μm thick SiO_2. The unit for x and y axes is μm. Page 87

Figure 5. 3: A nonvolatile electrically reconfigurable metasurface based on Sb2Se3. a Schematic of the transmissive tunable diatomic metasurface based on Sb_2Se_3. S (G), signal (ground) electrode. **b** The optical setup for probing the metasurface in transmission along with the devices under test wire bonded to a customized PCB. AFG is arbitrary function generator. **c** The schematic of the tunable

metasurface cross section. **d** Optical micrograph of a single metasurface pixel on the chip under test. Page 88

Figure 5. 4: Reversible switching of the diatomic metasurface and nonvolatile phase-only modulation. a Simulated spectral and phase shift caused by 20nm Sb_2Se_3. $\Delta\lambda$ is the wavelength shift of the resonance dip. The diatomic metasurface is designed to be Λ=900nm, Γ=0.7, and δ=0.05. a(c)Sb_2Se_3, amorphous(crystalline) Sb_2Se_3. **b** Measured reversible switching of the diatomic resonance. The switching conditions are 3.6V, 50μs pulse width, 30μs trailing edge for SET and 11.6V, 1μs pulse width, 8ns trailing edge for RESET. Three consecutive cycles are plotted where the shaded area indicates the standard deviation between the cycles and the solid line indicate the average. The spectrum is normalized with the spectrum of bare SiO_2 on silicon. **c** Phase shift ($\Delta\phi$, red) and transmission contrast ($\Delta T\%$, blue) between the two optical states extracted from simulation (top) and experiment (bottom). The phase is measured at 11 different wavelengths with 1nm spacing and averaged over three switching cycles. The standard deviation over the cycles is shown by the error bars. **d** Cyclability of the tunable metasurface for 1,000 switching events. The switching conditions are 3.6V, 50μs pulse width, 30μs trailing edge for SET and 11.6V, 600ns pulse width, 8ns trailing edge for RESET. Each pulse is temporally separated by 2s to ensure long thermal relaxation. The data is filtered by a two-point moving average to reduce fluctuation caused by thermal and mechanical noises. Page 90

Figure 5. 5: Fitting of the diatomic resonance by Fano equations when Sb2Se3 is in amorphous (blue) and crystalline (red) states. Page 92

Figure 5. 6: Spectrum of the same diatomic gratings cladded with 20nm GST. Page 93

Figure 5. 7: Temporal response of switching the metasurface. a Switching the metasurface with 2s interval without excitation, indicating non-volatile tuning. **b** Optical micrographs of the metasurface pixel before and after the endurance test. No damage is observed. Page 93

Figure 5. 8: Schematic of the experimental setup. a Optical setup for measuring switching of metasurface spectrum. **b** Optical setup for characterizing the device endurance and imaging the far field of the gratings. **c** Optical setup for measuring the optical phase shift caused by the metasurface switching. Page 95

List of Tables

Chapter 1. Introduction

1.1 Background

Programmability is an essential feature in modern-day photonic systems, and is crucial to enable technologies including next-generation data centers[1], optical computing[2], quantum information processing[3], and light detection and ranging[4], [5]. Such programmability is generally achieved by traditional modulation methods, such as thermo-optic (TO) effect, free-carrier dispersion, electro-optic (EO) effect, and mechanical tuning. These physical effects are, however, more suitable for modulating light, but not ideal for programmability. This is because modulators are optimized for high-speed and low-power operation, but programmability only requires infrequent switching. Although TO effect and micro-electro-mechanical-systems (MEMS) can offer slow but large extinction ratio (>60dB) tuning, their large static power consumption (>10 mW) and high driving voltage (>20V) are prohibitive to future photonic systems. For programmable photonic applications with infrequent switching, the power and latency of individual switching event are less important than zero static energy holding of the programmed states. Hence, a "set-and-forget" reconfiguration will be highly desirable for applications such as routing photons in photonic integrated circuits (PICs), setting phase masks in spatial light modulators (SLMs), or trimming photonic resonators to the same resonance frequency. Chalcogenide-based phase-change materials (PCMs), exemplified by $Ge_2Sb_2Te_5$ (GST), present an ideal solution to the above scenarios thanks to their reversible and bistable phase transition, multilevel operation, and large refractive index contrast ($\Delta n \geq 1$). They can also be programmed in a fast time scale ($\sim\mu$s to ns), and moderate switching energy (pJ to fJ) [6]–[8]. Despite recent progress in PCM-based photonics, several outstanding challenges remain:

(1) High insertion loss: Photonic systems based on traditional PCMs, such as GST, suffer from large insertion loss (a few dBs) so are not compatible with large-scale PICs.
(2) Large device footprint: While device engineering can reduce the insertion loss to below 2dB, it inevitably increases the footprint of the switch (> 64μm).
(3) High switching energy: Although pico-joules switching energy has been demonstrated via optical switching, electrical switching of PCMs using doped silicon or ITO microheaters still consumes tens of nano-joules of energy.
(4) Phase-only modulation in free-space: Beyond PICs, PCMs are also used to modulate the amplitude of the free-space wavefront. However, so far phase-only modulation has not been achieved due to the use of lossy PCMs and metallic microheaters.

In this dissertation, we will discuss our efforts to address the above key challenges in order to bring this technology a step closer to commercially viable products and identify future research directions in the field of PCM-based photonics. The thesis will focus on our original work, instead of literature review. For an in-depth background on PCM photonics, we refer the readers to these review papers[6]–[8].

1.2 Outline

The thesis will be organized into six chapters, as outlined below:

- In Chapter 2, we tried to address challenge (1) by integrating wide-bandgap PCM Sb_2S_3 with Si and SiN photonic platforms[9]. We showed, for the first time, large phase modulation ($\Delta\phi \sim 0.17\pi$) with near zero insertion loss by switching 8μm long Sb_2S_3 using an integrated ITO microheater. Based on this, we further showed the low loss of Sb_2S_3 in the visible range near 740nm by cladding it on SiN mirorings and hence its compatibility with solid-state quantum emitters.

- Chapter 3 discussed effort to reduce the device footprint using low-loss PCM Sb_2Se_3, in an attempt to overcome challenge (2). We reported an ultra-compact broadband directional coupler switch with only 33μm coupling length and insertion loss as low as 0.5dB. We further demonstrated individual control of coupling and phase shift in a racetrack resonator, enabling arbitrary trimming of the resonance to different extinction ratio while maintaining the same resonance wavelength.
- Chapter 4 focuses on tackling challenge (3) – a long-standing challenge in the PCMs community. Using graphene microheaters, we demonstrated ultra-low switching energy density down to 8.7±1.4aJ/nm^3, approaching the fundamental thermodynamic limit ~1.2aJ/nm^3 to switching PCMs[10]. We showed two key building blocks of PICs – an amplitude switch based on GST and a phase shifter based on Sb_2Se_3. The phase shifter can be quasi-continuously tuned to reach 14 distinct optical phase levels.
- In Chapter 5, we go beyond PICs to demonstrate a missing component in free-space wavefront control – a non-volatile phase shifter in transmission. We leveraged the high-*Q* resonance of a diatomic metasurface to enhance the phase shift achieved by only 20nm Sb_2Se_3. We showed 0.25π phase shifter in simulation and 0.2π in experiment with near zero change in the transmission near the resonance wavelength.
- In Chapter 6, we discussed limitations in our work and the field in general, and proposed future research directions.

Chapter 2. Non-volatile programmable integrated photonics enabled by broadband low-loss phase-change material

PCMs have long been used as a storage medium in rewritable compact disk and later in random access memory. In recent years, the integration of PCMs with nanophotonic structures has introduced a new paradigm for non-volatile programmable photonics. However, the high loss of the archetypal PCM $Ge_2Sb_2Te_5$ in both visible and telecommunication wavelengths has fundamentally limited its applications[11]. Sb_2S_3 has recently emerged as a wide-bandgap PCM with transparency windows ranging from 610 nm to near-IR[12]. In this Chapter, the strong optical phase modulation and low optical loss of Sb_2S_3 (SbS) are experimentally demonstrated for the first time in integrated photonic platforms at both 740 and 1550 nm. A phase shift of 0.17π is demonstrated by electrically switching 8μm SbS in a microring using an integrated ITO microheater with near zero insertion loss. As opposed to silicon, the thermo-optic coefficient of Sb_2S_3 is shown to be negative, making the Sb_2S_3-Si hybrid platform less sensitive to thermal fluctuation. Chapter 2 experimentally verifies prominent phase shift and low loss of SbS in wavelength ranges relevant for both solid-state quantum emitter and telecommunication, enabling potential applications such as optical field programmable gate array[13], post-fabrication trimming[14], and large-scale integrated quantum photonic network[3]. Part of the chapter is adapted from my previous publication Ref. [9].

2.1 Materials Characterizations

Four samples of 100nm-thick SbS were deposited by sputtering on silicon substrates (See section 2.7 for details on fabrication) and were later annealed for 20mins at four different

temperatures, ranging from 423K to 573K. The optical constants of SbS in amorphous and crystalline states were first measured by ellipsometry (Fig. 2.1a) for optical mode simulation. The phase transition is confirmed in both X-ray diffraction (XRD) (Fig. 2.1b) and Raman spectroscopy (Fig. 2.1c). We found that the material started to crystallize at ~523K and continued to crystallize through 573K, as seen from the emerging XRD peaks in Fig. 2.1b. The Bragg diffraction angles 2θ that give rise to constructive interference match with the previous literatures[15]–[18] and correspond to the characteristic crystallographic planes in typical SbS crystals. The optical micrographs (right panel of Fig. 2.1b) support the XRD results, showing the nucleation and growth of SbS polycrystalline domains with increasing temperature. The grain growth was incomplete at 523K and reached a completion at 573K. This is further corroborated by the Raman spectrum showing the characteristic Raman shift in both as-deposited amorphous and annealed crystalline SbS, denoted as aSbS and cSbS respectively, with good match to the previous literatures.[16], [18]

Table 2. 1: Comparison of Δn and k_c of Sb_2S_3, Sb_2Se_3, GST, and GSST at 633nm and 1550nm.

	Δn at 633nm	k_c at 633nm	$\Delta n/k_c$ at 633nm	Δn at 1550nm	k_c at 1550nm	$\Delta n/k_c$ at 1550nm
GST[19]	0.16	3.82	0.04	2.74	1.09	2.51
GSST[11]	0.62	2.56	0.24	1.75	0.42	4.17
Sb_2Se_3[20]	1.12	1.40	0.8	0.76	0	Undefined
Sb_2S_3	0.87	0.56	1.55	0.54	0.05	10.8

k_c (extinction coefficient) is quoted for the crystalline state of the PCM. Δn is the refractive index change from amorphous to crystalline state.

The minimal optical loss of SbS originates from its wide bandgap[12] (~1.7-2eV), which leads to suppressed band to band absorption from 610nm. Even in its crystalline state, SbS exhibits low loss (k~0.05) at 1550nm. This is superior to the recently-reported broadband

transparent GSST[11], [21], [22] which has near-zero loss at 1550nm in amorphous state but suffers from non-negligible loss in the crystalline state (see Table 2.1). Another emerging PCM Sb_2Se_3 has near zero loss in both states near 1550nm[20] but is plagued by the bandgap absorption in the visible range and hence exhibits measurable losses near 633nm. One potential limitation for SbS, however, is the simultaneous reduction in both Δn and k, as a result of Kramers-Kronig relation, and hence smaller phase shift per unit length. However, this could be easily overcome by using longer or thicker SbS (as discussed later in the paper), thanks to the reduced optical absorption.

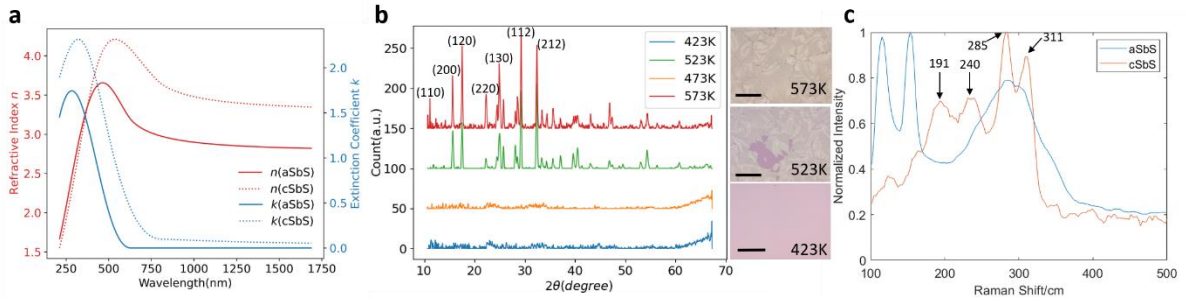

Figure 2. 1: Material characterization of SbS.

a Fit refractive index (n) and extinction coefficient (k) of 100nm SbS in amorphous and crystalline states. **b** X-ray diffraction spectrum of SbS annealed at four different temperatures for 20mins. Characteristic diffraction peaks are indexed based on literatures. The right panel shows the morphological evolution of SbS polycrystal grains as the annealing temperature increases (scale bar is 200μm). **c** Raman spectrum of amorphous and crystalline (annealed at 573K) SbS. The characteristic Raman shifts of cSbS are indexed according to the literature.

The effective index and mode profiles of the waveguides with different thicknesses of SbS on SOI waveguide are simulated using Lumerical Mode Solutions to find the optimal thickness. Fig. 2.2a and 2.2b show that the fundamental quasi-transverse electric (TE) mode at 1550nm is confined in the waveguide and there is a large effective index change (Δn_{eff}~0.022) due to the phase transition of 20nm SbS. Thanks to the low loss of SbS, we get a large ratio

between the effective index change and the loss at the crystalline state ($\frac{\Delta n_{eff}}{k_{eff}} \sim 4.183$). Note that the final capping layer of 10nm SiN is not considered in the reported simulation. The extra SiN capping raises the effective index by 0.06 but does not change the Δn_{eff} and loss. The increased imaginary part in cSbS indicates the increase of optical absorption in the crystalline state. We also plot the change of effective index and optical absorption as a function of SbS thickness (Fig. 2.2e). The index contrast increases with increasing PCM thickness (as the optical mode has stronger interaction with the PCM) but the optical absorption also becomes larger. This is illustrated in Figures 2.2c and 2.2d with 66nm of SbS cladded on silicon waveguide ($\Delta n_{eff} \sim 0.038\ and\ \frac{\Delta n_{eff}}{k_{eff}} \sim 3.98$). Based on our simulation, we chose the SbS thickness as 20nm to reduce the excess loss ($\alpha = \frac{4\pi k_{eff}}{\lambda} = 0.185 dB\mu m^{-1}\ and\ \Delta n_{eff} \sim 0.022$). The index contrast far surpasses the typical Si thermal phase shifter which can only achieve $\Delta n_{eff} < 1.8 \times 10^{-4}$ per Kelvin change in temperature.[23] The 20nm thickness is also chosen to facilitate the thermal diffusion as the PCM needs to be quenched rapidly during amorphization so thinner film has faster cooling rate.[24]

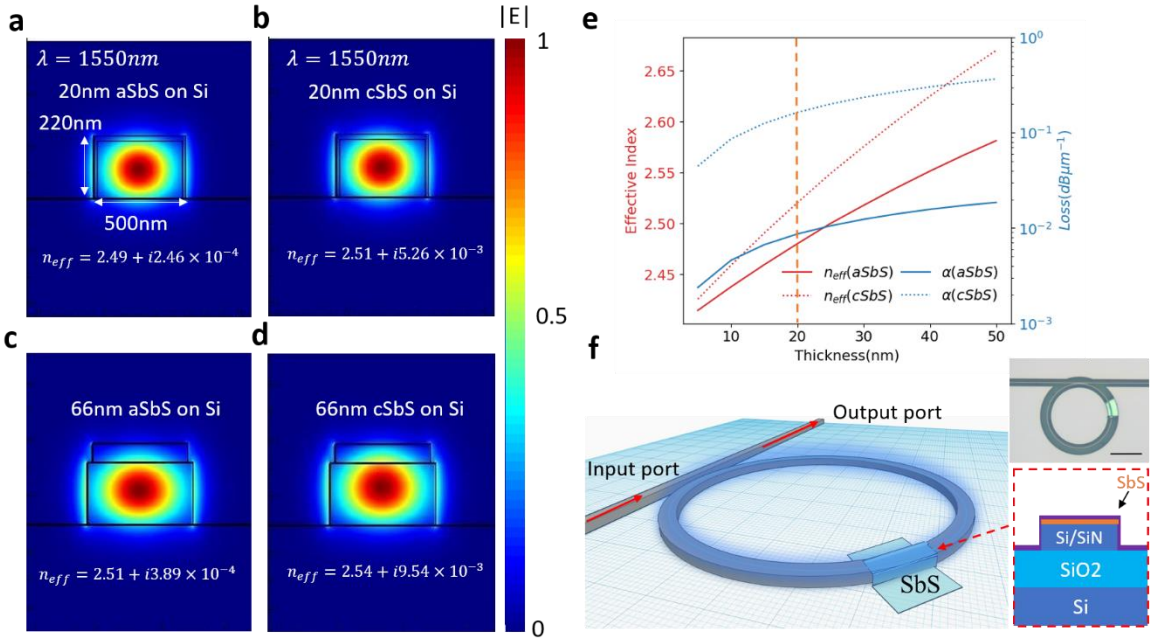

Figure 2. 2: Optical mode simulation of SbS on SOI.

a, b Simulated fundamental TE mode profiles of 20nm aSbS/cSbS on SOI hybrid waveguide at 1550nm using the optical constants extracted from ellipsometry. **c, d** Simulated fundamental quasi-TE mode profiles of 66nm aSbS/cSbS on SOI hybrid waveguide at 1550nm. Here, SbS is only placed on top of the waveguide to be consistent with the experiment. **e** Variation of effective index and absorption coefficient with the SbS thickness. **f** Schematic of microring resonators with SbS patterned on the ring. The inset shows optical micrograph (scale bar: 20μm) of SbS-capped ring and the cross-section of the device.

2.2 SbS on Si microring resonators

Varying lengths of 20nm and 66nm thick SbS are deposited on Si microring resonators of radius 20 μm (device schematic shown in Fig. 2.2f) using standard fabrication techniques (See section 2.7). The insets show the optical micrograph of Si microring patterned with 10μm-long, 20nm-thick SbS and the cross-section of the device. The PCM is capped with 10nm of PECVD SiN to prevent oxidation during annealing.

The phase shift induced by GST[19] and different thicknesses of SbS near 1550nm is compared in Fig. 2.3a where the length of PCM is fixed at 10μm. Due to the high loss of cGST ($\alpha = 7.6dB\mu m^{-1}$), the resonance is destroyed at crystalline state, whereas the resonance is clearly visible for the 20nm and 66nm thick cSbS capped rings, implying that cSbS has much lower optical loss than GST. This demonstrates that SbS could potentially be used to build optical phase shifter[25] that operates based on electro-refractive modulation. The spectral shift caused by phase transition of 66nm SbS is 0.93nm compared to 0.53nm for 20nm SbS, giving rise to 75% increase in the shift. This is very close to the 73% increase in Δn_{eff} predicted by the mode simulation (Figures 2.2a-2.2d). It is also worth pointing out that the microring is designed to be critically coupled at crystalline state which is the reason why the extinction ratio of the resonance increases dramatically as a result of the enhanced loss due to the phase transition. Figure 2.3b shows how the spectral shift and extinction ratio evolved as the length of 66nm-thick SbS increases from 0 to 50μm across the telecommunication C-band. The red shift becomes increasingly large such that the resonance eventually shifts over one free spectral range of the microring at 50μm. The rise in optical loss with length is confirmed by the transition from overcoupling (small resonance dip) at 0μm, near critical coupling (maximum dip) at 10μm, and strong undercoupling (small dip) at 50μm. Notice that a red shift (~0.83nm) is seen on the 0μm one (i.e., no SbS) due to a global capping of PECVD SiN before thermal annealing, which does not affect our conclusion as the capping layer is lossless and affects all the devices equally.

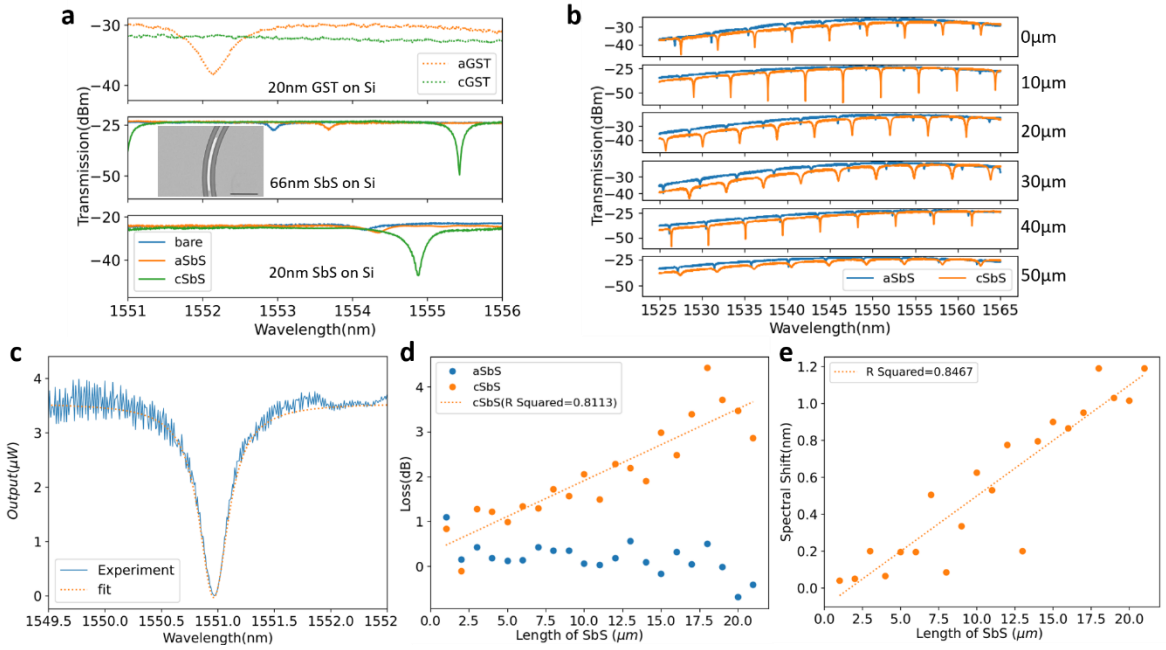

Figure 2. 3: Characterization of SbS on Si microring resonators.

a Optical spectrum of microring resonators capped with 20nm GST (top), 66nm SbS (middle), and 20nm SbS (bottom) in amorphous and crystalline states. The length of PCM was kept at 10μm. The inset of middle plot shows the SEM of 66nm SbS placed only on top of the waveguide. **b** Transmission of ring resonators over the C band for increasing length of 66nm aSbS and cSbS on SOI. 0μm indicates the absence of SbS (i.e., a bare ring). **c** Lorentzian fitting of measured resonance dip of Q factor ~ 5000. **d** Optical loss of 20nm thick aSbS and cSbS on SOI at various lengths. **e** Spectral shift from amorphous to crystalline with increasing length of 20nm thick SbS on SOI.

To analyze the optical phase modulation effect and loss quantitatively, the resonance dip near 1550nm is fit with a Lorentzian function to extract the quality factor (Q) and the loss (Fig. 2.3c). The optical phase modulation effect is quantified as the spectral shift $\Delta\lambda$ from aSbS to cSbS, while the attenuation is extracted from the Q factor reduction from amorphous to crystalline state. The results are plotted in Figs. 2.3d-2.3e. The experimental data show a good linear fit where the red shift due to the SbS phase transition increases linearly with the length of SbS. The spectral shift per unit length of SbS is extracted to be 0.060±0.006

nm·μm^{-1}, corresponding to a phase shift of 0.023±0.002 π·μm^{-1}. The loss introduced by SbS is estimated from the Q factors using the relation[19]:

$$Loss = 2\pi R\frac{2\pi n_g}{\lambda_0}\left(\frac{1}{Q}-\frac{1}{Q_0}\right)=\frac{2\pi\lambda_0}{FSR}\left(\frac{1}{Q}-\frac{1}{Q_0}\right) \qquad (1)$$

where n_g is the group index, Q is the quality factor of the ring after SbS phase transition and Q_0 is the Q factor of the ring with as-deposited SbS, FSR is the free spectral range. The loss of cSbS (orange line) increases linearly with the PCM length whereas the aSbS (blue line) remains almost flat, signifying extremely low loss as also confirmed by the mode simulation (Fig. 2.2a). The attenuation of cSbS is estimated to be 0.16±0.02dBμm^{-1}, almost 50 times smaller than that of cGST.[19]

The spectral shift induced by PCM on ring can be numerically calculated using equation[19]:

$$\frac{\Delta\lambda}{L_{SbS}}=\frac{\Delta n_{eff}\lambda_0}{2\pi R n_{eff0}} \qquad (2)$$

where R is the radius of the microring, λ_0 and n_{eff0} are the resonance wavelength and effective index before phase change, respectively. Δn_{eff} due to SbS phase change is extracted from the mode simulation as discussed above. The simulation results are compared with the experimental results in Table 2.2.

Table 2. 2: Comparison between the simulation and experimental results.

	Simulation	Experiment
$\Delta\lambda(\mathrm{nm}/\mu\mathrm{m})$	0.109	0.060 ± 0.006
$\Delta\alpha(dB/\mu m)$	0.185	0.160 ± 0.018

The extracted Δn_{eff} from experiment is 0.012 compared to 0.022 from simulation (which uses the ellipsometry data from blanket SbS measurement). This reflects a potential deviation of material optical properties, especially the real part of refractive index, as the PCM shrinks down from 1 by 1cm blanket film (used for ellipsometry) to thin nanoscale patches on waveguides. Similar deviation has also been previously reported in nano-patterned GST.[19] Another possible explanation is the change of SbS composition upon thermal annealing due to the Sulfur loss.[15] Although we have verified that the stoichiometry change is small for 100nm SbS upon thermal annealing, it is hard to rule out the effect of composition change in 20nm SbS. It is possible that only the surface PCM suffers from composition variation, so the measured composition change is small for 100nm SbS. For 20nm SbS, such variation, if indeed exists, may lead to more prominent deterioration of device performance. Finally, the nonuniform coverage of SbS on the waveguide sidewall could also be a contributing factor – SbS deposited on the sidewall is likely to be thinner than on the top of the waveguide due to the slight directional nature of the sputtering. On the other hand, the ellipsometry does predict the imaginary part of refractive index accurately which implies that the material's optical loss does not vary significantly as the dimensions reduce. The extracted loss is higher than what was found in the previous work[20] where SbS was also capped on Si waveguides. This higher loss can be attributed to surface oxidation or Sulfur migration due to the thin (10nm) capping layer used. Thicker encapsulation (>50nm) could prevent this in future. The result shown here provides an insight to the design of PCM based photonic devices where the discrepancy between nano-patterned and the bulk material's optical properties must be considered.

2.3 Electrical switching of SbS

To demonstrate the feasibility of an active integrated device based on SbS, an ITO external heater is patterned on top of the PCM to achieve on-chip electrical actuation of SbS phase transition (See section 2.7 for fabrication details), as shown in Fig. 2.4a. On-chip electrically switching has advantages over excitation by free-space laser[20] or waveguide optical switching,[26] because it does not require the complex alignment process of free-space setup while allows scale-up of the PICs with increased compute density. While other means of electrical switching mechanisms[27]–[29] has been leveraged for tuning PCMs in integrated photonics, ITO microheater[30]–[32] has the benefits of high electrical conductivity, low optical loss from visible to near IR and easy integration via sputtering. By applying voltage pulses across the ITO, electrical current causes Joule heating and subsequently phase transition of the PCM. Here, a microring modulator design[33] is adopted to amplify the modulation effect of SbS. The Si waveguide is partially etched by 140nm, as opposed to fully etch, to leave an 80nm-thick Si slab which acts as a heat sink to facilitate thermal diffusion from the PCM. It also helps the lift-off of ITO film as thinner ITO can be used to ensure conformal step coverage. The false color SEM in Fig. 2.4b shows fabricated device where the Si waveguide is conformally covered with ITO. The SbS is deposited beneath the ITO, and hence is not visible in the SEM. Figures 2.4c-2.4d demonstrate the electrical switching of 8μm-long SbS into its crystalline state by a DC voltage sweep from 0 to 1V at power of 13mW. The I-V curve in the Figure 4e shows a relatively linear relationship – a proof that ITO has stable resistance over this voltage/temperature range. Heat transfer simulation[24] in Fig. 2.4f (top) shows the temperature distribution under stationary heating from a DC voltage of 1V. The temperature reaches 650K which is higher than the crystallization temperature but lower than the melting point of SbS. The DC sweep allows extended period for long range atomic diffusion, during which the atoms can settle in the most energetically favourably

positions. The red shift is a result of PCM phase transition because it was found that the refractive index of amorphous ITO remains relatively constant upon heating up to 773K[34]. The spectral shift of 0.4nm (or $\Delta\phi \sim 0.17\pi$) matches very well with the predicted shift of 0.39nm based on simulation of rib waveguide but lower than what was measured from fully etched waveguide (0.48nm) due to less mode confinement. However, since the ring is designed to be critically coupled at crystalline state, it is still large enough to give an extinction ratio of over 30dB in optical transmission with minimal increase in the resonance linewidth. The strong phase modulation at a cost of small loss shows that SbS is a promising tuning medium for next-generation non-volatile large-scale PICs.

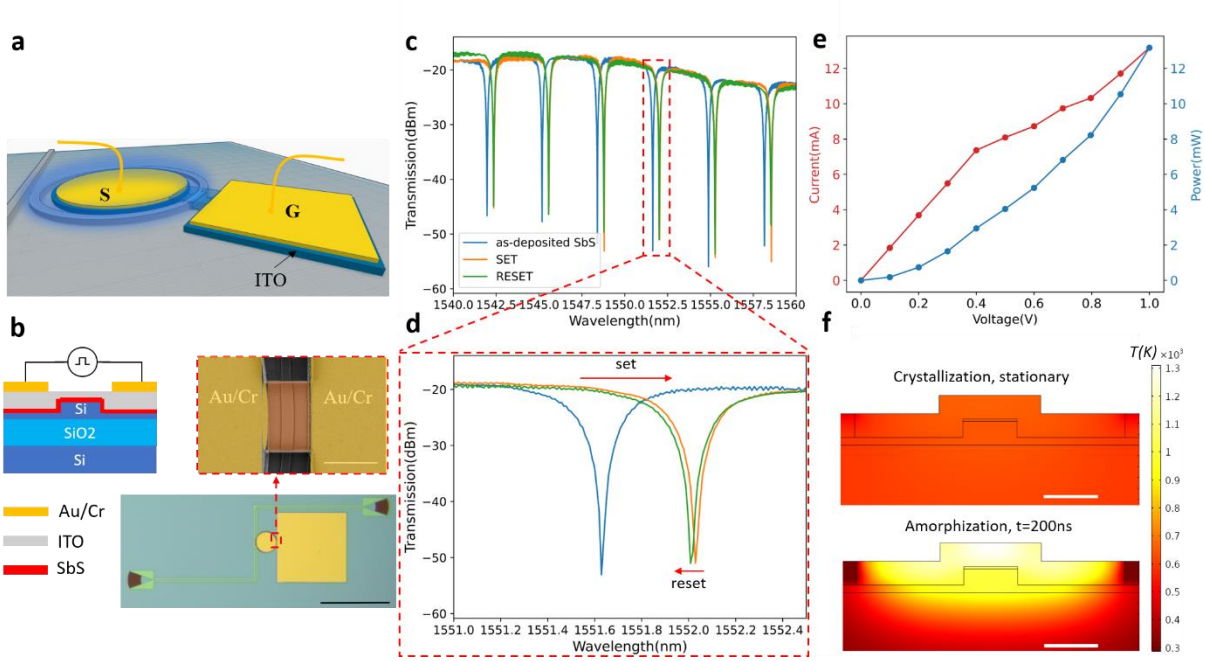

Figure 2. 4: Electrical Switching of SbS in a microring.

a Schematic of integrated photonic microring switch based on SbS. **b** Cross-section of the device, optical micrograph (scale bar: 200µm) and false color SEM (scale bar: 3µm) of the fabricated device. **c, d** Transmission spectrum showing the SET and RESET operation as red and blue shift of the resonance dip. **e** I-V curve (red) and power (blue) during a 0-1V DC sweep that triggered the SET operation. **f** Temperature distribution under stationary heating at 1V (top) and after 200ns pulse at 6V (bottom). Scale bar is 500nm.

The device can be reset by applying a 6V 200ns square pulse using a function generator, causing a slight blue shift. The bottom plot of Fig. 2.4f shows the simulated temperature distribution after a 200ns 6V square pulse is applied. The temperature at the top layer of SbS has reached over 1000K, more than what is required for amorphization and below the melting point of Si waveguide. The trailing edge of the pulse was set to be 8ns to allow the melt-quench of the PCM during which the fast-moving atoms are quickly frozen into a disordered state. However, the RESET spectrum does not perfectly overlap with the original spectrum while the *Q* factor remains roughly the same as the SET spectrum. We speculate that the abrupt resistivity increase of ITO at 650K[35] gives rise to regional thermal hot spots that causes nonuniform heating of the PCM. Pulses of higher voltages led to further blue shift and broadening of resonance dip, which implies that the PCM amorphization is accompanied by waveguide damage, as some local hotspots may have temperature exceeding the melting point of Si. Since the cyclability of blanket film SbS has been recently reported using laser pulses,[20], [36] we believe the low cyclability of our device is more of a heater design issue rather than SbS's material issue. Transparent conductors whose conductivity is thermally stable such as graphene[37] and FTO[38] could provide a better solution for operation with large number of cycles.

The switching time for the SET operation is 1s, which is the duration of 0-1V voltage sweep, while the switching time for RESET is 200ns, which is the pulse width. Such relatively slow switching speed is however not limited by the fundamental PCM properties but by the thermally unstable heater material and unoptimized heater design (i.e., thermal diffusion is impeded by the thick ITO). In the future, the waveguides can be planarized to reduce the required heater material thickness or atomically thin heater such as graphene can be used.

2.4 Thermo-optic effect of SbS

Due to the large positive thermo-optic (TO) effect of silicon,[23] SOI platform is prone to thermal fluctuations, particularly for high-*Q* optical resonators.[39] Integrated metal heaters near the resonators are normally used to stabilize the temperature and prevent resonance drift from the temperature variation in the environment.[40], [41] The TO effect of GST has already been investigated on SiN waveguides.[42] Here, we showed that SbS exhibits strong negative TO effect that counteracts the positive TO effect of silicon. The overall TO coefficient of SbS-SOI hybrid waveguide is hence lower than pure Si waveguide, making the hybrid system more thermally stable. By heating the ring resonators capped with different lengths of SbS, the TO coefficient of SbS on SOI is extracted in both amorphous and crystalline states near 1550nm. Thicker SbS (66nm) is used to amplify the minimal change in resonance spectrum from the TO effect of SbS. Note that the PCM is only placed on top of the waveguide to simplify the calculation of mode confinement factor (Figs. 2.2c and 2.2d). The TO coefficient of SbS-SOI hybrid waveguide can be approximated to the first order as[43]:

$$\frac{dn_{eff}}{dT} = \Gamma_{Si}(\lambda)\frac{dn_{Si}}{dT}(\lambda) + \Gamma_{SbS}\frac{dn_{SbS}}{dT}(\lambda) \qquad (3)$$

where the mode confinement factors *Γ*[44] of Si waveguide and SbS are wavelength dependent and can be calculated using Lumerical Mode Solutions. By adjusting the temperature of a thermal electric controller beneath the chip, we can tune the resonances (Fig. 2.5a). Using the resonance shift and the temperature change, the collective TO coefficient of SbS-Si hybrid waveguide can be expressed as (see section 2.5 for derivation):

$$\frac{dn_{eff}}{dT} = \left(\frac{\lambda_{res} n_{eff}^{Si}}{\lambda_{res0}\Delta T} - \frac{n_{eff}^{Si}}{dT} - \frac{dn_{eff}^{Si}}{dT}\right)\frac{2\pi R - L_{SbS}}{L_{SbS}} + \left(\frac{\lambda_{res}}{\lambda_{res0}} - 1\right)\frac{n_{eff0}}{\Delta T} \qquad (4)$$

Note that $\frac{dn_{eff}}{dT}$ and $\frac{dn_{eff}^{Si}}{dT}$ in Equation (4) not only describe the TO effect of SbS-SOI hybrid waveguide and Si waveguide, but also include the effect of dispersion which must be subtracted to extract the pure temperature effect to the refractive index. n_{eff0} and n_{eff}^{Si} are the effective indices of SbS-Si hybrid waveguide and SOI waveguide respectively at the resonance wavelength before the temperature change of ΔT. λ_{res0} and λ_{res} are the resonance wavelengths before and after the temperature change, respectively. Substituting (3) into (4) hence yields the expression of TO coefficient of pristine SbS in terms of the measurable parameters λ_{res0}, λ_{res}, and ΔT. Here, the length of the SbS is varied from 0 to 80μm (nine rings) and each device is measured at 5 different temperatures (i.e., for four ΔTs) from 297K to 317K, giving four values of TO coefficient for each length of SbS. No definite dependency of SbS TO coefficient on temperature is observed in the experiment. Hence, it is assumed that the change in the TO coefficient with temperature is negligible for both Si and SbS in this temperature range. Fig. 2.5b shows the wavelength dependent TO coefficients of both amorphous and crystalline SbS compared with Si near 1550nm.[23] The data points are calculated as the average of TO coefficients across four ΔTs while the error bars measure the standard deviation from the average of four. The TO coefficient of aSbS exhibits a strong linear dependency to wavelength, whereas the TO coefficient of cSbS is wavelength independent. The TO coefficient of aSbS and cSbS at 1550nm are estimated to be $-3.11 \times 10^{-4} K^{-1}$and $-7.28 \times 10^{-5} K^{-1}$. The strong negative TO effect of SbS shows that the SbS-SOI hybrid platform has less sensitivity to heat fluctuation than SOI does and is suitable for use in non-volatile integrated photonics.

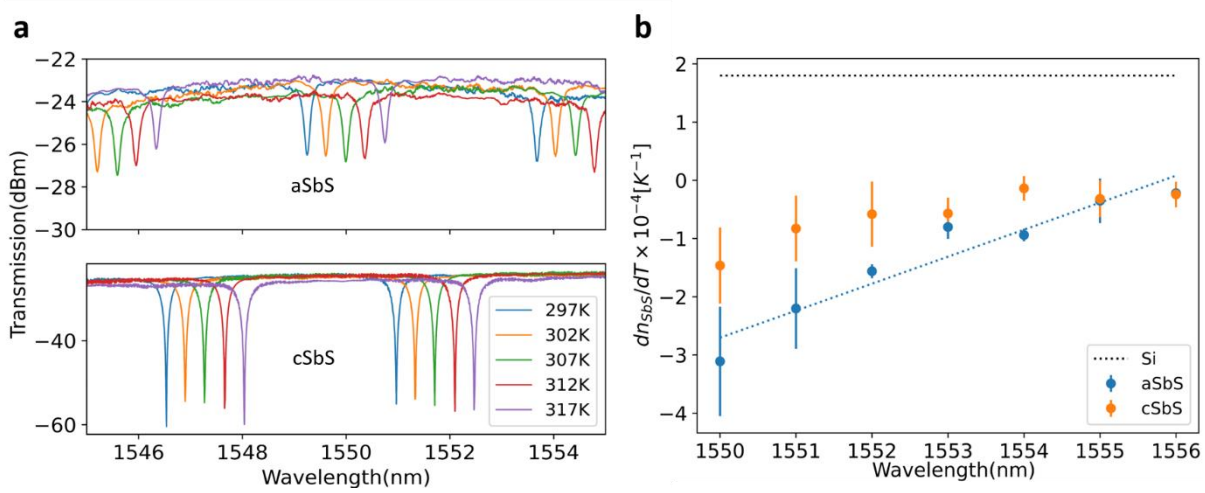

Figure 2. 5: Thermo-optic effect of SbS on SOI.

a Spectral shift caused by raising the temperature from 297K to 317K of microring capped with 10μm-long, 66nm-thick SbS. **b** Extracted thermo-optic coefficient of aSbS and cSbS compared with silicon.

2.5 Derivation of SbS thermo-optic coefficient

Starting with the resonance condition for a ring resonator, we can write:

$$\lambda_{res0} = \frac{n_{eff0}L}{m}, m = 1,2,3 \ldots$$

where λ_{res0} is the resonance wavelength before temperature change, n_{eff0} is the effective index of the SbS-SOI hybrid waveguide before temperature change, L is the optical path length which equals $2\pi R$ for a ring of radius R. m is the mode number which can only be integers. For the same resonance mode, a temperature change will alter the mode's effective index and hence the resonance wavelength. We can write *m* in terms of the effective index and resonance wavelength, and then equate the *m* number before and after the temperature change, arriving at:

$$\frac{n_{eff}^{Si}+\Delta n_{eff}^{Si}}{\lambda_{res}}(2\pi R - L_{SbS}) + \frac{n_{eff0}+\Delta n_{eff}}{\lambda_{res}}L_{SbS} = \frac{n_{eff0}}{\lambda_{res0}}L_{SbS} + \frac{n_{eff}^{Si}}{\lambda_{res0}}(2\pi R - L_{SbS}) \quad (5)$$

Expression on the left of equation (5) is the mode order after raising the temperature whereas expression on the right denotes the *m* before the temperature change. n_{eff0} and n_{eff}^{Si} are the effective indices of SbS-SOI hybrid waveguide and SOI waveguide respectively before temperature change of ΔT. λ_{res0} and λ_{res} are the resonance wavelengths before and after the temperature change, respectively. Rearranging (5) such that only Δn_{eff} is on the left and divide ΔT on both sides will give Equation (4) in section 2.4.

It should also be pointed out that Δn_{eff}^{Si} and Δn_{eff} are the effective index changes of SOI waveguide and SbS-SOI hybrid waveguide induced by both the temperature change and resonance shift due to dispersion, expressed as:

$$\Delta n_{eff}^{Si} = \frac{dn_{eff}^{Si}}{dT}\Delta T + \frac{dn_{eff}^{Si}}{d\lambda}\Delta\lambda \qquad (6)$$

$$\Delta n_{eff} = \frac{dn_{eff}}{dT}\Delta T + \frac{dn_{eff}}{d\lambda}\Delta\lambda \qquad (7)$$

$\frac{dn_{eff}^{Si}}{dT}$ and $\frac{dn_{eff}}{dT}$ are the effective TO coefficients of Si waveguide and SbS-SOI hybrid waveguides that appear in Equation (3) in section 2.4. $\frac{dn_{eff}^{Si}}{d\lambda}$ and $\frac{dn_{eff}}{d\lambda}$ describe the dispersion of Si and SbS-SOI hybrid waveguides in the wavelength range of interest. Since the resonance was tuned from 1546nm to 1556nm in experiments, the $\frac{dn_{eff}^{Si}}{d\lambda}$ is calculated to be $-1.314 \times 10^{-3} nm^{-1}$ using Lumerical Mode Solutions in this wavelength range, while $\frac{dn_{eff}}{d\lambda}$ of aSbS and cSbS on SOI are $-1.21 \times 10^{-3} nm^{-1}$ and $-1.19 \times 10^{-3} nm^{-1}$ in the same range, respectively. The mode confinement factors Γ_{aSbS} *and* Γ_{cSbS} are simulated to be 0.0907 and 0.1138 at 1550nm with a wavelength dependency of $1.6 \times 10^{-4} nm^{-1}$*and* $6 \times 10^{-5} nm^{-1}$. To calculate the pure TO coefficient of SbS-SOI waveguide, we just need to subtract $\frac{dn_{eff}}{d\lambda}\frac{\Delta\lambda}{\Delta T}$ from $\frac{dn_{eff}}{dT}$ in Equation (4) of section 2.4.

2.6 SbS on SiN microring resonators

Finally, since SbS is transparent near visible wavelengths, the tuning ability of SbS on SiN platform is also investigated. Specifically, we probed the wavelength regime near 740nm, where quantum emitters like SiV in diamond[45] and quantum materials like Wse_2 emit.[46] A second chip was fabricated (See section 2.7) on SiN-on-oxide platform with similar design to probe the optical properties of SbS near 740nm. Figs. 2.6a-2.6b show the mode simulation of 20nm SbS on SiN at 740nm wavelength where the effective index change $\Delta n_{eff} = 0.04$ is nearly two times that of SbS on SOI at 1550nm. The theoretically calculated $\Delta\lambda$ is 0.273 nm·μm^{-1} and the loss is 2.48dB·μm^{-1}. Fig. 2.6c shows the transmission spectrum of 5μm-long SbS on SiN ring (10μm radius) before and after thermal annealing. Owing to low optical losses, the resonances are clearly visible in both amorphous and crystalline states from 720nm to 770nm whereas the same length of GST will destroy the resonances. Hence, our experiment demonstrates the unlimited potential of SbS to be used in tunable visible integrated photonics. We note that the experimentally extracted $\Delta\lambda$ and loss of cSbS do not match quite well with the simulation and further experiments are planned to characterize the exact optical phase modulation effect of SbS near 740nm.

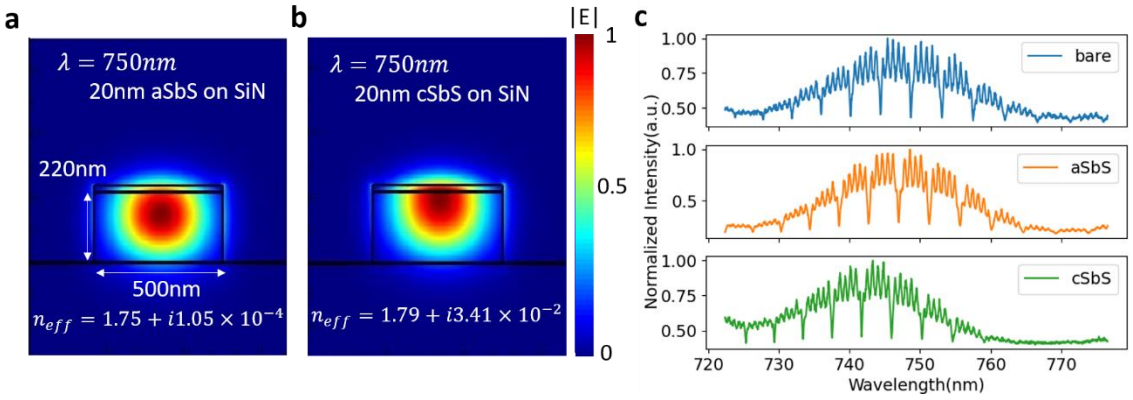

Figure 2. 6: SbS on SiN microrings in near visible wavelength.

a Simulated fundamental quasi-TE mode profiles of 20nm aSbS/cSbS on SiN hybrid waveguide at 750nm. Note here that the SbS is only place on top of the waveguide. **b** Transmission spectrum of SiN ring resonators capped with 5µm aSbS and cSbS near 750nm.

2.7 Device fabrication

The SbS-on-SOI microring resonators were fabricated on a 220-nm thick silicon layer on top of a 3-µm-thick buried oxide layer (SOITECH). The pattern was defined by a JEOLJBX-6300FS 100kV electron-beam lithography (EBL) system using positive tone ZEP-520A resist. 220 nm fully etched ridge waveguides were made by an inductively coupled plasma reactive ion etching (ICP-RIE) process. A second EBL exposure using positive tone poly(methyl methacrylate) (PMMA) resist was subsequently carried out to create windows for the SbS deposition. After development, 20nm SbS was DC sputtered from a SbS target (Plasmaterial Ltd.) in a magnetron Sputter System (Lesker Lab18) under Ar atmosphere at 27W and base pressure of ~5×10^{-7} Torr. The Ar flow rate is controlled to maintain a sputtering pressure of 3.5mTorr. The plasma is stabilized for 5 minutes before the actual deposition. The lift-off of SbS was completed using methylene chloride followed by a global capping of 10nm PECVD SiN at 125°C to prevent oxidation. Note that the SbS samples used for ellipsometry, Raman and XRD were deposited on Si [100] wafers and capped with 10nm sputtered ITO. The SbS-ITO integrated photonic switch were fabricated in a similar process where the waveguide was only partially etched by 140nm for easier liftoff of ITO. A 200nm thick ITO layer was sputtered following the 20nm SbS deposition without breaking vacuum. After the lift-off of the SbS/ITO layers, an extra EBL overlay and electronbeam evaporation of Au/Cr (60nm/30nm) were done to pattern the electrode pads. For crystallization of SbS, rapid thermal annealing (RTA) at 300 °C for 20 min was performed under N_2 atmosphere.

The SiN microring resonators were fabricated on a 220-nm-thick SiN membrane grown via LPCVD on 4 µm of thermal oxide on silicon (Rogue Valley Microelectronics). We spun

roughly 400 nm of ZEP520A, which was coated with a thin layer of Pt/Au that served as a charging layer. The resist was then patterned by EBL and the pattern was transferred to the SiN using the same RIE in CHF_3/O_2 chemistry. The SbS was deposited onto the SiN rings using the same process mentioned above.

2.8 Summary

In this chapter, wide-bandgap PCM Sb_2S_3 is investigated for its applications in non-volatile programmable photonics. The XRD and Raman data have confirmed the phase transition of Sb_2S_3 from amorphous to crystalline state while ellipsometry shows that the material exhibits broadband transparency from 610nm to near-IR. The large refractive index contrast and low absorptive loss of Sb_2S_3 are verified experimentally for the first time on SOI and SiN integrated photonics platform using microring resonators at the telecom C-band and near visible wavelengths. The measured resonance shift is 0.06nm·μm^{-1} at 1550nm while the optical losses at 1550nm are 0.16dBμm^{-1} in crystalline state and zero in amorphous sate. An on-chip non-volatile Sb_2S_3-SOI microring switch with low-loss, large optical phase shift ($\Delta\phi \sim 0.17\pi$) and extinction ratio(>30dB) is demonstrated. Additionally, the thermo-optic coefficient of aSbS and cSbS at 1550nm is extracted to be $-3.11 \times 10^{-4} K^{-1}$ and $-7.28 \times 10^{-5} K^{-1}$ respectively, with opposite sign to that of Si, showing that the SbS-SOI hybrid waveguide is more stable to temperature variation than Si waveguide. Our experiments introduce Sb_2S_3 as a promising candidate for the low loss non-volatile phase tuning of large-scale PIC and will find potential applications in fields such as optical FPGAs, post-fabrication trimming, and quantum information processing.

Chapter 3. Ultra-compact non-volatile broadband directional coupler switch based on low-loss phase change material

In Chapter 2 we have explored a low-loss PCM Sb_2S_3 for non-volatile programmable integrated photonics. We used silicon microrings to show its strong phase modulation (~0.17π) with near zero addition loss near both 1550nm and 740nm. However, it has limited applications because a microring is intrinsically narrow band and reversible switching of the Sb_2S_3 was not realized. In this Chapter, we demonstrated an essential building block of large-scale programmable PICs – an ultra-compact broadband directional coupler switch based on emerging low-loss PCM Sb_2Se_3. The directional coupler has a coupling length of only 33μm, a 50% reduction in footprint compared to the state-of-the-art[47], and an operating bandwidth over 50nm. It also exhibits loss insertion loss (~0.5dB) and high extinction ratio (~15dB). We further showed the individual control of coupling and phase in a racetrack resonator, enabling the tuning of resonance extinction ratio without perturbing the resonance wavelength. Both the racetrack resonator and directional coupler switch can be cycled for more than 1,100 cycles at >10dB extinction ratio without significant performance degradation. The work is a crucial step towards future energy-efficient programmable photonics with applications in post-fabrication trimming, optical interconnects, and optical computing.

3.1 Design of the direction coupler switch part I

The goal of this project is to design a directional coupler switch such that the light couples to the cross port when the PCM is in amorphous state and to the bar port when the PCM is in the crystalline state, see Fig. 3.1a. The switch is fabricated on a 220nm SOI platform and the waveguide is partially etched with 100nm slab to allow doping that forms PIN microheater[27]. To make sure the light couples, the bare silicon waveguide must have the

same effective index as the PCM-silicon hybrid waveguide to satisfy the phase matching condition, see Fig. 3.2a. For bare slab waveguide width of 500nm, hybrid waveguide width is designed to be 462nm to phase match. Coupled mode simulation is run between the silicon waveguide and the hybrid waveguide at various coupling gap. Fig. 3.2b shows the coupling of fundamental TE mode at gap of 374nm. When the Sb_2Se_3 is in the amorphous state, both the even and odd supermodes are in the two waveguides, implying a good coupling between the waveguides. When the Sb_2Se_3 is switched into the crystalline state, the optical mode only stays in one of the waveguides and there is no coupling. We sweep the coupling gap to extract the difference between the effective index of the even and odd mode, from which the coupling length L_c can be calculated based on coupled mode theory[48]. Coupling lengths for both aSb_2Se_3 and cSb_2Se_3 are plotted in Fig. 3.1b and the blue line indicates the ratio i.e., L_c in amorphous state over L_c in crystalline state. The shortest L_c that satisfies our requirement is when the ratio equals to 2[48]. More specifically, the light couples once to the cross port in amorphous state, while couples twice back to the bar port in crystalline state, see Fig. 3.1c. The simulated transmission spectrum is shown in Fig. 3.1d with broad operating bandwidth over 40nm and less than -20dB crosstalk in both states. The insertion loss is ~0.35dB in amorphous state and ~0.37dB in the crystalline state. There are two main sources of loss which can be identified in Fig. 3.1c. First, some light is lost at the input and output S bends (~0.2dB per bend) due to the tight 10μm bend radius of partially etched waveguides. Tight waveguide bend is used to reduce the FDTD simulation region, so that finer mesh can be used at the coupling region. In experiment we switched to 20μm bend which has negligible bend loss. The second source of loss comes from the mode transition from the bare Si waveguide to the hybrid waveguide, which is clearly visible in the transition region in Fig. 1c. We estimate a reflection loss of ~0.05dB per facet. The reflection loss can be avoided in the future by tapering the PCMs.

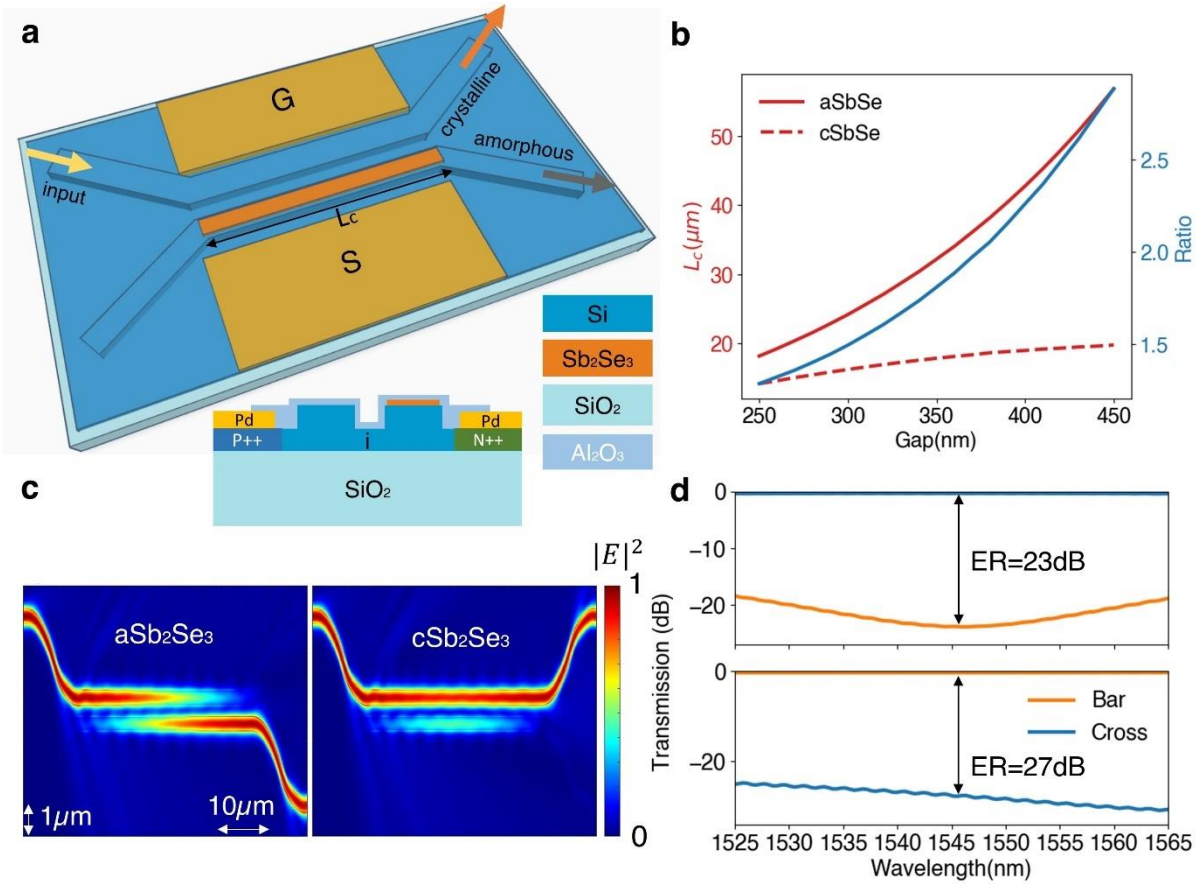

Figure 3. 1: Design of the directional coupler switch.

a Schematic of the directional coupler switch. Inset below shows the cross-section of the device. **b** Coupling length against gap for aSb_2Se_3 and cSb_2Se_3-loaded hybrid waveguide. The ratio is the coupling length of aSb_2Se_3 over that of cSb_2Se_3. **c** FDTD simulated electric field intensity of the directional coupler in cross (amorphous) and bar (crystalline) states. **d** FDTD simulated transmission spectrum of the directional coupler in cross (top) and bar (bottom) states.

3.2 Design of the directional coupler switch part II

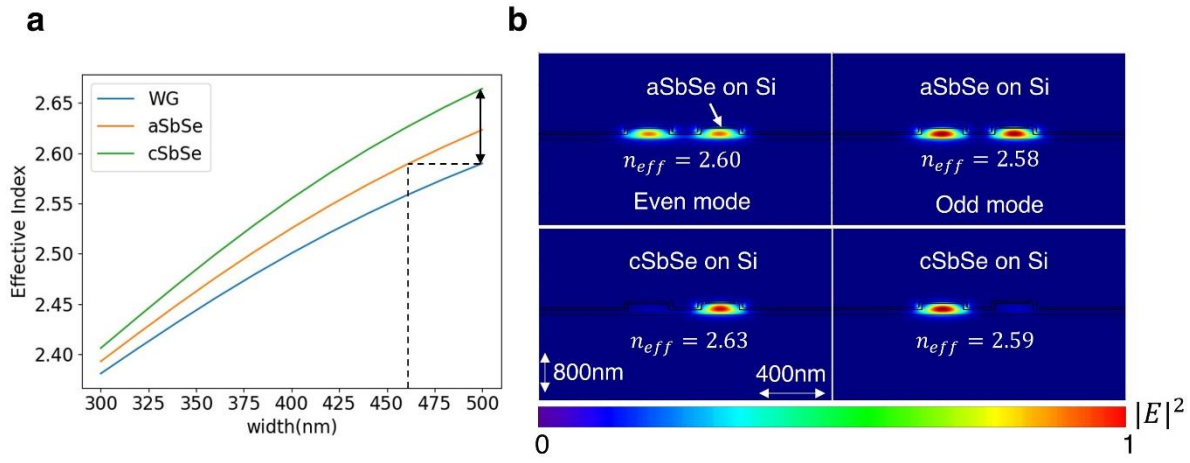

Figure 3. 2: Coupled mode simulation of bare waveguide and hybrid waveguide.

a Simulated effective index of the bare Si, aSb_2Se_3-loaded, and cSb_2Se_3-loaded waveguides. The dash line indicates where the phase matching condition is satisfied between the aSb_2Se_3-loaded waveguide (w_h=462nm) and bare Si waveguide (w=500nm). **b** Simulated fundamental quasi-TE supermodes of aSb_2Se_3-loaded waveguide (top) and cSb_2Se_3-loaded waveguide (bottom) next to a Si waveguide. w_h is 462nm and w is 500nm. Gap is 374nm.

3.3 Electrical control of the directional coupler switch

The device is fabricated using standard fabrication techniques (see section 3.4). The 33µm long Sb_2Se_3 on waveguide is electrically controlled by an integrated silicon PIN diode microheater[27]. The optical micrograph and SEM of a fabricated device are shown in Fig. 3.3a. The SEM shows good alignment of the deposited Sb_2Se_3 with the Si waveguide. Fig. 3.3b shows repeatable switching of the light between the cross and bar ports for two consecutive cycles, which corresponds to the states shown in the schematics in Fig. 3.3c. We measured very broadband bistable switching of light over 50nm near the telecommunication C band. The extinction ratio is ~8dB in the cross state and ~15dB in the bar state near 1530nm. The insertion loss is ~1dB in the cross state and ~0.5dB in the bar state near

1530nm. The lower extinction ratio and higher insertion loss in the cross state is a clear indication that the phase matching conditions are not fully satisfied, instead of due to material losses. The portion of the light that is not coupled to the cross port leaves the bar port, leading to a lower transmission in the cross port and higher transmission in the bar port. Assume the measured -9dBm of power in the bar port is fully coupled to the cross port. This increases the power at the cross port from -1dBm to -0.36dBm, where the remaining 0.36dB loss can be attributed to a combination of free carrier absorption, reflection, bend loss, and scattering loss due to the rough Sb_2Se_3 surfaces after switching. In the bar state, if we add the -15dBm power at cross port to the -0.5dBm at the bar port, we again obtain the same residual loss of 0.36dB - consistent with the cross state. Interestingly, the simulation shows a net loss of ~0.25dB introduced by the cSb_2Se_3 if we consider the experimental loss of cSb_2Se_3. The reason why the cSb_2Se_3 loss does not contribute to the insertion loss here is again because of the deviation from the phase matching condition. In simulation, light couples to the bottom waveguide and hence suffers from the cSb_2Se_3 loss at the bar state, but in experiment little or no light couples to the bottom waveguide, so cSb_2Se_3 incurs almost no loss.

Here we aim to explain the cause of the deviation from the phase matching conditions. Using SEMs, we have confirmed that the waveguide dimensions match with our design, so the only possible discrepancy is due to the mismatch between the nanoscale Sb_2Se_3 refractive index and the ellipsometry measured index which we used for simulation. To find the perfect phase matching conditions, more design of experiments (DOEs) can be added to scan a wider parameter window of hybrid waveguide width while keeping the bare Si waveguide width unchanged. This was shown in section 3.5 where we have identified a design with ~0.5dB loss and larger than 10dB extinction ratio in both cross and bar states.

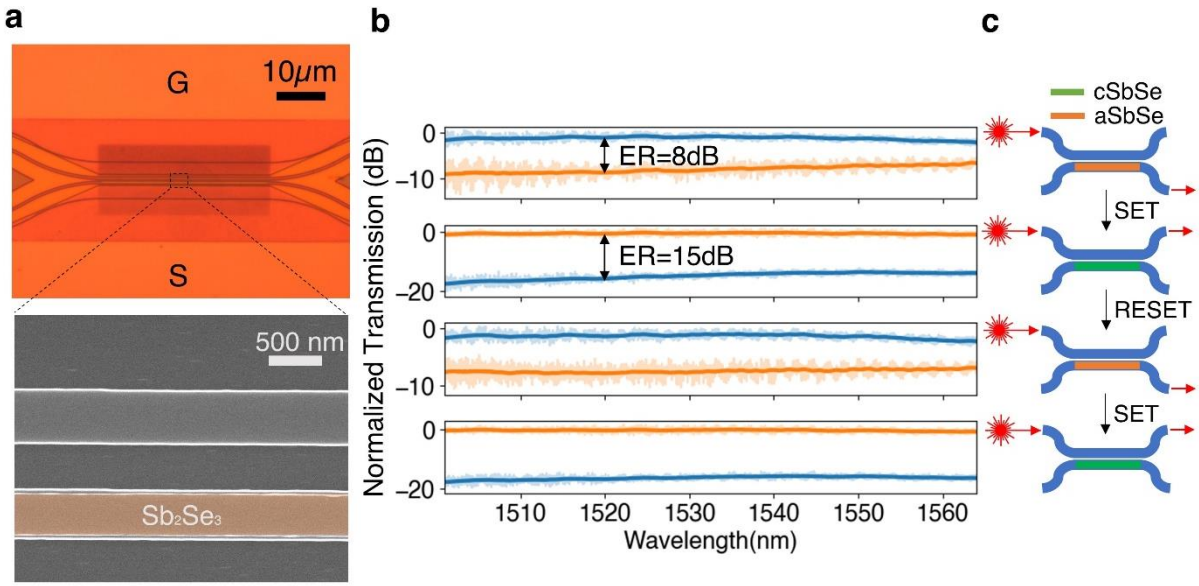

Figure 3. 3: Electrical control of the directional coupler switch.

a Optica micrograph (top) and SEM (bottom) of the fabricated switch. **b** Experimental transmission spectrum of the reversible switching between cross and bar states. 3.6V, 1.5ms width, 0.5ms trailing edge is used for SET. 8.2V, 400ns width, 8ns trailing edge is used for RESET. The spectrum is normalized by the spectrum of a waveguide near the device to remove the grating coupler spectrum. A Savitsky-Golay filter with window size 501 is applied to smooth out the spectrum. The unsmoothed data is shaded in the background. **c** Schematic showing the state of the switch, corresponding to the spectrum shown in **b**.

3.4 Device fabrication

The fabrication mainly follows our previous works[27], [47]. The silicon photonic devices were fabricated on a commercial SOI Wafer with 220-nm-thick Silicon on 2-µm-thick SiO2 (WaferPro). All devices were defined using electron-beam lithography (EBL, JEOL JBX-6300FS) with a positive-tone E-beam resist (ZEP-520A) and partially etched by ~120 nm in a fluorine-based inductively coupled plasma etcher (ICP, Oxford PlasmaLab 100 ICP-18) with mixed SF6/C4F8. The doping regions were defined by two additional EBL rounds with 600-nm-thick poly (methyl methacrylate) (PMMA) resist and implanted by boron (phosphorus)

ions for p++ (n++) doping regions with a dose of 2×10^{15} ions per cm^2 and ion energy of 14 keV (40 keV). The chips were annealed at 950 °C for 10 min (Expertech CRT200 Anneal Furnace) for dopant activation. Ohmic contact was formed after removal of the surface native oxide via immersing the chips in 10:1 buffered oxide etchant (BOE) for 10 seconds. The metal contacts were then immediately patterned by a fourth EBL step using PMMA. Metallization was done by electronbeam evaporation (CHA SEC-600) and lift-off of Ti/Pd (5 nm/180 nm). After a fifth EBL defining the Sb_2Se_3 window, a 20nm Sb_2Se_3 thin film was deposited via thermal evaporation, followed by a lift-off process. The Sb_2Se_3 was then encapsulated by 40-nm-thick Al_2O_3 through thermal ALD (Oxford Plasmalab 80PLUS OpAL ALD) at 150 °C. To ensure good contact between the electric probe and metal pads while applying electrical pulses, the Al_2O_3 on the metal contacts was removed by defining a window using a sixth EBL with 600 nm PMMA, then etching in a chlorine-based inductively coupled plasma etcher (ICPRIE, Oxford PlasmaLab 100 ICP-18).

3.5 Optimizing the phase matching conditions through parameter sweep

In section 3.3 we discussed the difficulty in identifying the ideal phase matching conditions in experiments due to the deviation of nanoscale Sb_2Se_3 refractive index from the ellipsometry measured index. Here we sweep a large parameter space (coupling length and hybrid waveguide width) to find the optimal phase matching conditions. The bare Si waveguide width and the gap are fixed at 500nm and 400nm respectively. The Sb_2Se_3 is deposited in amorphous states onto the silicon waveguide and then lifted off using the same fabrication method stated in section 3.4 (doping was not performed to simplify the fab), after which the spectrum is measured. Rapid thermal annealing at 250°C is then used to transition the material into crystalline state and the spectrum is measured again. Fig. 3.4a shows one optimal design (L_c = 44.74μm, w_h = 460nm) where the crosstalk is less than -10 dB in both the bar and cross ports over 60 nm bandwidth, while insertion loss is ~0.56 dB and ~ 0.75dB in amorphous and

crystalline states, respectively. The slightly higher insertion loss in crystalline state is likely attributed to the higher loss of cSb_2Se_3. We can also see that near perfect phase matching is achieved at 1510nm when the Sb_2Se_3 is in amorphous state, where the cross state transmission is around 0dB and bar state transmission is as low as -21dB. A different design with a shorter coupling length (L_c=40.74 µm, w_h=440nm) is designed to be in the cross state for cSb_2Se_3 and bar state for aSb_2Se_3 (Fig. 3.4b). It exhibits lower insertion loss - ~0.54 dB and ~0.5 dB for amorphous and crystalline states, respectively, and small crosstalk of less than -10 dB, though with narrower bandwidth (~ 33 nm). Similarly, near perfect phase matching is observed at 1510nm when the PCM is in crystalline state. The results show that through careful optimization over a larger parameter space, low loss and high extinction ratio can be achieved simultaneously for both the cross and bar states.

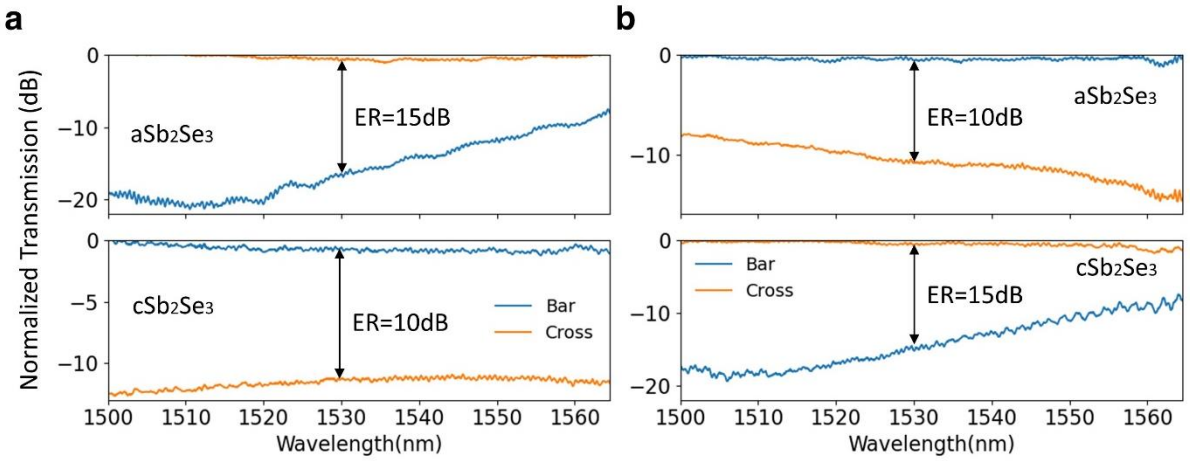

Figure 3. 4: Parameter sweeps to identify the phase matching conditions.

Measured spectra of directional coupler switches satisfying phase matching conditions near 1510nm in **a** amorphous state and **b** crystalline state.

3.6 Arbitrary trimming of racetrack resonator part I

Once the electrical control of waveguide coupling is realized using Sb_2Se_3, it becomes possible to individually control the coupling and the phase in a racetrack resonator. Such task

proves to be extremely challenging for the traditional thermo-optic phase shifters due to the thermal crosstalk and are power-hungry. In contrast, it can be realized readily using PCMs because the tuning is non-volatile. Fig. 3.5a shows the device schematic (top) and the optical micrograph of the fabricated device (bottom). We can individually control the coupling between the racetrack and the bus waveguide and the phase inside the racetrack, depending on the terminals (G1 or G2) that connect to the ground. Fig. 3.5b shows the fully reversible and complete control of the coupling region from the initial under-coupling state (no resonance) to critical coupling state (30dB extinction ratio). The schematic on the top shows the terminal that is grounded and the initial state of the device with spectrum plotted in the first row. Note that as the extinction ratio is changed, the resonance wavelength also blue shifts as changing the coupling will inevitably changes the optical phase inside the racetrack. This will be undesirable in applications such as trimming where the coupling of a microring should ideally be tuned at a fixed resonance wavelength. By changing the ground to G2, we can control the phase inside the racetrack without changing the extinction ratio of the resonance (Fig. 3.5c). If we simultaneously tune the coupling and the phase, we can compensate for the unwanted phase from changing the coupling, as shown in Fig. 3.5d. After phase compensation, the coupling can be tuned to multiple levels without changing the resonance wavelength. In section 3.7, we discuss in detail how the phase compensation is performed.

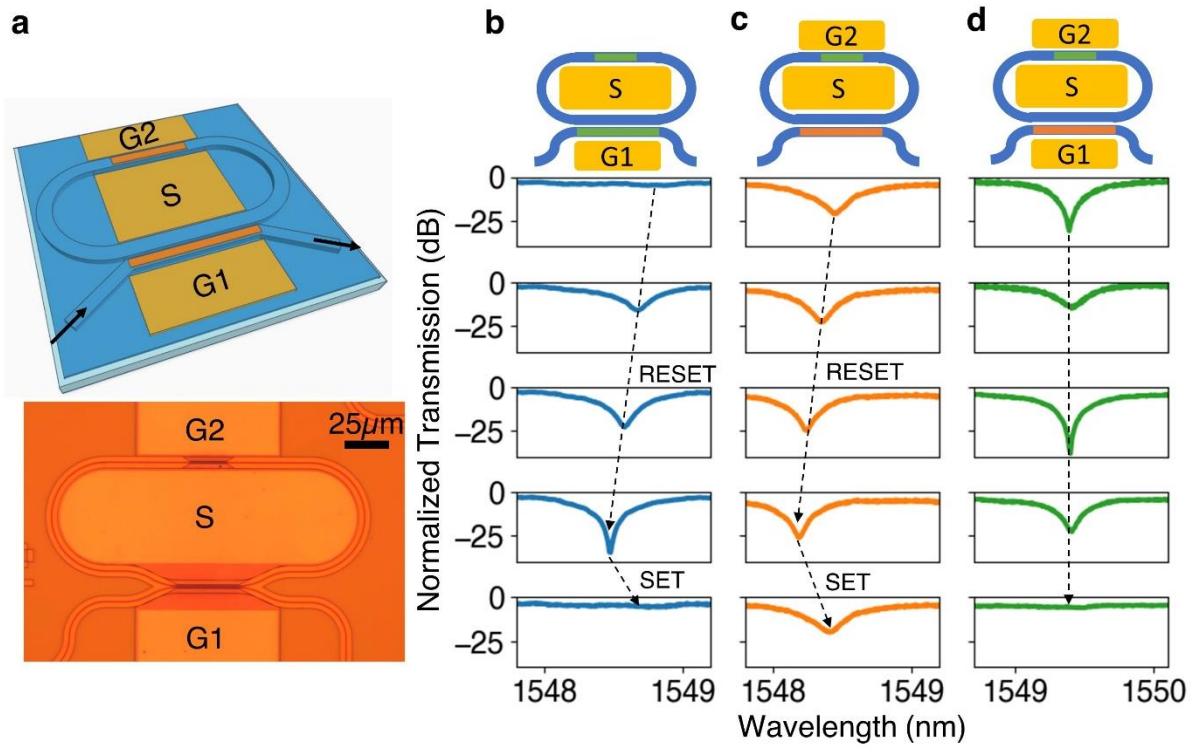

Figure 3. 5: Arbitrary trimming of a racetrack resonator.

a Schematic (top) and the optical micrograph (bottom) of the racetrack resonator. **b** Controlling the coupling between the racetrack and the bus waveguide. For RESET, pulses of 5.6V, 5.7V, and 5.8V were used with 400ns width and 8ns trailing edge. For SET, a pulse of 2.6V, 1.5ms width, 0.5ms trailing edge was used. **c** Controlling the optical phase inside the racetrack. For RESET, pulses of 5.3V, 5.4V, and 5.6V were used with 400ns width and 8ns trailing edge. For SET, a pulse of 2.7V, 1.5ms width, 0.5ms trailing edge was used. **d** Tuning the coupling without changing the resonance wavelength via phase compensation. The pulse conditions are discussed in section 3.6.

3.7 Arbitrary trimming of racetrack resonator part II

Fig. 3.5d shows that it is possible to tune the coupling of the racetrack without changing the resonance wavelength by simultaneously controlling the coupling and the optical phase. Here we show how the phase compensation was performed in Fig. 3.6. The pulse conditions are listed in Table 3.1 for excitations 1 to 12 labelled in Fig. 3.6. Currently the optimization is

performed manually, but this can be done automatically using scripts by minimizing the L_2 norm of the difference between the target resonance and current resonance wavelength.

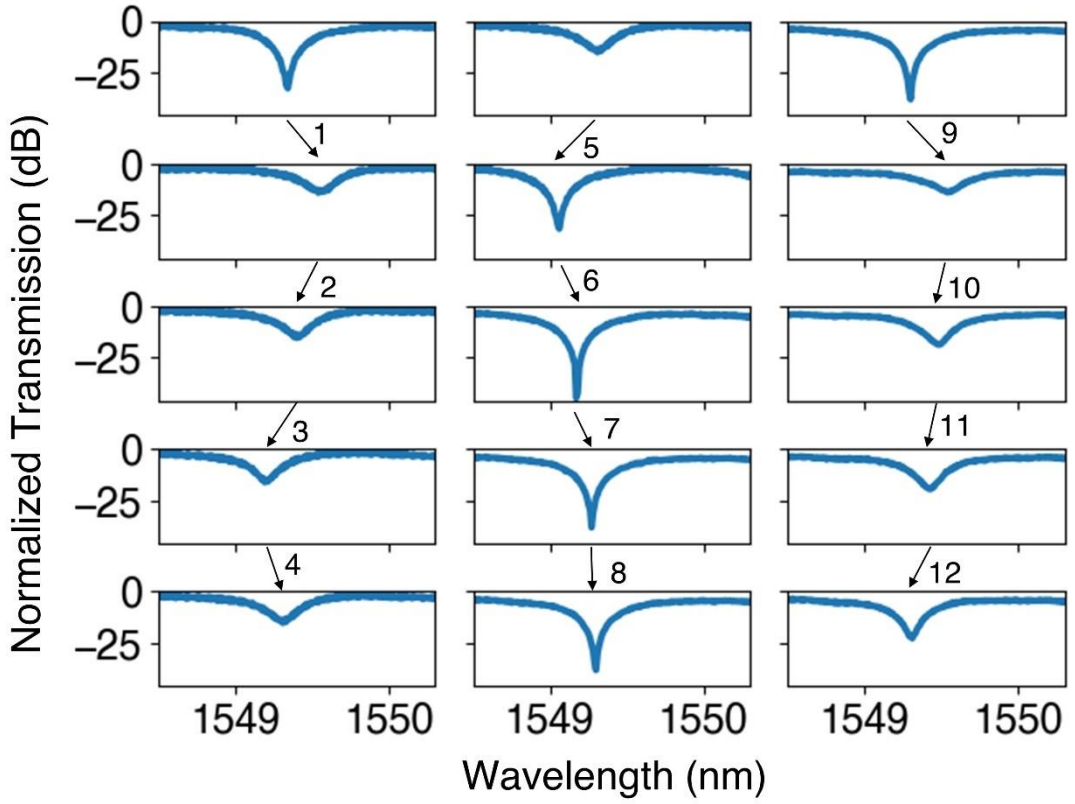

Figure 3. 6: Simultaneous tuning of coupling and phase in a racetrack resonator.

The pulse conditions for each step are detailed in Table 3.1 below. The first row shows the initial state of the resonance while the last row shows the resonance state after phase compensation.

Table 3. 1: Pulse conditions in Fig. 3.6.

	Phase or coupling?	Voltage(V)	Pulse width	Trailing edge
1	Coupling	2.7	1.5ms	0.5ms
2	Phase	6.2	400ns	8ns
3	Phase	6.3	400ns	8ns
4	Phase	2.2	1.5ms	0.5ms
5	Coupling	8.3	400ns	8ns
6	Phase	2.2	1.5ms	0.5ms

7	Phase	2.5	1.5ms	0.5ms
8	Coupling	2.5	1.5ms	0.5ms
9	Coupling	2.6	1.5ms	0.5ms
10	Coupling	8	400ns	8ns
11	Phase	5.8	400ns	8ns
12	Phase	5.93	400ns	8ns

3.8 Endurance of the photonic switches

Finally, we show excellent endurance of the switch of over 1,100 cycles, which is sufficient for infrequent programming of the PICs, such as trimming. Both the directional coupler switch (Fig. 3.7a) and the racetrack (Fig. 3.7b) can be switched for more than 2,300 times at >10dB extinction ratio, without significant degradation in the device performance. Note in Fig. 3.7a that the crystalline transmission suddenly becomes very stochastic at around 800th event. Meanwhile, the amorphous state transmission increases by around 1dB. By raising the SET amplitude by 0.2V at 1,250th switching, the randomness in the crystalline state is suppressed, before becoming random again at 1,500th switching. We think this is caused by over-resetting the PCMs into an inactive amorphous state. A portion of the PCMs becomes hard to crystallize, so higher temperature is required to re-activate this region. On the other hand, it is also possible to over-SET. Fig. 3.7b shows that the amorphous state is very stochastic in the first 1,200 events, but the crystalline state is less random, implying that the PCM is harder to be RESET. To reduce the variations, we raise the RESET amplitude by 0.2V and SET amplitude by 0.05V. The randomness in the amorphous state is substantially reduced but the variation in the crystalline state increase slightly. The results here show that although there is a wide range of conditions that can trigger the phase transition, only a few conditions can minimize the stochasticity in both states. Even if such conditions are

identified, for example in the first 800 events in Fig. 3.7a, one of the states can suddenly become stochastic during cycling. The pulse conditions need to be re-optimized to bring the switching back to a more deterministic state. A potential solution is to implement an optimization script to automatically find the optimal pulse condition by minimizing the L_2 norm of the difference between the target state and the current state. In practice, the devices do not have to be switched constantly (once every few hours) so once the optimal conditions are found the device can operate for a long time.

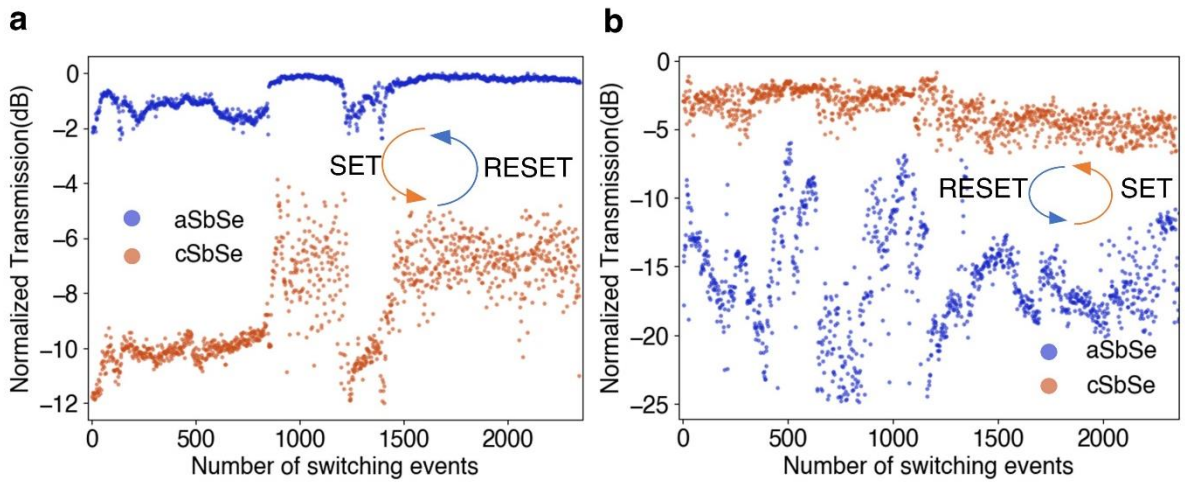

Figure 3. 7: Endurance tests of the photonic switches.

a Endurance test of the directional coupler switch measured at the cross port. For the first 1,250 events, the pulse conditions are 4V, 1.5ms, 0.5ms for SET and 11V, 400ns, 8ns for RESET. After 1,250th event, the SET pulse is changed to 4.2V, 1.5ms, 0.5ms. The RESET pulse remains unchanged. **b** Endurnace test of switching the coupling region in the racetrack resonator. The laser wavelength is parked near the resonance. The pulse conditions for the first 1,200 events are 2.2V, 1.5ms, 0.5ms for SET and 5.2V, 400ns, 8ns for RESET. After the 1,200th event, the SET pulse is changed to 2.25V, 1.5ms, 0.5ms and RESET pulse to 5.4V, 400ns, 8ns RESET.

3.9 Summary

In this chapter, we demonstrated a non-volatile ultra-compact directional coupler switch based on low-loss PCM Sb_2Se_3. The directional coupler has coupling length of only 33μm

and broad operating range of over 50nm. The extinction ratio is ~15dB and the loss is as low as ~0.5dB near 1530nm. We further showed the control of coupling in a racetrack resonator without changing the resonance wavelength via phase compensation. Finally, the photonic switches were testing over 1,150 cycles with >10dB extinction ratio. This project paves way to next-generation energy-efficient and compact programmable PICs.

Chapter 4. Ultra-low energy programmable nonvolatile silicon photonics based on graphene heaters

Silicon photonics is evolving from lab research to real world applications with the potential to transform many technologies, including optical neural networks and quantum information processing. A key element for these applications is a reconfigurable switch operating at ultra-low programming energy – a challenging proposition for traditional thermo-optic or free carrier switches. Recent advancements in nonvolatile programmable silicon photonics based on PCMs provide an attractive solution to energy-efficient photonic switches with zero static power, but the programming energy density remains high (hundreds of aJ/nm^3). In this chapter, we demonstrate a nonvolatile electrically reconfigurable silicon photonic platform leveraging a monolayer graphene heater with record-high energy efficiency and endurance. In particular, we show a broadband switch based on the technologically mature PCM $Ge_2Sb_2Te_5$ and a phase shifter employing the emerging low-loss PCM Sb_2Se_3. The graphene-assisted photonic switches exhibit an endurance of over 1,000 cycles and a programming energy density of 8.7 ± 1.4 aJ/nm^3 - within an order of magnitude of the PCM thermodynamic switching energy limit (~1.2 aJ/nm^3) and at least a 20-fold reduction in switching energy compared to the state-of-the-art. Our work shows that graphene is a reliable and energy efficient heater compatible with dielectric platforms, including Si_3N_4, for technologically relevant non-volatile programmable silicon photonics. Part of the chapter is adapted from my previous publication Ref. [10].

4.1 A graphene-PCM reconfigurable platform in silicon photonics

Our graphene-PCM hybrid switching platform consists of a patterned graphene bridge across a planarized 220 nm silicon-on-insulator (SOI) waveguide (Fig. 4.1a and 4.1b; see section 4.6

for fabrication methods). The layered view (Fig. 4.1b) shows that the PCM sits above the graphene which is transferred onto the waveguides. The 40 nm thick top Al_2O_3 acts as an encapsulation for both the PCM and graphene to prevent oxidation and PCM re-flowing during switching. There is an additional 10 nm ALD Al_2O_3 spacer between the graphene and PCM which isolates the two materials. This spacer prevents the rupture of graphene due to the tension caused by the volume expansion and contraction of PCM upon switching. The metal contacts are placed only 300 nm away from the 500 nm wide waveguide to reduce the graphene resistance while maintaining a low experimental metallic absorption loss of 0.002 ± 0.001 dB/μm. Such a low ohmic loss, despite the proximity of the metals to the waveguides, is made possible by the planarized waveguide geometry (see Fig. 4.5a), which keeps the optical mode away from the metal plane and minimizes the evanescent interaction. Graphene has a large contact area ($9.75\ \mu m \times 100\ \mu m$) with the metals to reduce the contact resistance, and it narrows at the bridge to restrict the current flow to the PCM region and to minimize the absorptive loss from graphene. The bridge region has a width W designed to be 200 nm longer than the length of the PCM and a length L fixed at 1.1 $\mu m = 0.3\mu m \times 2 + 0.5\mu m$. The optical micrograph of the fabricated device is shown in Fig. 4.1c, while Fig. 4.1d shows the false-color SEM of 2.85 μm × 400 nm GST patch on the waveguide, revealing excellent lithographic alignment accuracy.

Fig. 4.1e illustrates the operating principle of the graphene-PCM photonic switch. By applying a high amplitude and short voltage pulse, also know as a 'RESET' pulse, across the graphene bridge, the PCM is heated above its melting temperature T_l and rapidly quenched by removing the excitation. The melt-quench operation induces the amorphization of the PCM and transforms the PCM into the transparent and lower refractive index state. To return the PCM to its crystalline state, a low amplitude and long voltage pulse, as know as a 'SET' pulse, is applied across the graphene heater to heat the PCM above its crystallization

temperature T_x and below the melting point. The long trailing edge ensures slow cooling of the materials to complete crystallization. The material is then restored to the higher absorption and refractive index crystalline state. Two devices discussed below leverage the absorption and refractive index modification of the PCM actuated by graphene heaters to realize a broadband on/off switch and a low-loss phase shifter, respectively.

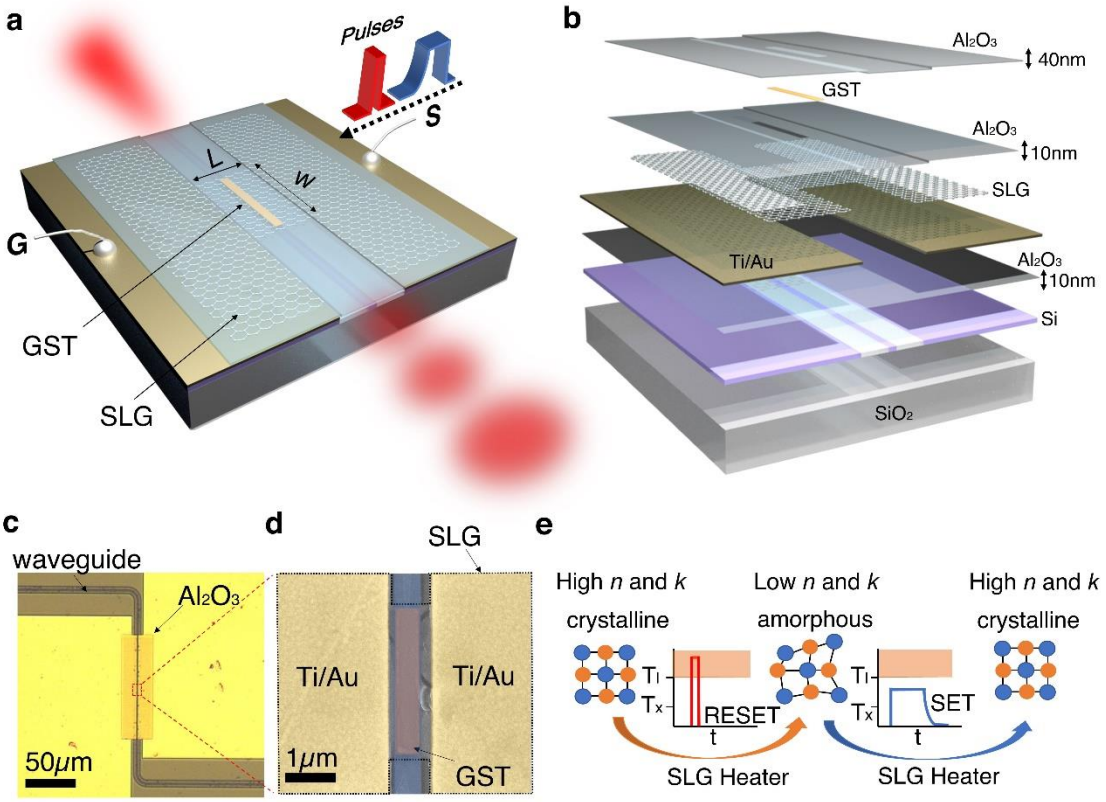

Figure 4. 1: A graphene-PCM reconfigurable silicon photonic platform.

a Schematic of the device structure. SLG stands for single-layer graphene. S (G), signal (ground) electrode. **b** Layered structure of the device. Note that an additional 10nm sputtered SiO_2 is used to encapsulate the Sb_2Se_3 which is not shown in the Figure. Such SiO_2 capping is not used for GST. **c** Optical micrograph of the waveguide switch. **d** False color SEM of the waveguide area where the GST is patterned. The SLG area is enclosed by the black dashed lines. **e** Operating principle of the device. T_l denotes the melting temperature and T_x denotes the crystallization temperature. *n* is the refractive index and *k* is the extinction coefficient.

4.2 Graphene-assisted broadband waveguide switch based on $Ge_2Sb_2Te_5$

We first demonstrate a broadband waveguide switch based on the absorption modulation of GST. GST undergoes a large change in complex refractive index upon phase transitions, which gives rise to a remarkable modification of the optical mode of the GST-clad waveguide (See Fig. 4.5). Although strong optical absorption of GST in the crystalline state makes it undesirable for phase-only control in the near infrared (NIR), the amplitude modulation of GST across a wide wavelength range is attractive for applications such as photonic memory[50] and optical computing[51]. Fig. 4.2a shows the reversible switching of the waveguide spectrum between low (crystalline GST) and high (amorphous GST) transmission states for 8 consecutive cycles using the device structure shown in Figs. 4.1c and 4.1d. The shaded regions of the spectra indicate the standard deviation between the 8 switching cycles, clearly revealing the excellent cycle-to-cycle reproducibility. A contrast of 3 dB in transmission is observed across the entire telecommunication C-band with 4.73 μm long, 23 nm thick GST. Temporal trace measurements (Fig. 4.10a) confirm that the change is indeed nonvolatile and hence caused by the GST. The 0.74 dB/μm optical contrast is slightly lower than GST directly on top of the waveguides[27] since there is a 20 nm Al_2O_3 spacer between the GST and waveguide, but agrees well with the optical mode simulations (see Fig. 4.5a). Heat transfer simulation also confirms that the temperature has reached the required threshold temperatures for both crystallization and amorphization of GST (see Fig. 4.5b). The total switching energy for amorphization is 5.55 nJ, corresponding to an energy density of 127.6 aJ/nm^3 and the energy dissipated by the graphene heater alone (i.e., excluding the power loss at the contact resistance) is only 0.380 ± 0.062 nJ, equivalent to an energy density of 8.74 ± 1.42 aJ/nm^3 (see section 4.3 for estimating the graphene sheet resistance and switching power). This represents over 20-fold reduction in the programming energy density compared

to the state-of-the-art[52] and within an order of magnitude of the ~1.2 aJ/nm^3 fundamental limit[53]. Finally, we showed high endurance of the device by performing 1,500 switching events on the graphene-GST photonic switch, as shown in Fig. 4.2b. A ~0.5 dB improvement in switching contrast is observed at ~600th switching event (pulse conditions remain unchanged) which is likely attributed to larger crystalline domain forming from the initial 'conditioning' steps[50]. It was found that the initial pulsing of the PCMs could give rise to ordered structures that act as seeds for subsequent crystal growth with minimal nucleation[54]. As a result, a larger volume of the PCM can be switched or 'activated'.

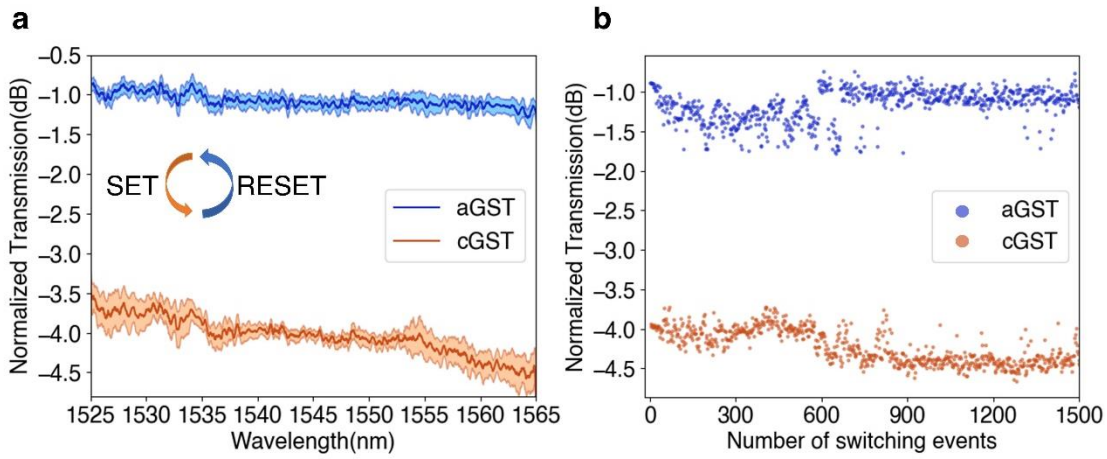

Figure 4. 2: Graphene-assisted broadband waveguide switch based on GST.

a Reversible switching of GST using graphene heater on SOI waveguide. The switching conditions are 3V, 100µs pulse width, 120µs trailing edge for SET and 5V, 400ns pulse width, 8ns trailing edge for RESET. 8 consecutive cycles are plotted where the shaded area indicates the standard deviation between the cycles and the solid line indicates the average. The device spectrum is normalized with the spectrum of a bare waveguide. **b** Cyclability of the switch for 1,500 switching events. The pulse conditions are the same as in **a**. Each pulse is temporally separated by 2s to ensure long thermal relaxation. The transmission is normalized with the transmission of a bare waveguide. aGST (cGST), amorphous (crystalline) GST.

4.3 Graphene sheet resistance and estimation of the switching power

The sheet resistance of the single layer graphene (SLG) is extracted by an array of test devices next to the photonic switches with different lengths and widths of SLG connecting to metal contacts (Fig. 4.3a). The resistance is measured at 0.1mV DC bias and plotted against the SLG length (Fig. 4.3b). The sheet resistance is extracted by fitting the equation

$$R_{total} = 2R_{contact} + R_{sheet}\frac{L}{W}$$

to the experimental data. We extract the lowest sheet resistance $R_{sheet} = 551 \pm 91\Omega/sq$ at 10μm width and a contact resistance of $R_{contact} = 919 \pm 261\Omega$, as shown in Fig S3c. Ideally speaking, the SLG sheet resistance should not depend on the width, but in reality, we found they are positively correlated. This is because the larger the SLG area, the more it is prone to defects such as pores and wrinkles, which means to obtain a low R_{sheet} it is essential to reduce the graphene area between the electrodes. To further reduce the SLG sheet resistance, hBN encapsulated SLG can be transferred mechanically, enabling high mobility charge transport[55]. On the other hand, Fig. 4.3c also shows that a large contact width between the SLG and the metals is required to reduce the $R_{contact}$. 1D edge contacts can be made to obtain ultra-low contact resistance and hence reduces the power loss in the contacts[56]. The total resistance of 1961±542Ω matches very well with the total resistance ~2000Ω that we measured from the SLG-PCM photonic switches.

To extract the programming energy per bit we measured the I-V curve of the devices to determine the power consumption. Fig. 4.3d shows the I-V curve from 2V to 5.2V of the ~5μm wide SLG heater that is used to switch the GST on SOI in the main text. The power is calculated to be 13.9mW (amorphization) and 5.37mW (crystallization), which gives the total energy per bit of 5.55nJ (400ns pulse width, amorphization) and 860.71nJ (100μs pulse

width, 120μs trailing edge, crystallization). Although crystallization occurs at lower power than amorphization, it consumes higher energy as the pulse width and trailing edge are longer. The programming energy density can then be estimated by dividing the energy by the PCM volume. The GST volume is calculated to be 23nm×4730nm×400 nm, where the area is measured by SEM and thickness is measured by ellispometer. This yields an energy density of ~127.6aJ/nm^3 (amorphization) and ~19.78fJ/nm^3 (crystallization). However, a significant amount of power is lost in the contact resistance and does not contribute to heating the PCM. We now use the R_{sheet} extracted above to estimate the energy consumed solely in the heater region. The power consumed by the SLG heater region can be expressed as

$$P_{SLG} = I^2 R_{sheet} \frac{L}{W}$$

I is the measured current from the I-V curve (2.78mA at 5V for GST), *L* is the heater length which is measured to be 1.1μm, and *W* is the heater width which is measured to be 4.93μm. The programming energy consumed by the SLG heater alone is therefore 0.380±0.062 nJ (amorphization) and 63.3±10.3 nJ (crystallization). The programming energy density is 8.74±1.42 aJ/nm^3 (amorphization) 1.45±0.24 fJ/nm^3 (crystallization). This is a 20-fold reduction compared to the previous work using SLG heater, where the contact resistance was also subtracted[52], and 70-fold reduction compared to the most energy-efficient doped Si heater[27].

The programming energy for the SLG-Sb_2Se_3 phase shifter can be extracted in a similar fashion. The total switching energy for amorphization is ~9.25 nJ and the energy density is ~128.4 aJ/nm^3. The energy dissipated by the SLG heater alone (i.e., excluding the power loss at the contact resistance) is 0.57 ± 0.09 nJ, and the energy density is 7.90±1.28 aJ/nm^3. The total switching energy for crystallization is 1280 nJ and energy density is 26.67 fJ/nm^3. The

energy consumed by the SLG heater alone is 78.7 ± 12.8 nJ and the energy density 1.09±0.18 fJ/nm^3.

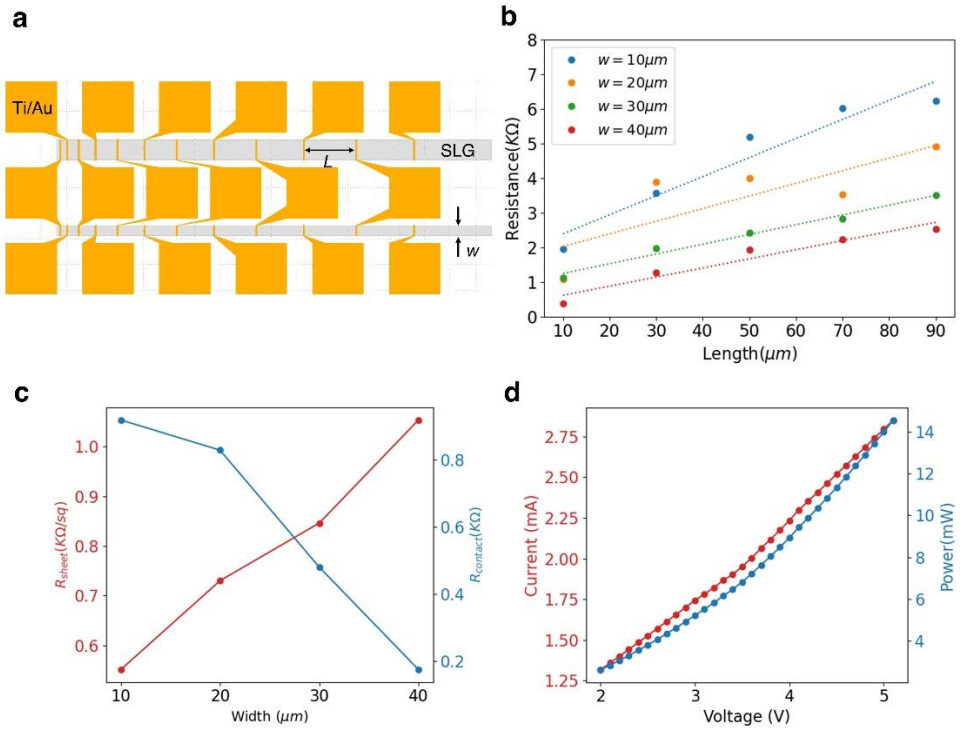

Figure 4. 3: Graphene sheet resistance and I-V curve.

a Device schematic for characterizing the SLG sheet resistance. *W* is the SLG width while *L* is the SLG length. **b** Resistance of SLG of different widths against lengths. The resistance is measured at DC applied bias of 0.1mV. **c** The extracted sheet resistance and contact resistance of SLG against the width. **d** I-V curve of the SLG-GST device tested in the main text from 2V to 5.2V.

4.4 Graphene-assisted low-loss phase shifter based on Sb_2Se_3 in a microring resonator

Phase shifters are frequently used in PICs to realize Mach-Zehnder modulators and 1×2 or 2×2 switches. The large optical absorption of GST in the crystalline state prohibits its use for phase-only modulation. Here, we employ the recently reported[20], [25] low-loss PCM Sb_2Se_3 to realize a graphene-assisted non-volatile phase shifter in a microring resonator. We harness the transparent window of Sb_2Se_3 in the NIR, where a negligible insertion loss of

0.002 ± 0.002 dB/μm of the Sb_2Se_3-loaded waveguide is extracted using a cutback method at 1550 nm (see Fig. 4.5). The device schematic is illustrated in Fig. 4.4a and the optical micrograph of the device is shown in Fig. 4.4b, while Fig. 4.4c shows the false-color SEM of a 6 μm long, 400 nm wide, and 30 nm thick Sb_2Se_3 patch on a waveguide. Reversible tunning of a microring resonance at 1549 nm is shown in Fig. 4.4d, where the spectra of three cycles are plotted and the shaded regions indicate standard deviations between the cycles.

The total switching energy for amorphization is 9.25 nJ (128.4 aJ/nm^3) and the energy dissipated by the graphene heater alone (i.e., excluding the power loss at the contact resistance) is only 0.57±0.09 nJ and 7.9±1.3 aJ/nm^3 (see section 4.3 for estimating the graphene sheet resistance and switching power). A maximum resonance shift of 0.021 nm is extracted which corresponds to a phase shift of 0.014π and $V_\pi \cdot L$ of 0.291V·cm (assuming a switching voltage of 6.8 V), representing a three-fold improvement compared to the state-of-the-art silicon PN phase shifter[57]. The phase shift matches the simulation (see Fig. 4.5) but is smaller than the recent reported value[58] due the intrinsic smaller index change in our Sb_2Se_3 and the use of 20 nm Al_2O_3 spacer. The increase in insertion loss (IL) of Sb_2Se_3 in crystalline state can be extracted by fitting the Q factor of the resonances which is estimated to be 0.006 ± 0.002 dB/μm. The IL from the metal and graphene is estimated to be 0.002 ± 0.001 dB/μm and 0.047 ± 0.006 dB/μm respectively from fitting the microrings spectra after each overlay step. The total IL is only ~0.33 dB for a device of 6 μm in length. The graphene IL is slightly lower than the loss measured in a similar graphene-on-microrings structure[59], where an IL of ~0.07 dB/μm was extracted. The reduction in the graphene IL in our work is likely attributed to lower carrier density and the 10 nm ALD Al_2O_3 spacer between the graphene and the waveguides, compared to 3 nm hBN used in the previous work[59]. Optical

losses in graphene can be further suppressed via electrical gating to the Pauli blocking region[60, p.], [61].

Lastly, we demonstrated excellent endurance of the device by performing 2,000 switching events on the phase shifter, as shown in Fig. 4.4e. The laser wavelength is slightly detuned from the resonance wavelength to mitigate the transmission fluctuations from the thermal drift. The gradual increase in transmission with cycling time shown in Fig. 4.4e is caused by the temperature-induced drift of resonance wavelength away from the initial laser wavelength (see section 4.13). The temporal trace after 1,100 cycles still shows a large optical contrast of 7 dB (Fig. 4.10b.) as the laser wavelength is parked near the resonance. Transmission measurements taken between the switching events (duration of 2s) indicate the change is nonvolatile and is indeed caused by Sb_2Se_3. The transient reponse of the switching is characterized by a 150MHz fast photoreceiver (see Fig. 4.11). Finally, we compare our graphene-PCM hybrid platform to other electrical switching approaches in PCM-based photonics (Fig. 4.6). It can be clearly seen that our graphene-PCM switch not only exhibits one of the highest endurances (> 1,000 cycles), but also produces the lowest switching energy density (8.7 ± 1.4 aJ/nm^3) reported so far.

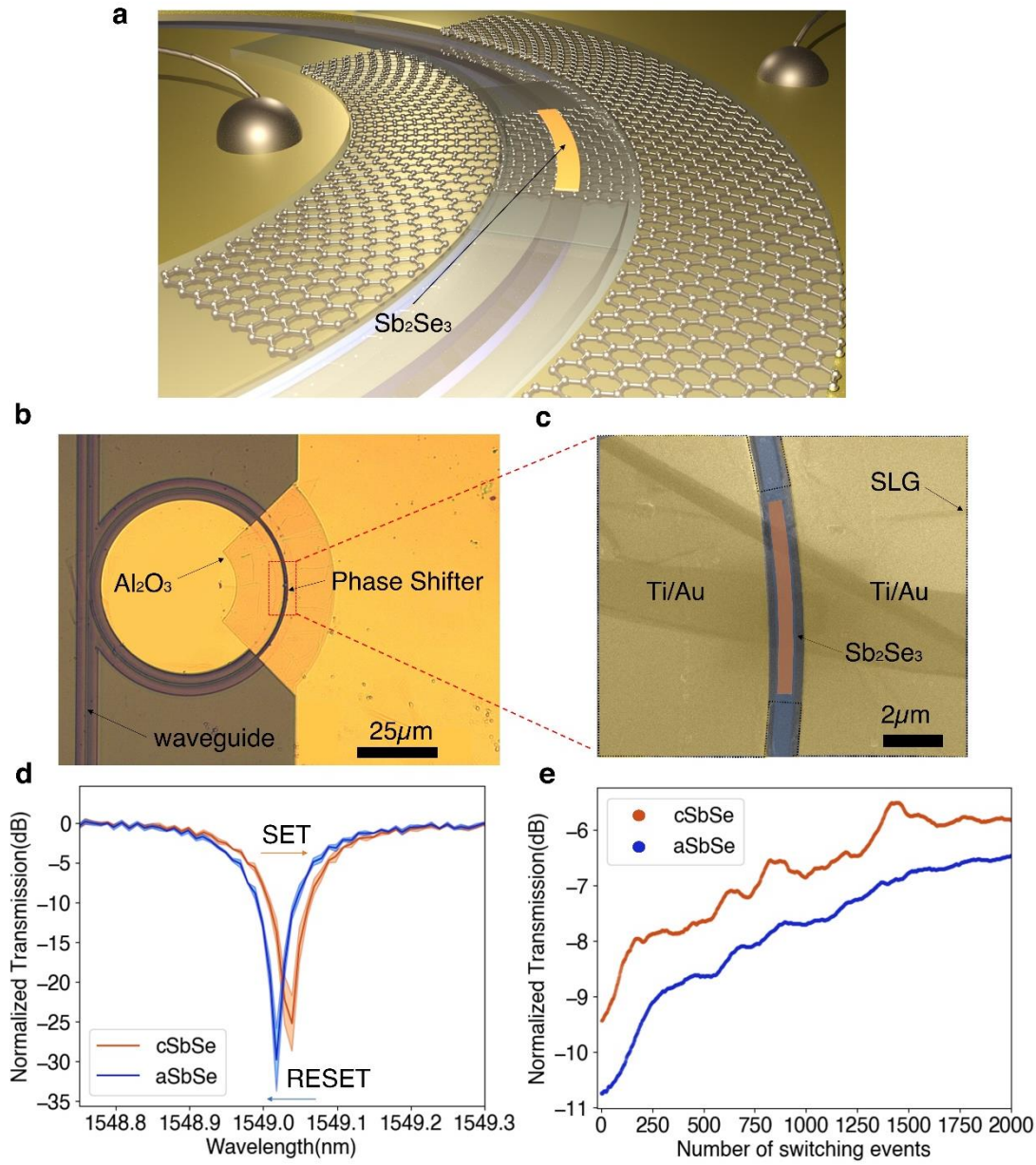

Figure 4. 4: Graphene-assisted phase shifter based on Sb_2Se_3 in a microring.

a Schematic of the graphene-Sb_2Se_3 phase shifter in a microring. **b** Optical micrograph of the microring resonator integrated with a phase shifter. **c** False-color SEM of the microring area where the Sb_2Se_3 is patterned. The graphene area is enclosed by the black dashed lines. **d** Reversible switching of Sb_2Se_3 using graphene heater on microrings. The switching conditions are 4V, 100μs pulse width, 120μs trailing edge for SET and 6.8V, 400ns pulse width, 8ns trailing edge for RESET. Three consecutive cycles are plotted where the shaded area indicates the standard deviation between the cycles and the solid line indicate the average. The spectrum is normalized with the spectrum of a bare waveguide. **e** Cyclability of the switch for 2000 switching events. The switching conditions are 4V,

100μs pulse width, 120μs trailing edge for SET and 6.4V, 400ns pulse width, 8ns trailing edge for RESET. Each pulse is temporally separated by 2s to ensure long thermal relaxation. The transmission is normalized with the transmission of a bare waveguide. The data is filtered by a 50-point moving average to reduce fluctuation caused by thermal noises.

4.5 Optical mode and heat transfer simulations

Here, we present the optical and heat transfer simulation results which are compared to the experimental results. The mode simulation is performed using Lumerical Mode solutions while the heat transfer simulation is performed using COMSOL Multiphysics heat transfer and electric current modules. Fig. 4.5a left panel shows that the fundamental quasi-transverse electric (TE) mode at 1550nm is confined in the SLG-GST cladded planarized waveguide and there is a large optical attenuation change $\Delta\alpha = 0.79\ dB/\mu m$ due to the phase transition of 23nm GST. This matches well with our experiments where we extract an attenuation change of $0.74\ dB/\mu m$ and confirms that we have fully changed the entire volume of GST. The small discrepancy is due to the batch-to-batch fabrication variations in deposited material thickness, dimensions, and etched waveguide dimensions. The change in extinction coefficients of GST in amorphous and crystalline states on silicon waveguides is extracted from a cutback measurements using microrings as discussed in our previous works[9], [19], [27]. The optical constants extracted from ellipsometry measurements are not used in the mode simulations because we found a large variation in optical constants as the material is reduced to nanoscale dimensions[9]. Similarly, the right panel of Fig. 4.5a shows the TE mode profiles of 30nm Sb_2Se_3 cladded SOI planarized waveguides with SLG. We use a cutback method to extract the on-waveguide optical constants of Sb_2Se_3 (See section 4.5 below) which are used in simulations. Since the refractive index change of Sb_2Se_3 is much smaller than that of GST, the shape of the optical mode remains roughly unchanged before and after phase transition. We calculated near zero loss in the simulation and a small change

in the effective index $\Delta n_{eff} = 0.0017$. Such change is smaller than the recently reported value[58] but is consistent with our experimental extracted value of $\Delta n_{eff} \approx 0.0011$. We attribute the small discrepancy between the simulation and experiment to the fabrication variations and the slight reduction of material volume upon crystallization which we have neglected in simulation. Based on ellipsometry, we found ~11% reduction in Sb_2Se_3 thickness upon crystallization. Despite having smaller index change, the Sb_2Se_3 used in our work exhibits almost three times lower absorption loss in crystalline state (0.006 ± 0.002 dB/μm) compared to a recent work[58] and hence is highly desirable for phase shifter applications.

Next, we show that the PCMs have indeed reached the phase transition temperature by inputting the experimental conditions into the heat transfer model in COMSOL Multiphysics. The top panel of Fig. 4.5b shows that when we specify a current of 2.78mA (measured in experiments) and 400ns pulse width, the GST temperature reaches $\sim 700^o C$, $\sim 100^o C$ above the melting temperature of GST. The short trailing edge of 8ns ensures the melt-quench of the GST into the amorphous state. Similarly, by injecting 1.79mA (measured in experiments) into the SLG heater with a pulse width of 100μs, the GST is heated to $\sim 400^o C$. The 120μs long trailing edge ensures the slow cooling of GST so that it settles into the crystalline state. The experimentally extracted SLG sheet resistance of 551±91 Ω/sq is used in the simulations.

Fig. 4.5c shows the temperature distribution in the cross-section of the device at the end of amorphization pule (t=400ns, top panel) and crystallization pulse (t=100μs, bottom panel). It can be seen from the heat distribution that the SLG heater exhibits an improved heating efficiency due to a two-fold effect. First, the SLG only has an atomically thin heating volume which significantly reduces the energy wastage, compared to a doped Si heater which has a gigantic heating volume coming from the 220nm thickness[27]. Secondly, the SLG and PCM are surrounded by ALD Al_2O_3 encapsulation top and bottom, which creates a large thermal

boundary resistance between the SLG and the silicon slab below. This considerably reduces the heat dissipation into the silicon slab. Such phenomenon is clearly visible in the temperature distribution (Fig. 4.5c) where the heat is shown to be mainly confined in the SLG/PCM/Al_2O_3 thin film stack while the temperature of the silicon slab remains to be low.

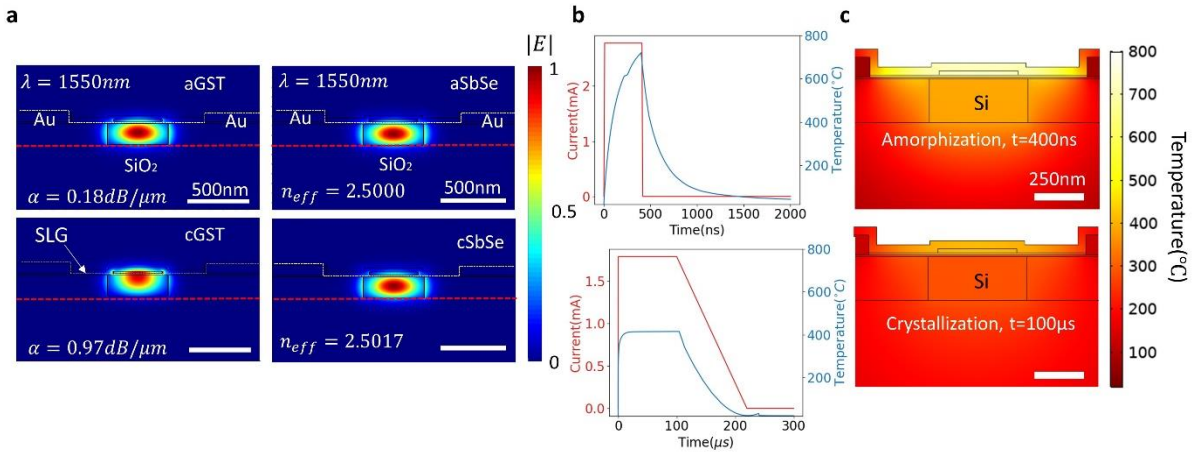

Figure 4. 5: Optical mode and heat transfer simulations of the SLG-PCM photonic switch. **a** Simulated fundamental TE mode profiles of 23nm GST (left panel) and 30nm Sb_2Se_3 (right panel) on planarized SOI waveguides at 1550nm. The optical constants of GST and Sb_2Se_3 at 1550nm are extracted from cutback measurements using microring resonators. The white dashed lines indicate the presence of SLG in the simulation. The red dashed lines indicate the boundaries between the device layer (220nm Si) and the buried oxide. **b** Simulated temperature variation with time under the measured current for amorphization (top) and crystallization (bottom). The red curves indicate the injecting current while the blue curves indicate the temperature of GST. **c** Simulated temperature distribution at 400ns under injecting current of 2.78mA (top) and at 100μs under current of 1.89mA (bottom).

4.6 Cutback measurement of Sb_2Se_3 on microrings

To evaluate the actual refractive index change and the loss of nanoscale Sb_2Se_3 on waveguides, we design a cutback measurement where the length of the Sb_2Se_3 cladded on 220nm fully etched silicon microrings is increased from 0μm to 80μm. Fig. 4.6a shows the

SEM of a Sb_2Se_3 cladded microring where the PCM is only placed on top of the waveguide. Fig. 4.6b shows the waveguide cross-section measured by Atomic Force Microscope (AFM), indicating the thickness of the Sb_2Se_3 is 20nm. The loss and spectral shift with respect to the length of Sb_2Se_3 are plotted in Fig. 4.6c and 4.6d, respectively. A few data points show negative loss values due to fabrication variations such as resist residue and liftoff imperfections. By fitting the data, we extracted experimentally Δn_{eff} and Δk_{eff} as summarized in the table below using methods discussed in our previous works[9], [19]

	Experiment
$\Delta\lambda(\mathrm{nm}/\mu\mathrm{m})$	0.035±0.000
Δn_{eff}	0.007±0.000
$\Delta\alpha(dB/\mu m)$	0.002±0.002
Δk_{eff}	$6 \times 10^{-5} \pm 6 \times 10^{-5}$

Finally, using the mode simulations, we estimate a $\Delta n \approx 0.008$ and a near zero extinction coefficient from the phase change of nanoscale Sb_2Se_3 on waveguides. These values are used to model the phase shift and insertion loss in our actual electrical switching devices.

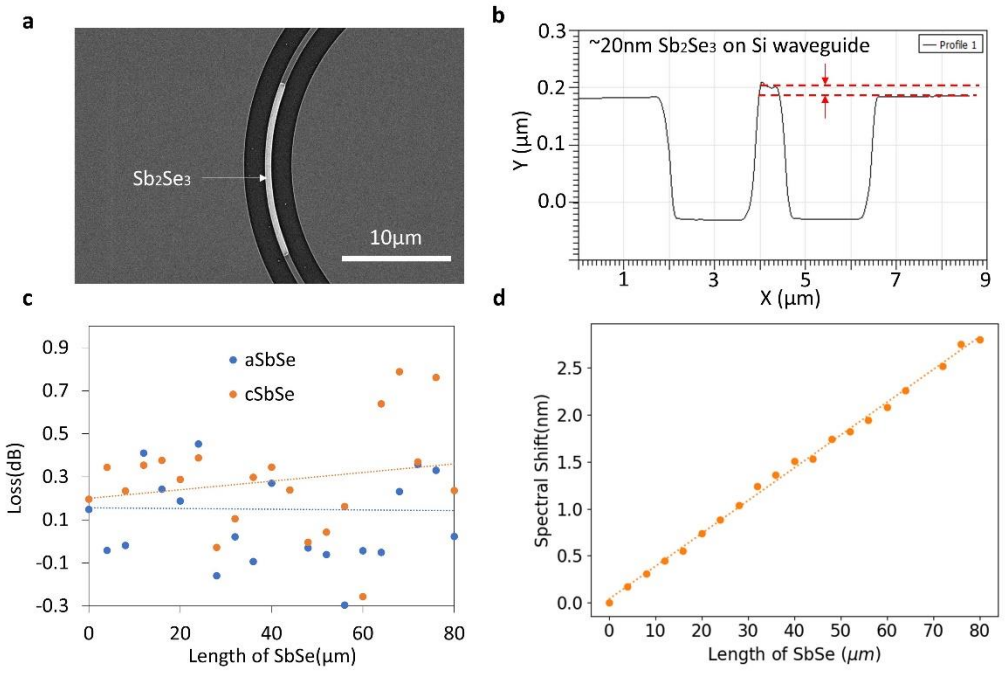

Figure 4. 6: Extracting the insertion loss and effective index change of Sb_2Se_3 using microrings.

a SEM showing the Sb_2Se_3 material is patterned on top the silicon microring resonators. **b** AFM measured cross-section of the waveguide with 20nm Sb_2Se_3 on top. **c** The extracted insertion loss of the Sb_2Se_3 in both the amorphous and crystalline states against the length. **d** The extracted spectral shift caused by the Sb_2Se_3 phase change against the length.

4.7 Comparison to other non-volatile electrically reconfigurable photonic platforms

We now compare our graphene-PCM hybrid platform to other electrical switching approaches in PCM-based photonics. Fig. 4.7 plots the number of switching cycles demonstrated against the programming energy density of recent works reporting electrical tuning of PCMs in photonics. We emphasize that the number of cycles demonstrated does not reflect the ultimate limit of PCM technologies since much higher cycle number[53] has been demonstrated in the electronic memory before. In fact, we anticipate an increased number of cycles will be eventually realized in phase-change photonics as well. Our result shows the state-of-the-art in phase-change photonics and serves as a general guide to researchers when it comes to the choice of microheaters for phase-change photonics. The programming energy density is defined as the switching energy per unit volume of PCMs for complete phase transition, $\frac{E_{switch}}{V_{PCM}}$. The normalization with respect to PCM volume will ensure a fair comparison between different heater/switch geometries without considering the device architecture. Specifically, a microring and waveguide-based modulators will have vastly different switching energy due to the photon storage in the microring, but similar switching energy density. Here, we focus on low-loss conductors including doped silicon, TCOs, and graphene as they afford low insertion loss for integrated photonic applications. It can be seen that doped silicon[28], [58] and PIN[27] heaters generally have remarkable endurance with the highest demonstrated cyclability of 500 cycles using a PIN heater[27]. However, they are all plagued by relatively

high programming energy which lies between 600 and 800 aJ/nm^3, indicated in the grey region. The low energy efficiency is a result of large heating volume due to severe heat dissipation into silicon. For example, in order to change ~10-20 nm thick PCM, a 220 nm thick silicon waveguide has to be heated up to the PCM melting point, leading to significant power waste[24]. Lastly, such heaters cannot be used with materials that cannot be doped, such as Si_3N_4. On the other hand, TCO heaters have programming energies that are drastically different[32], [62], [63, p.]. This is in contrast to the theoretical calculation,[24] which predicts comparable energy efficiency between the silicon and ITO heaters. We attribute this to the substantial property variation between different growth conditions[64]–[66] of TCOs, whereas the growth and doping conditions of silicon is relatively standardized. Although high endurance (1,000 cycles) was shown using a fluorine-doped tin oxide (FTO) heater[63], the switching is not demonstrated in integrated photonics and the energy efficiency is very low. Meanwhile, ITO heaters are more widely explored for integrated photonics but suffer from endurance issues[9], [32], [62]. Finally, we compare our work to the recent demonstration of graphene heater for tuning $Ge_2Sb_2Se_4Te$ (GSST)[52] where the reversible switching is demonstrated, yet not in PICs. The endurance of GSST on graphene heaters has yet to reach the same level as previously demonstrated using metal heaters[11]. Introducing a graphene heater drastically reduces the total programming energy to 186 aJ/nm^3 in the previous work and reaches staggeringly low switching energy of 8.7 ± 1.4 aJ/nm^3 in our approach, when the power loss due to the contact resistance is subtracted. The extracted switching energy is very close to the simulated value[24] of 6.6 aJ/nm^3 and within one order of magnitude of the 1.2 aJ/nm^3 fundamental thermodynamic limit of GST phase change[53]. Such ultra-low programming energy density represents a 20-fold reduction in energy compared to the previous graphene heater[52] and a 70-fold reduction compared to the most energy-efficient doped silicon heater reported in literature[27]. The high energy efficiency is

made possible primarily by the atomically thin heating volume of graphene which represents a ~650 times reduction in heating volume compared to the doped silicon for the same heater area. Secondly, the thermal boundary resistance between the graphene/Al_2O_3/Si thin film stack considerably limits thermal dissipation into the silicon underneath[24]. On the other hand, the 20-times improvement in the energy efficiency of this work compared to the previous work on graphene can be attributed to a heater design specifically optimized for PICs. Instead of using a large graphene area ($\sim 100\mu m \times 10.5\mu m$), most of which does not contribute to the heating of PCM, we reduce the extension regions down to only $\sim 0.3\mu m \times 5.2\mu m$. This confines graphene to the vicinity of the waveguide and PCMs (see Fig. 4.1), drastically minimizing the unnecessary heating and the power loss. In addition to energy efficiency, our work has also shown that graphene is a reliable heater with the highest cyclability of 1,000 cycles that has been demonstrated in electrically tunable phase-change PICs so far.

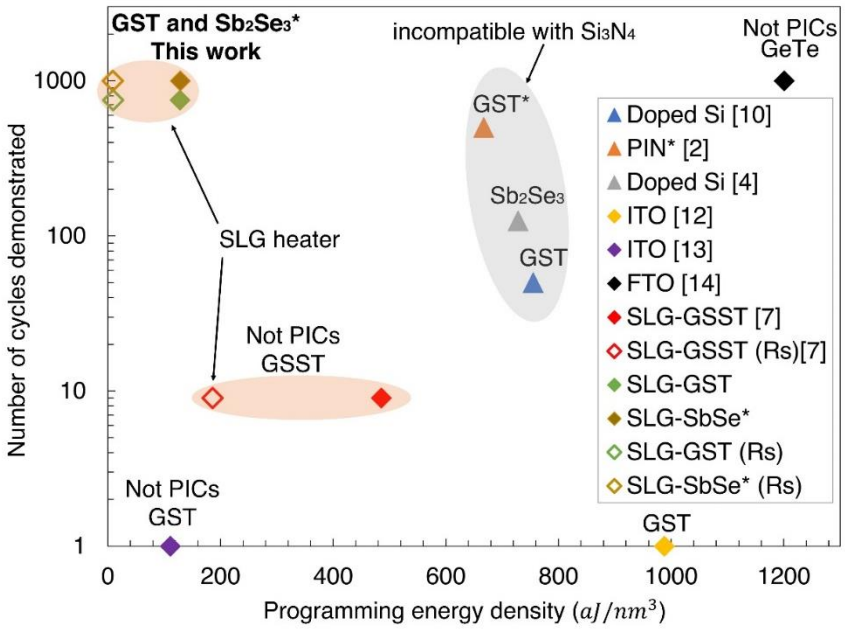

Figure 4. 7: Comparison to other nonvolatile electrically reconfigurable photonic platforms. Comparison of number of cycles demonstrated versus the programming energy density for doped Si[28], [58], PIN[27], TCOs[32], [62], [63], and graphene heaters[52]. The reference number is

denoted inside the parenthesis. 'Not PICs' indicates that the reversible switching of PCM was not achieved on a PIC platform. The diamond markers indicate that the heaters are compatible with Si_3N_4. The no-fill diamond markers indicate the programming energy calculated by considering only the graphene sheet resistance, also denoted by 'R_s'. The grey shaded area includes only the doped Si heaters that are compatible with SOI only. The red shaded areas include only the graphene heaters. 'GST', 'GSST', and 'SbSe' in the legend denote $Ge_2Sb_2Te_5$, $Ge_2Sb_2Se_4Te$, and Sb_2Se_3 respectively. The * in the legend indicates that the numbers are quoted for microrings.

4.8 Quasi-continuous multilevel phase modulation using the Graphene-Sb_2Se_3 phase shifter

It is well-known that PCMs can support multilevel operation and such property is widely-exploited in electronic memory[67], photonic memory[68], and most recently in optical neural networks[69]. After realizing the bistable switching, we further show that the phase shifter can be tuned quasi-continuously to attain multiple optical phase levels by controlling the programming energy. Fig. 4.8a shows that as the programming voltage is monotonically increased in steps of 0.1 V from 5.5 V up to 6.4 V (pulse width and trailing edge are fixed at 400 ns and 8 ns respectively), we attain an increasingly larger hot spot in the center of the heater, causing increasingly larger area of the PCM to be amorphized. As a result, the resonance dip shifts gradually to the shorter wavelength and these intermediate states correspond to partially amorphous PCMs. After 10 pulses of increasing amplitude, a SET pulse of 4V (100 μs pulse width and 120 μs trailing edge) is used to return the resonance to the original position. The resonance wavelength of the SET state perfectly matches the resonance wavelength of the initial crystalline state, as indicated by the grey dashed line in Fig. 4.8a. The time dynamic response is investigated by increasing the programming voltage by 0.2 V increments from 5.5 V to 6.9 V and the transmission is continuously monitored with respect to time, as shown in Fig. 4.8b. After each RESET operation, the PCM is returned to

the initial crystalline state by the same SET pulse of 4V. Eight distinct transmission levels can be clearly resolved with ~1 dB contrast between adjacent levels. To better quantify the multi-level phase modulation, we extract the phase shift from the change in the resonance wavelength corresponding to each RESET pulse and plot the phase shift against the programming energy (Fig. 4.8c). 14 phase levels can be attained by increasing the programming energy from 6 nJ to 9.5 nJ, where the phase increases linearly with the programming energy. Fig. 4.8d shows that the resulting change in transmission from the phase modulation matches very well with Fig. 4.8c. The reproducibility of the multi-level operation is evaluated in Fig. 4.12b for five iterations, showing that although the transmission levels are not entirely deterministic, the mean transmission increases with the programming energy almost linearly. Similarly, multilevel operations can also be realized in the graphene-GST waveguide switch where seven distinct transmission levels are obtained (Fig. 4.12a).

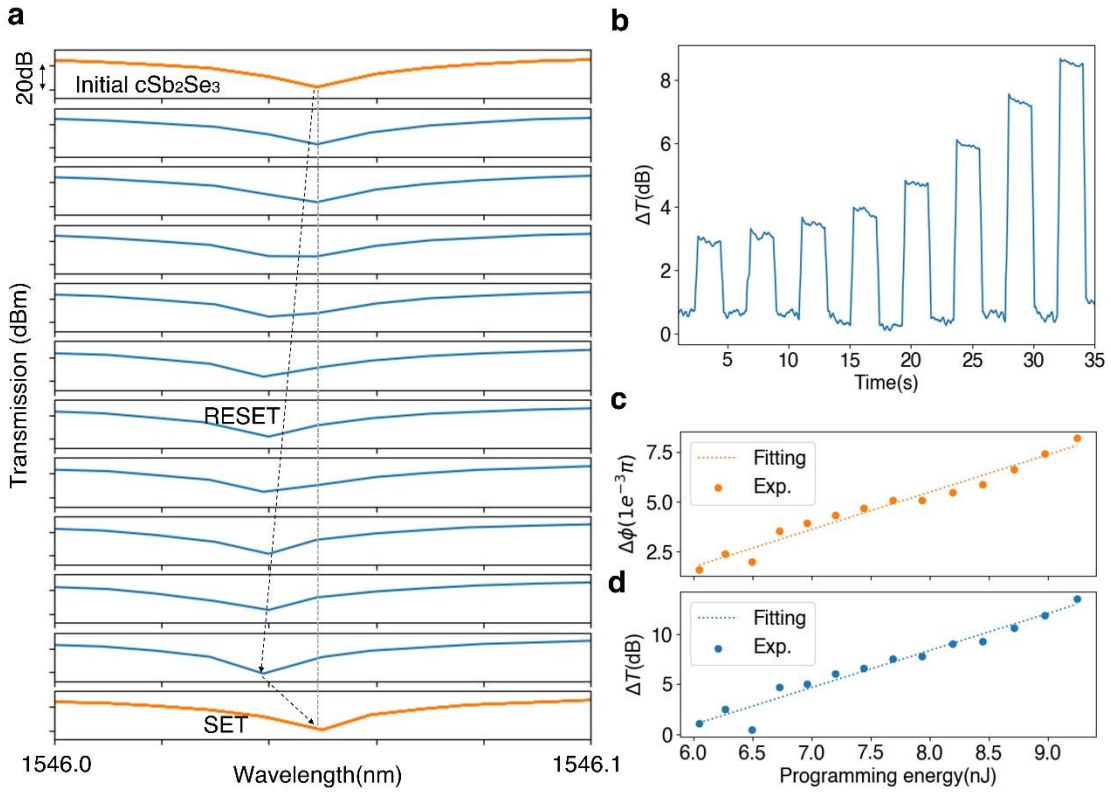

Figure 4. 8: Quasi-continuous phase modulation using the graphene-Sb_2Se_3 phase shifter.

a Quasi-continuous tuning of microring resonance by step amorphization. The SET conditions are 4V, 100μs pulse width, 120μs trailing edge. For RESET, the amplitude is increased monotonically from 5.5V to 6.4V and the pulse width and trailing edge are fixed at 400ns and 8ns. **b** Temporal trace of a continuous programming iteration with a monotonically increasing RESET pulse amplitude from 5.5V to 6.9V followed by a SET pulse. Eight transmission levels are clearly resolved. The pulse width and trailing edge of the RESET pulse are fixed at 400ns and 8ns. The SET conditions are the same as in **a**. **c** Change in phase shift ($\Delta\varphi$) with respect to the programming energy. 14 phase levels can be resolved where the phase shift increases linearly with the programming energy. **d** Change in transmission caused by the phase shift with respect to the programming energy. 14 transmission levels can be resolved. The transmission contrast increases linearly with the programming energy, matching very well with **c**.

4.9 Fabrication of graphene-PCM photonic switch

The graphene-PCM photonic switch is fabricated on a 220-nm thick silicon layer on top of a 3-μm-thick buried oxide layer (SOITECH). Fig. 4.9 shows the schematics of fabrication flow. The pattern is defined by a JEOLJBX-6300FS 100kV electron-beam lithography (EBL) system using positive tone ZEP-520A resist. 220 nm fully etched ridge waveguides are made by an inductively coupled plasma reactive ion etching (ICP-RIE) process in Florine-based gases. Before removing the resists, 220 nm SiO_2 is evaporated onto the resist-coated waveguides by electron beam evaporation. The lift-off of SiO_2 is completed by 3 mins sonication in methylene chloride, which leads to planarized waveguides. 10 nm of thermal atomic-layer-deposited Al_2O_3 (H_2O precursor at 150℃) is then grown on the substrate to prevent the formation of semiconductor and metal junction between the graphene and silicon. A second EBL exposure using positive tone poly(methyl methacrylate) (PMMA) resist is subsequently carried out to create windows for the Ti/Au deposition. After development, 5nm Ti followed by 100 nm Au was electron beam evaporated onto the chip. The lift-off of Ti/Au

was completed again by immersing the chip in methylene chloride. Monolayer graphene (Graphenea) grown by chemical vapor deposition (CVD) is transferred onto the chip by the standard PMMA wet transfer technique[70] and then patterned with EBL using the maN 2403 negative resist. O_2 plasma is used to etch away the graphene that is not protected by the resist which is followed by another 10nm thermal ALD Al_2O_3 capping layer to protect the graphene during the subsequent fabrication steps. The high quality of the transferred graphene on the fabricated devices is confirmed by Raman spectroscopy (See Fig. 4.13). The 5th EBL overlay step is used to expose the PMMA resist before depositing GST or Sb_2Se_3 via magnetron sputtering. 23 nm of GST is deposited via magnetron sputtering (Lesker Lab 18) using a GST target at 28 W DC power and a base pressure of ~5×10^{-7} Torr. The Ar flow rate is controlled to maintain a sputtering pressure of 3.5mTorr. The Sb_2Se_3 is sputtered using a magnetron sputtering system at 30 W RF power under a deposition pressure of 4 mTorr and Ar flow of 30 sccm. The deposition rate for Sb_2Se_3 is ~1 nm/min. Additionally, the samples are capped with 10 nm of SiO_2 sputtered in situ (150 W RF power, 4 mTorr pressure, and Ar flow of 30 sccm), to prevent oxidation during sample shipping. Several pre-and post-deposition treatments of the sputtering chamber were performed for the selenide deposition, including cleaning the chamber followed by annealing and O_2 plasma cleaning. Prior to Sb_2Se_3 deposition, the sputtering chamber is baked at 400ºC for 6 hours (under vacuum) followed by cooling down the chamber to room temperature to drive out gases and other contaminants. The toxic residual hydrogen selenide formed during Sb_2Se_3 deposition is removed by running oxygen plasma for 1 hour prior to opening the sputtering chamber. The atomic ratio of Sb_2Se_3 after deposition is confirmed using XPS to be Sb:Se ≈ 44:56 which is close to the sputtering target stoichiometry of Sb:Se ≈40:60. Immediately after lifting off the PCM in methylene chloride, a 40nm ALD Al_2O_3 is grown on the chip to protect the PCM from oxidation and reflowing during switching. To allow good electrical contacts between the probes and the

metal pads, the 6th EBL step is used to open windows in PMMA resist at the contact regions for Al_2O_3 etching. The Al_2O_3 on top of the contacts is etched away using ICP-RIE etching in Chlorine-based gases. Finally, the PCMs are initialized into the fully crystalline state by rapid thermal annealing (RTA) at 200°C for 10 min under N_2 atmosphere before measurements.

The patterned graphene does not peel off after subsequent fabrication steps because it is protected by 10nm ALD Alumina.

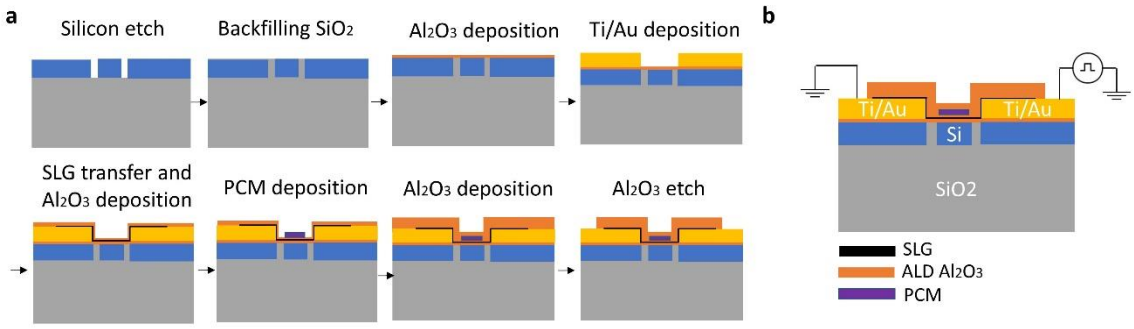

Figure 4. 9: Fabrication flow schematics of SLG-PCM reconfigurable silicon photonic platform. **a** Fabrication process flow of the SLG-PCM photonic switch. **b** The cross-section of the final fabricated device.

4.10 Temporal trace of SLG-PCM photonic switch and phase shifter

We continuously monitor the optical transmission over ten reversible switching events of the SLG-GST photonic switch (Fig. S4a) and the SLG-Sb_2Se_3 phase shifter in microrings (Fig. S4b) to show the dynamic response. The switching is deliberately paused for two seconds before the next excitation while the transmission is continuously measured. The transmission does not automatically fall back to the original state, indicating that the transition is indeed nonvolatile. The signal measured from the SLG-Sb_2Se_3 phase shifter is slightly noisier than the signal from the waveguide switch because the laser is parked near the resonance where the light intensity is very low. The up-shift and down-shift of the overall transmission background in Fig. S4b is caused by the resonance drifting from the temperature fluctuations.

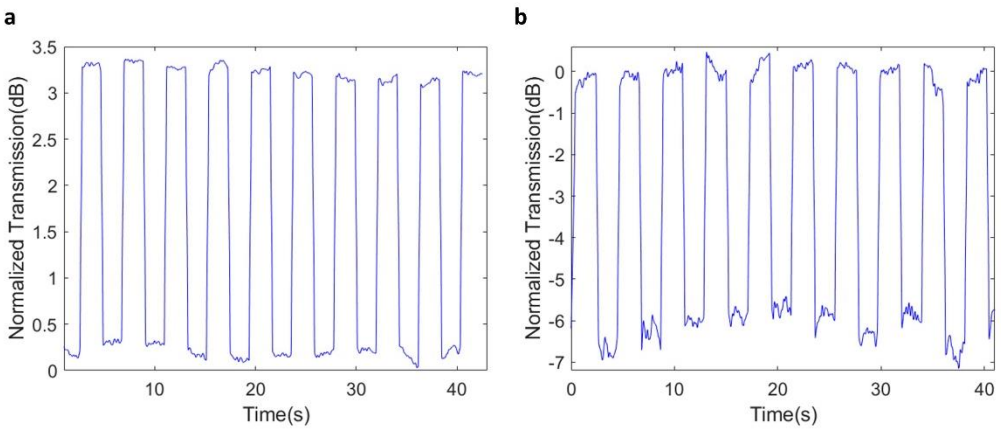

Figure 4. 10: Temporal trace of SLG-PCM photonic switch and phase shifter.

a Temporal trace of SLG-GST photonic switch for ten reversible switching events. The switching conditions are 3V, 100µs pulse width, 120µs trailing edge for SET and 5V, 400ns pulse width, 8ns trailing edge for RESET. **b** Temporal trace of SLG-Sb_2Se_3 phase shifter for ten reversible switching events. The switching conditions are 4V, 100µs pulse width, 120µs trailing edge for SET and 6.4V, 400ns pulse width, 8ns trailing edge for RESET. A two-second interval is used in **a** and **b** between consecutive switching events.

4.11 Transient response of SLG-PCM switches

We measured the response speed of SLG-Sb_2Se_3 waveguide switch using a 150MHz near IR fast photoreceiver (Thorlabs PDB450C). For crystallization, a 50µs wide pulse with 30µs trailing edge is applied to the heater at an amplitude of 8V. For amorphization, a 400ns wide pulse with 8ns trailing edge is applied to the heater at an amplitude of 19V. The relatively high voltage used is because of the high graphene resistance (~9KΩ) of the device under test. The small optical contrast is due to the small increase in optical absorption (~0.006dB/µm) in Sb_2Se_3. It can be seen that for crystallization, thermal relaxation takes longer time (~50 µs) due to the long pulse required. On the other hand, much faster response (~500 ns) is observed for amorphization thanks to the short excitation time (408 ns). The ultra-thin thermal mass of the graphene heater enables fast heat dissipation and hence short thermal relaxation, limited

only by the duration of excitation. While it is hard to completely decouple the switching time due to material phase change from thermal relaxation, we think the reponse time is mainly limited by the thermal relaxation, instead of phase transition. This is because the change in dielectric constant caused by phase transition typically occurs at picosecond time scale[71], while heat diffusion normally requires hundreds of nanoseconds. We, however, would point out that for most reconfigurable/ programmable photonics applications, switching speed is of low importance. The envisioned applications for PCM-photonics are programming a photonic circuit depending on the applications in hand. Due to the non-volatile nature of PCM, static power consumption will be zero, and that is where we get the benefit of using PCMs. In such applications, it does not matter how fast we are programming the circuit, as the programming happens occasionally.

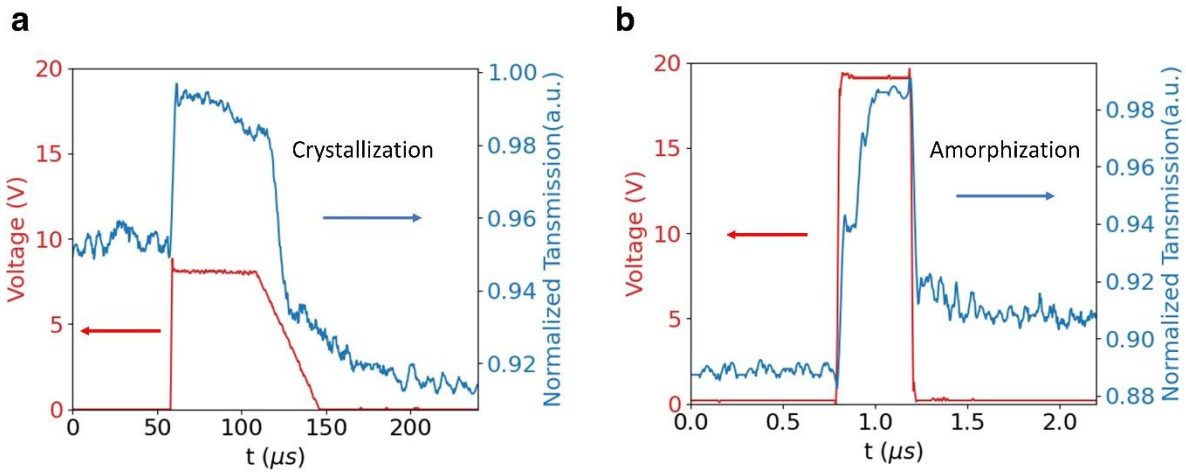

Figure 4. 11: Real-time voltage of the applied electrical pulse and the corresponding change in transmission for a crystallization and **b** amorphization.

4.12 Multilevel operation in waveguide switches and reproducibility

We show the multilevel operation of SLG-GST waveguide switch in Fig. 4.12a. Seven transmission levels can be attained by quasi-continuously tuning the RESET pulse energy from 5.71nJ to 6.49nJ. A SET pulse can be applied to return the RESET state into the initial crystalline state after the multilevel operation, as indicated by the light (initial) and saturated

(SET) orange lines. It is well-known that multilevel operation of PCMs is inherently stochastic under electrical excitations[72]. In other words, the transmission levels attained by multi-stage crystallization/amorphization is generally not deterministic because the atomic configuration after each melt-quench process will never be the same. As a result, the crystalline domains formed by the SET pulses will have different sizes, shapes, and distribution for each SET-RESET cycle. In Fig. 4.12b, we assess the reproducibility of the ten-level operation in the SLG-Sb_2Se_3 phase shifter by repeating the SET-RESET cycles for five iterations. Although the transmission levels are not deterministic, they all lie within the error bars and the mean transmission contrast across five iterations is positively correlated with the RESET pulse energy. While more transmission levels have been achieved using GST[68] by optical switching, this is usually limited by the signal-to-noise in experiment. In our measurements, the contrast between levels is around 0.5 dB which is hardly larger than the measured power fluctuation ± 0.2 dB. To relax the requirement for low noise, we either need to use larger GST volume or resonators to increase the transmission contrast. This is also why we achieved more transmission level in the Sb_2Se_3 graphene phase shifter due to the use of microrings.

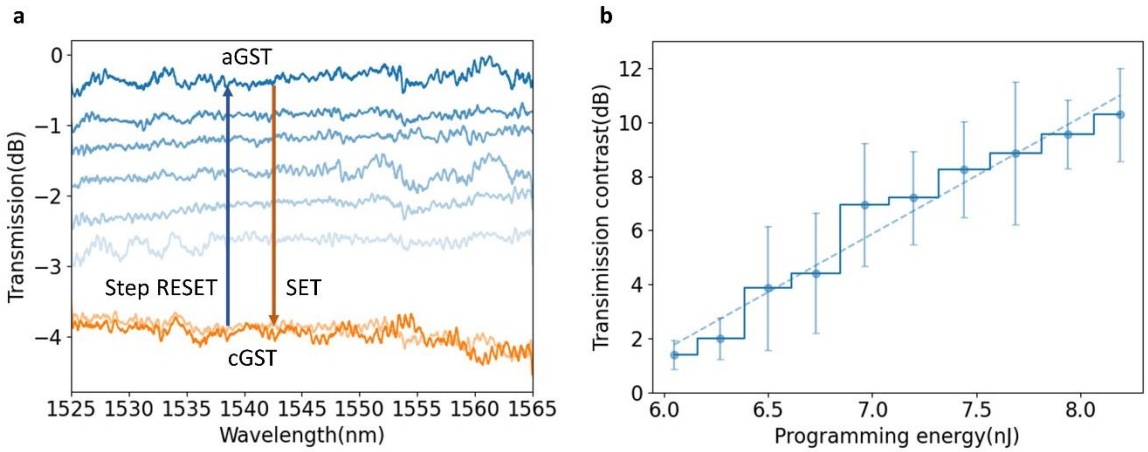

Figure 4. 12: Multilevel operation in waveguide switches and reproducibility.

a Multilevel operation of the SLG-GST waveguide switch through step amorphization. Seven distinct transmission levels are obtained by controlling the RESET pulse energy. The saturation of the blue color shows the level of amorphization. The light orange line indicates the initial crystalline state, while the saturated orange line indicates the as-switched crystalline state after the multilevel operation. The spectra are normalized with the spectrum of a bare waveguide. **b** Reproducibility of the multilevel operation evaluated by five iterations of SET and RESET cycles. Error bars indicate the standard deviation of transmission contrast for five iterations.

4.13 Experimental setup and measurement

The waveguides and microrings are characterized by a vertical fiber-coupling setup[27]. All the measurements are performed under ambient conditions while the temperature of the stage is fixed at ~26°C by a thermoelectric controller (TEC, TE Technology TC-720) to prohibit the serious thermal shift of the resonators. The input light is provided by a tunable continuous-wave laser (Santec TSL-510) and its polarization is controlled by a manual fiber polarization controller (Thorlabs FPC526) to match the fundamental quasi-TE mode of the waveguides.

A low-noise power meter (Keysight 81634B) is used to collect the static optical output from the grating couplers. The transmission spectrum measurement is performed after the fabrication of bare microrings, deposition of metal, transfer of SLG, and deposition of Sb_2Se_3 respectively to extract change in optical losses in each step. For electrical characterizations, the electrical signals are applied to the metal contacts by a pair of DC probes controlled by two probe positioners (Cascade Microtech DPP105-M-AI-S). The voltage sweep and current measurement are provided by a source meter (Keithley 2450). The generated I-V curves are used to estimate the power of the applied pulses. The SET and RESET pulses were generated from a pulse function arbitrary generator (Keysight 81150A). To reconfigure the graphene-GST photonic switch, we used a voltage pulse of 5V (2.78mA), 400ns pulse width, and 8ns rising/trialing edge to induce the amorphization. For crystallization, a voltage pulse of 3V

(1.79mA), 100μs pulse width, and 120μs trailing edge is used. To reconfigure the graphene-Sb_2Se_3 phase shifter, we used a voltage pulse of 6.8V (3.4mA), 400ns pulse width, and 8ns rising/trialing edge to induce the amorphization. For crystallization, a voltage pulse of 4 V (2.0 mA), 100 μs pulse width, and 120 μs trailing edge is used. The voltage is the actual voltage applied across the device as the impedance is matched by setting the load impedance of the function generator to the measured total resistance of the device from the I-V curve. The maximum current the graphene can withstand is typically around 3mA in our experiment. To perform the endurance test shown in Fig. 4.4e, the laser wavelength is initially parked near the resonance which gives a larger optical contrast, but later drifts away from the resonance, leading to a simultaneous increase of transmission in both states and a slightly decreased contrast. The data is filtered by a 50-point moving average to reduce fluctuation caused by thermal noises. Resonance drift of high-Q resonator due to temperature variation in the surrounding is not an uncommon issue due to the relatively strong thermo-optic effect of silicon, and integrated metallic heaters near the resonators are normally used to stabilize the temperature[40], [41]. Optimized thermal stabilization scheme will be explore in the future work but is out of the scope of current paper. To measure the transient response of the switch (Fig. 4.11), the output light from the grating couplers is amplified by an optical fiber amplifier (Amonics AEDFA-30-B-FA) and the amplified signal is detected by a 150MHz near IR fast photoreceiver (Thorlabs PDB450C) connected to an oscilloscope.

4.14 Raman spectrum of the graphene on fabricated devices

Fig. 4.13 shows the Raman spectrum measured at the graphene region on the final fabricated devices. A 514nm wavelength laser is used at 1mW power. No defect-related peaks (D, D’ or D+G) are observed, indicating that the subsequent fabrication after graphene transfer, including ALD, does not introduce structural defects into graphene. The absence of graphene

oxide peak near 1300cm^{-1} shows that the ALD Alumina growth does not induce oxidation to the graphene.

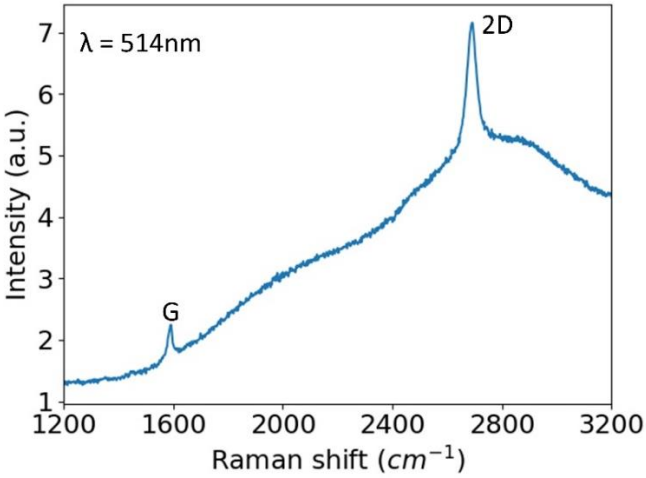

Figure 4. 13: Raman spectrum of the graphene on the fabricated devices

4.15 Summary

We have reported two examples of nonvolatile electrically switchable silicon photonic platform leveraging a monolayer graphene heater: a $Ge_2Sb_2Te_5$-based broadband waveguide switch and a Sb_2Se_3-clad phase shifter. We achieve ultra-low programming energy density (8.7 ± 1.4 aJ/nm^3) and high endurance (>1,000 cycles) at CMOS-driving voltage ($\leq$ 5V) and current ($\leq$ 2.78mA). Our results prove that graphene is not only a reliable heater that can be controlled by CMOS electronics, but also compatible with dielectric platforms, including Si_3N_4, and can potentially be used on arbitrary substrates.

Chapter 5. Non-volatile electrically programmable metasurface for free-space phase-only modulation

Free-space modulation of light has been an enabling technology behind optical communications, holography, and more recently in light detection and ranging and virtual or augmented reality. Traditional means of modulating free-space light is through spatial light modulators (SLMs) based on liquid crystals (LCs) and microelectromechanical systems (MEMS) which are bulky, require high driving voltage, suffer from phase fluctuations and crosstalk, and support only volatile operation. Recent progress in meta-optics has circumvented some of the limitations by integrating active materials with metasurfaces to realize compact and fast free-space light modulation with subwavelength pixel size. However, nonvolatile phase-only control, a highly desirable feature of free-space light tuning, is still missing. In this chapter, we demonstrate nonvolatile, electrically programmable, phase-only modulation of free-space wavefront in transmission mode based on low-loss phase change materials (PCMs) Sb_2Se_3. By coupling ultra-thin PCMs to a high-Q (Q~406) diatomic metasurface, we achieved a phase-only modulation of ~0.25π in simulation and ~0.18π in experiment. The metasurface is robust against reversible switching over 1,000 times. This work paves the way to a nonvolatile phase-only SLM.

5.1 High-Q silicon diatomic metasurfaces

Sb_2Se_3 undergoes a refractive index contrast of ~0.7 and exhibits zero loss[20] near 1550nm upon phase transition, which stipulates a ~1.1μm PCM thickness to obtain π phase shift. Although this is significantly thinner than LC used in commercial SLMs, it still poses a severe challenge in reversible switching the PCMs as PCMs need to be melt-quenched to be amorphized and such a large thickness prevents the critical cooling rate to be reached[73].

Motivated by the use of microring resonators to increase the modulation contrast in integrated photonics[9], a high-Q planar resonator can also be used to enhance the phase-modulation of free-space light by thin film PCMs, while allowing thinner device layer than Fabry-Perot cavities. Earlier works on high-Q planar resonator focused on high contrast gratings (HCGs)[74], while the more recent works studied quasi-bound-state-in-continuum (q-BIC) in periodic nanostructures with in-plane asymmetry[75], [76]. Here we combine the idea of HCGs and q-BIC by introducing an asymmetry into the periodicity of traditional HCGs, realizing a diatomic metasurface (Fig. 5.1a). Such diatomic gratings have also been proposed theoretically in several previous works[77]–[79] but have not yet been demonstrated experimentally. Fig. 5.1a shows that the symmetry of the HCG is broken by slightly displacing one of the gratings relative to the other so that the grating spacing becomes dissimilar i.e., $a_1 \neq a_2$. We denote such displacement or perturbation by $\delta = \frac{a_2 - a_1}{\Lambda}$ where Λ is the period of the diatomic gratings. The duty cycle Γ is defined as $\frac{w}{\Lambda_{HCG}}$ for HCGs and $\frac{2w}{\Lambda}$ for diatomic gratings, where w is the grating width. It can be seen that Γ is essentially identical for the two types of gratings because the period of diatomic gratings becomes doubled. The periodicity doubling causes the folding of the first Brillouin zone such that the dark modes that were originally at the edge of the Brillouin zone, which is outside the free-space light cones, get folded into the interior of the light cones, allowing for free-space excitation[77], [78]. Fig. 5.1b shows the simulated spectral response of HCGs (δ=0) and diatomic gratings (δ=0.05) upon excitation of normal incident transverse-magnetic (TM) polarized light near 1550nm wavelength (Λ=900nm and Γ=0.7). When δ=0, the dark modes are not accessible to the free-space excitation and hence no resonance is observed. While a small perturbation of δ=0.05 is enough to introduce a sharp q-BIC resonance with its signature Fano line shape. The pronounced resonance is also clearly visible in Fig. 5.2 where the q-BIC resonance represents a ~40 times electric field enhancement compared to when δ=0. By fitting the experimentally measured resonance we extract a large Q

factor of 409 for heavily N-doped 220nm silicon-on-insulator (SOI) at doping concentration~$10^{20}cm^{-3}$, as shown in inset of Fig. 5.1b. Such a high experimental Q factor is attributed to the ultra-smooth etching side wall as revealed by Fig. 5.1c, despite the additional loss from the doping. Fig. 5.1d shows the experimentally measured resonances as the period increases from 900nm to 1000nm (silicon thickness=220nm, δ=0.05 and Γ=0.7). The resonance shifts almost linearly across the telecommunication wavelength range without significant change in the Q factor – a highly-desirable characteristic of diatomic gratings[77]. In contrast, changing the period of HCGs will lead to dramatic change in the Q factor as reported previously[74]. Now it become clear why diatomic grating makes an ideal platform for demonstrating nonvolatile phase-only modulation with low-loss PCMs. First, the high Q resonance is very sensitive to loss. Cladding the metasurface with lossy materials will lead to a drastic reduction in the Q factor and hence obscuring the phase response, which is shown in the simulation in Fig. 5.6 where 20nm GST is cladded on the diatomic gratings. Secondly, 1D gratings with equal width w allows identical microheater resistance, which is essential for uniform heating of PCMs cladded on top. Using dissimilar gratings width[78] or introducing notches[80] in the gratings will also lead to high Q resonances, but each grating will have different resistance and distinct Joule heating from current injection. Lastly, the resonance can be fine-tuned to arbitrary wavelength by changing the period without degrading the Q factor, enabling operation over a large wavelength range limited only by the material bandgap.

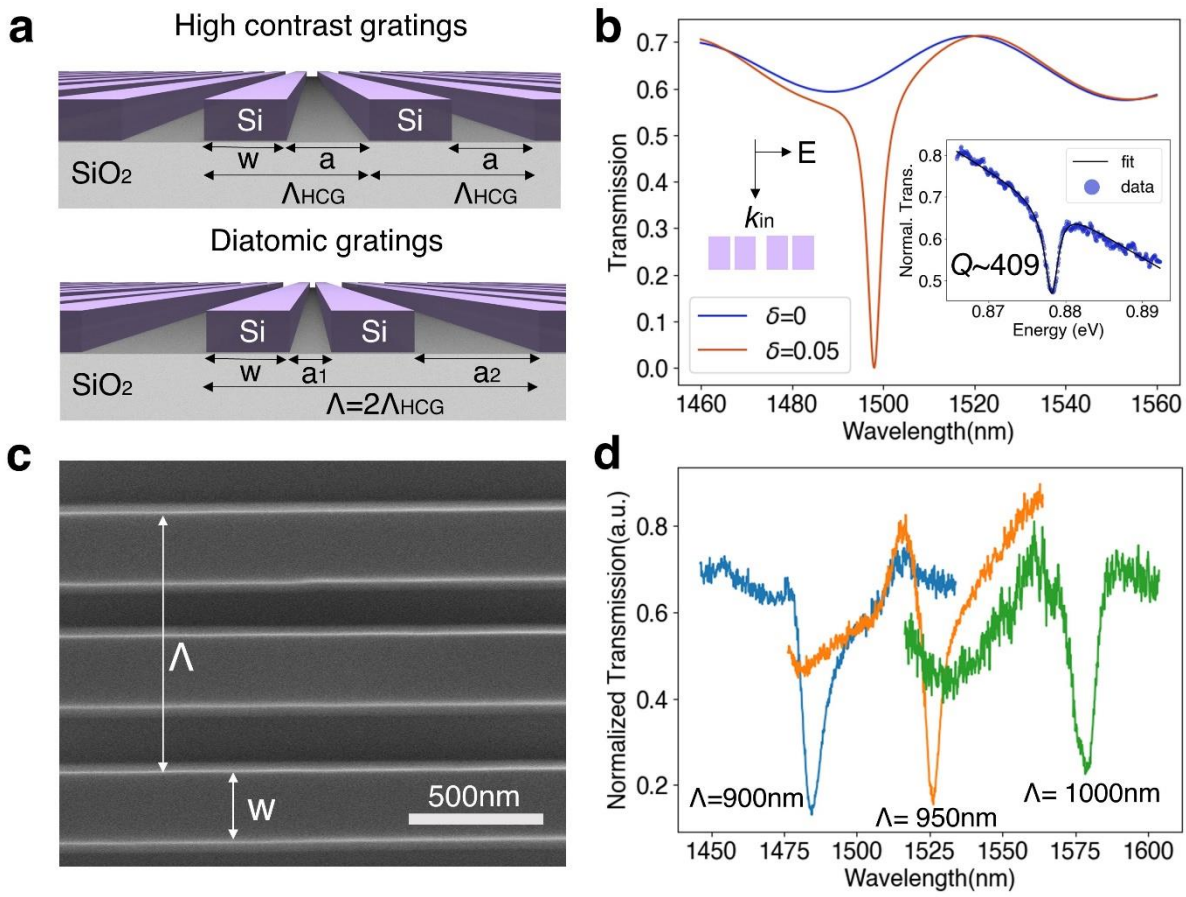

Figure 5. 1: High-Q silicon diatomic metasurfaces.

a Schematics of the high contrast gratings (top) and diatomic gratings (bottom). Λ_{HCG} and Λ are the periods of the high contrast gratings and diatomic gratings respectively. The spacing between the gratings are denoted as a, a_1, and a_2. w is the grating width. **b** Simulated transmission spectrum of the high contrast gratings (blue) and diatomic gratings (orange) under normal incident TM polarized light. Silicon thickness is 220nm, Λ=900nm and Γ=0.7. Inset: Experimental spectrum of a resonance fitted by Fano equation, Λ=950nm and Γ=0.7. **c** SEM of fabricated silicon diatomic gratings. **d** Experimental spectrum of diatomic gratings with different periods from 900nm to 1000nm, where δ=0.05 and Γ=0.7.

5.2 Electric field of the meta-gratings

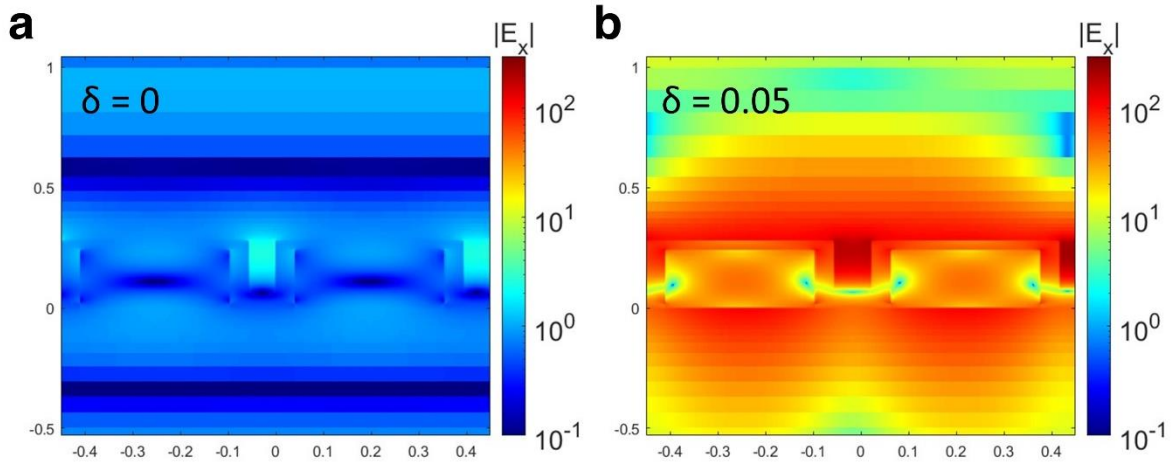

Figure 5. 2: Electric field amplitude of the high contrast gratings vs. diatomic gratings.

a Electric field amplitude of the high contrast gratings when δ is zero. **b** Electric field amplitude of the diatomic gratings when δ=0.05. Structures in **a** and **b** consist of 220nm thick silicon gratings (Λ=900nm and Γ=0.7), cladded with 20nm aSb_2Se_3 and capped with 40nm Al_2O_3. The gratings sit on 2μm thick SiO_2. The unit for x and y axes is μm.

5.3 A nonvolatile electrically reconfigurable metasurface for phase-only control

In order to dynamically control the diatomic metasurface, we dope the SOI into microheaters[28], [81] that is used to switch the Sb_2Se_3 cladded on top (Fig. 5.3a). The Phosphorus doped (doping concentration~$10^{20}cm^{-3}$) silicon is then etched into diatomic gratings before cladded with 20nm Sb_2Se_3 via sputtering, followed by 40nm atomic-layer-deposited (ALD) Al_2O_3 encapsulation to prevent oxidation and PCM dewetting during switching (See section 5.4 for details on device fabrication). Ohmic contacts are then formed by Ti/Au electrodes. The cross-section of the metasurface is shown in Fig. 5.3c. Current is injected into the highly doped silicon gratings via electrical pulses that causes joule heating, which in turn switches the PCMs. A two-objective transmission setup (see section 5.8 for

details on measurement setup) is built to probe the reversible switching of Sb_2Se_3-loaded diatomic metasurface. The fabricated chip is wire bonded to a customized printed circuit board (PCB) (labelled PCB1 in Fig. 5.3b) connected to a second customized PCB carrying a microcontroller (labelled PCB2 in Fig. 5.3b). PCB2 is then connected to an arbitrary function generator (AFG) that generates pulses. The microcontroller on PCB2 can be programmed by a computer to individually address metasurface pixels fabricated on the same chip (see Methods for details on the electrical control). Fig. 5.3d shows the optical micrograph of a 30μm aperture metasurface pixel on a chip that has been wire bonded to the PCB.

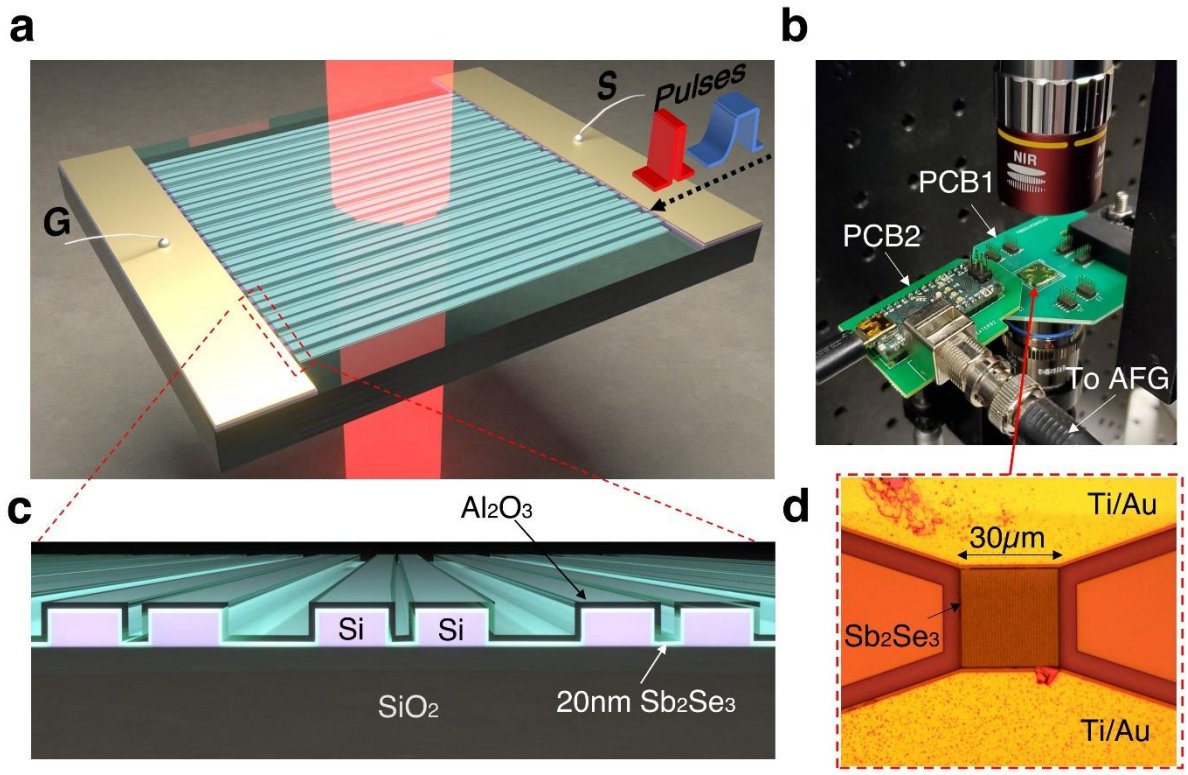

Figure 5. 3: A nonvolatile electrically reconfigurable metasurface based on Sb_2Se_3.

a Schematic of the transmissive tunable diatomic metasurface based on Sb_2Se_3. S (G), signal (ground) electrode. **b** The optical setup for probing the metasurface in transmission along with the devices under test wire bonded to a customized PCB. AFG is arbitrary function generator. **c** The schematic of the

tunable metasurface cross section. **d** Optical micrograph of a single metasurface pixel on the chip under test.

Reversible tuning of the diatomic resonance is shown in Fig. 5.4a (simulation) and 5.4b (experiment). The spectra of three consecutive switching cycles are plotted in Fig. 5.4b and the shaded regions indicate standard deviations between the cycles. The small standard deviation reveals excellent cycle to cycle reproducibility. The experimentally extracted spectral shift ($\Delta\lambda{\sim}1.2nm$) matches very well with the simulated shift ($\Delta\lambda{\sim}1.3nm$). Fig. 5.4c shows the phase shift ($\Delta\phi$) and transmission contrast ($\Delta T\%$) between the two optical states near the 1518nm resonance. A good match between the simulation and the experiment can be clearly seen. We extract a maximum phase shift of ~0.18π (~0.25π) near the resonance wavelength from experiment (simulation) with less than 3% measured change in transmission. See Section 5.8 for details on the measurement of spectrum and phase shift. To further show that this is indeed a phase-only modulation, we fit the Fano line shape to the resonances of aSb_2Se_3 and cSb_2Se_3 averaged over five consecutive cycles (Fig. 5.5). The extracted Q factor only decreases from 312 to 271 upon crystallization, representing only 13% reduction, which shows that minimal loss is introduced by the phase transition. In contrast, the high Q resonance is completely suppressed by the same thickness of GST cladded on the metasurface due to its high optical loss (Fig. 5.6). Temporal trace measurements (Fig. 5.7a) also confirm that the change is indeed non-volatile and hence caused by the Sb_2Se_3. Finally, we show that the tunable metasurface is robust against switching over 1,000 times without degradation in the contrast, as shown in Fig. 5.4d. The tunable laser is parked near the resonance to detect a measurable change in the transmission (See section 5.8). Optical micrographs taken before and after the cyclability test indicate no ablation is caused by the switching across the entire 30×30μm^2 metasurface (Fig. 5.7b).

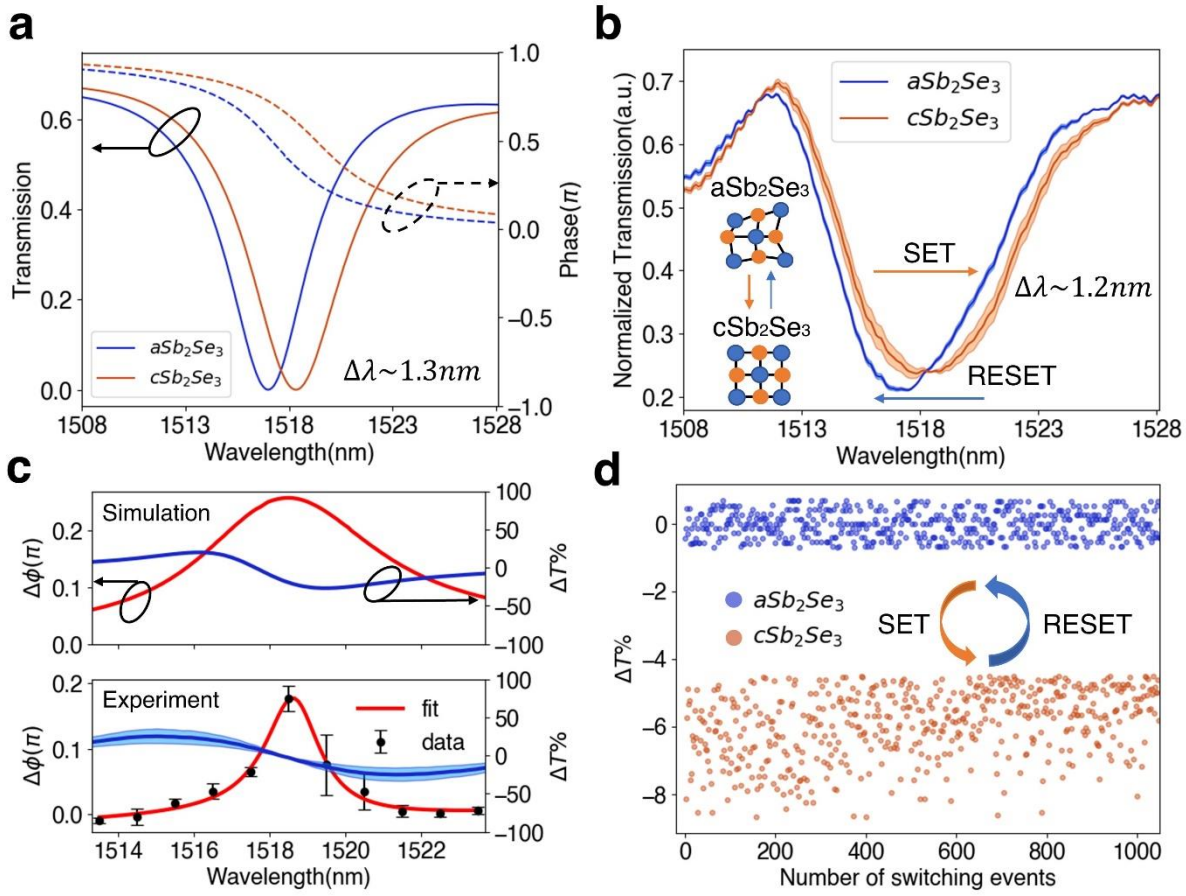

Figure 5. 4: Reversible switching of the diatomic metasurface and nonvolatile phase-only modulation.

a Simulated spectral and phase shift caused by 20nm Sb_2Se_3. Δλ is the wavelength shift of the resonance dip. The diatomic metasurface is designed to be Λ=900nm, Γ=0.7, and δ=0.05. a(c)Sb_2Se_3, amorphous(crystalline) Sb_2Se_3. **b** Measured reversible switching of the diatomic resonance. The switching conditions are 3.6V, 50μs pulse width, 30μs trailing edge for SET and 11.6V, 1μs pulse width, 8ns trailing edge for RESET. Three consecutive cycles are plotted where the shaded area indicates the standard deviation between the cycles and the solid line indicate the average. The spectrum is normalized with the spectrum of bare SiO_2 on silicon. **c** Phase shift (Δϕ, red) and transmission contrast (ΔT%, blue) between the two optical states extracted from simulation (top) and experiment (bottom). The phase is measured at 11 different wavelengths with 1nm spacing and averaged over three switching cycles. The standard deviation over the cycles is shown by the error bars. **d** Cyclability of the tunable metasurface for 1,000 switching events. The switching conditions are 3.6V, 50μs pulse width, 30μs trailing edge for SET and 11.6V, 600ns pulse width, 8ns trailing edge

for RESET. Each pulse is temporally separated by 2s to ensure long thermal relaxation. The data is filtered by a two-point moving average to reduce fluctuation caused by thermal and mechanical noises.

5.4 Fabrication of the programmable metasurface

The reconfigurable diatomic metasurface is fabricated on a 220-nm thick silicon layer on top of a 3-μm-thick buried oxide layer (SOITECH) with back-side-polished silicon. The blanket SOI wafer is first implanted by phosphorus ions with a dosage of 2×10^{15} cm^{-2} and ion energy of 40 keV at a tilt angle of 7°. Subsequently, the wafer is annealed at 950 °C for 30 min to activate the dopants. The metasurface pattern is defined by a JEOLJBX-6300FS 100kV electron-beam lithography (EBL) system using positive tone ZEP-520A resist. 220 nm fully etched gratings are made by an inductively coupled plasma reactive ion etching (ICP-RIE) process in Florine-based gases. Before metallization, the surface native oxide was removed by immersing the chips in 10:1 buffered oxide etchant (BOE) for 15 s to ensure Ohmic contact. A second EBL exposure using positive tone poly(methyl methacrylate) (PMMA) resist is subsequently carried out to create windows for the Ti/Au deposition. After development, 5nm Ti followed by 150 nm Au was electron beam evaporated onto the chip. The lift-off of Ti/Au was completed again by immersing the chip in methylene chloride. The third EBL step is used to expose the PMMA resist before depositing Sb_2Se_3 via magnetron sputtering. The Sb_2Se_3 is sputtered using a magnetron sputtering system at 30 W RF power under a deposition pressure of 4 mTorr and Ar flow of 30 sccm. The deposition rate for Sb_2Se_3 is ~1 nm/min. Additionally, the samples are capped with 10 nm of SiO_2 sputtered in situ (150 W RF power, 4 mTorr pressure, and Ar flow of 30 sccm), to prevent oxidation during sample shipping. The atomic ratio of Sb_2Se_3 after deposition is confirmed using XPS to be Sb:Se ≈ 44:56 which is close to the sputtering target stoichiometry of Sb:Se ≈40:60. Immediately after lifting off the PCM in methylene chloride, a 40nm ALD Al_2O_3 is

grown on the chip to protect the PCM from oxidation and reflowing during switching. To allow good adhesion between the wedge bonds and the metal pads, the 5th EBL step is used to open windows in PMMA resist at the wire bonding regions for Al_2O_3 etching. The Al_2O_3 on top of the contacts is etched away using ICP-RIE etching in Chlorine-based gases. Then the PCMs are initialized into the fully crystalline state by rapid thermal annealing (RTA) at 200°C for 10 min under N_2 atmosphere before measurements. Finally, the chip is wire bonded onto the custom-made PCBs using a wire bonder (Westbond) via gold ball-wedge bonds.

5.5 *Q* factor of the diatomic resonance

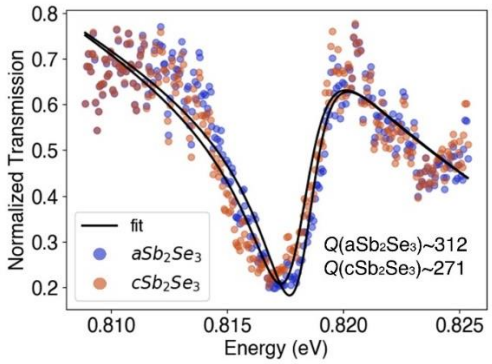

Figure 5. 5: Fitting of the diatomic resonance by Fano equations when Sb_2Se_3 is in amorphous (blue) and crystalline (red) states.

To extract the Q factor, the diatomic resonance is fitted by a Fano line shape using the equation $T = | g_1 + jg_2 + \frac{b}{E-E_0+j\gamma} |^2$, where g_1, g_2, and b are constant real numbers. E is the photon energy and E_0 is the central resonance energy. 2γ is the line width of the resonance. So, the Q factor is calculated to be $\frac{E_0}{2\gamma}$.

5.6 $Ge_2Sb_2Te_5$ on diatomic gratings

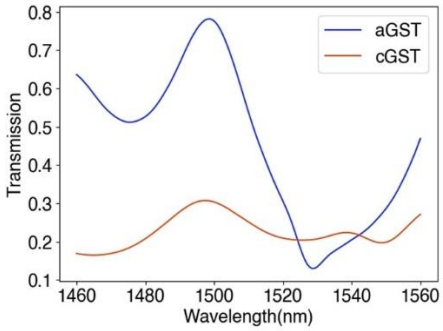

Figure 5. 6: Spectrum of the same diatomic gratings cladded with 20nm GST.

5.7 Temporal response of the non-volatile switching

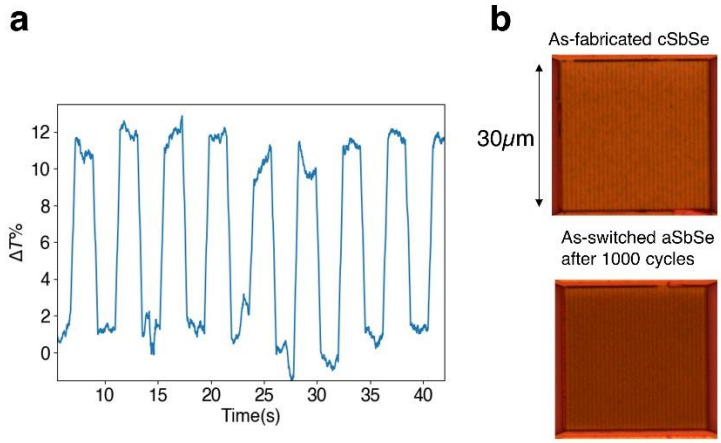

Figure 5. 7: Temporal response of switching the metasurface.

a Switching the metasurface with 2s interval without excitation, indicating non-volatile tuning. **b** Optical micrographs of the metasurface pixel before and after the endurance test. No damage is observed.

5.8 Optical setup and measurement

The metasurface is characterized by a custom-build two-objective transmission setup (see Fig. 5.3b and Fig. 5.8a). A collimated broadband laser (Fianium) is linearly polarized and focused onto the metasurface at normal incidence by a 10× near IR objective (Mitutoyo, 0.26 numerical aperture) and collected by a 50× near IR objective (Olympus, 0.65 numerical

aperture). The beam splitter (Transmission: Reflection~85:15 in near IR) splits the light into two paths: one path (~85%) goes to the IR spectrometer (Princeton Instrument) for characterizing the optical spectrum; the other path (~15%) goes to the IR camera (NIT SenS 320) for imaging the metasurface. Fig. 5.8b shows the modified setup for characterizing the cyclability of the tunable mesurface and beam splitting. A tunable continuous-wave laser (Santec TSL-510) is used here as the source to park the laser wavelength near the 1518nm resonance while the real-time transmission is monitored by a low-noise power meter (Keysight 81634B). Beam splitting effect is recorded on the IR camera via the additional lens that focuses on the BFP of the objective.

To measure the phase shift caused by the switching, we built a Mach-Zehnder interferometer (Fig. 5.8c) and switched the pixel in-situ. The interference fringes between the signal beam through the metasurface and the reference beam are taken by the IR camera. The images are captured at 11 different wavelengths from 1513nm to 1523nm for the two optical states, averaged over 20 frames. The phase of each optical state is calculated by first applying a high pass filter on the image in the Fourier domain, and then take the argument of the filtered image in the real space. The phase shift is the difference between the extracted phase in crystalline state and amorphous state.

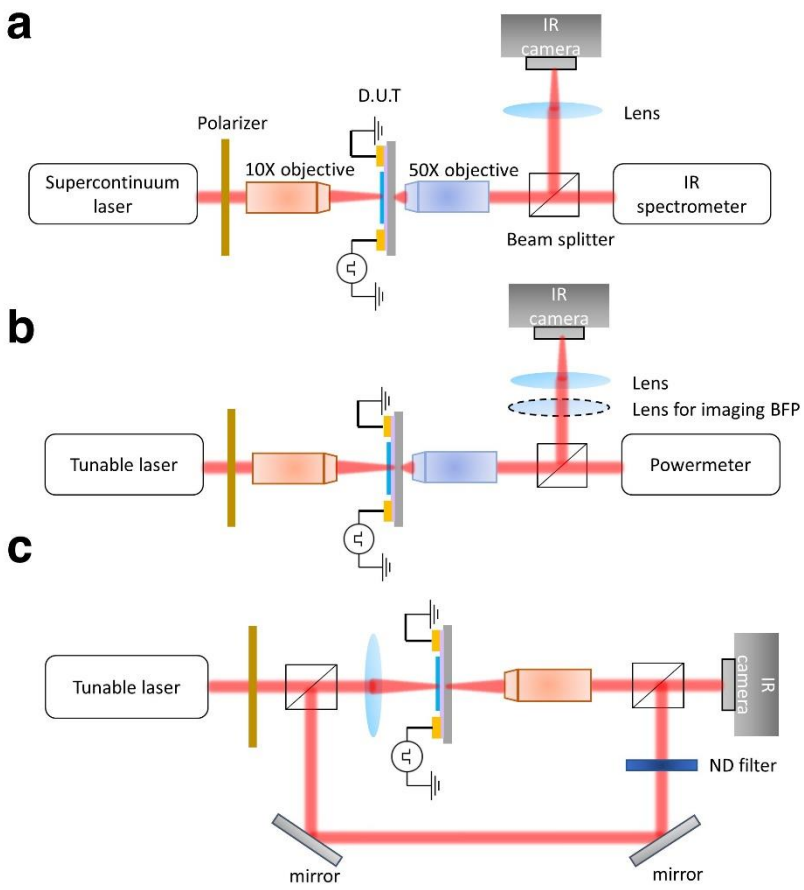

Figure 5. 8: Schematic of the experimental setup.

a Optical setup for measuring switching of metasurface spectrum. **b** Optical setup for characterizing the device endurance and imaging the far field of the gratings. **c** Optical setup for measuring the optical phase shift caused by the metasurface switching.

5.9 Electrical control for individual addressing

Each metasurface pixel on the chip is connected to a metal pad that is wire bonded to a pin on the carrier PCB or PCB1. A hole (0.8cm in diameter) is opened at the center of PCB1 to allow direct light transmission through the PCB. In order to individually control the pixels, a second customized PCB (PCB2) carrying a microcontroller (Arduino Nano) is inserted into the predefined pins on PCB1. Most commercial microcontrollers normally supply low voltage (≤5V) and slow speed (tens of megahertz), whereas high amplitude (>10V) and short (nanosecond falling edge) pulses are required to amorphized the PCMs. Hence the

microcontroller cannot be directly used to switch PCMs, instead an external function generator is connected to the PCB2 as a source of excitation. The microcontroller can be programmed to turn on/off 17 MOSFETs connected in series with the on-chip microheaters. By switching the MOSFET, the voltage drop across the microheater can be controlled independently when an electrical pulse is applied. The resistance of the microheaters is measured using a source meter (Keithley 2450). A 30μm^2 large metasurface pixel typically has resistance of ~70Ω at 1mV DC bias. The SET and RESET pulses were generated from an arbitrary function generator (Keysight 81150A). To reconfigure the metasurface, we used a voltage pulse of 11.6V (~166mA), 1μs pulse width, and 8ns rising/trialing edge to induce the amorphization. For crystallization, a voltage pulse of 3.6V (~51mA), 50μs pulse width, and 30μs trailing edge is used.

Chapter 6. Opportunities and Challenges

To summarize, we have attempted to tackle the challenges that we identified at the beginning of the dissertation in order to bring the PCM-based photonic technology a step closer to commercially viable and scalable products. In particular, we have shown that, compared to the traditional GST-based platforms, low-loss PCMs such as Sb_2S_3 and Sb_2Se_3 substantially reduce the loss of photonic systems, making large-scale PICs possible. Based on these low-loss PCMs, we demonstrated an ultra-compact directional coupler switch - an essential building block of programmable PICs. Previously, electrically controlling PCMs consumed a large amount of power (tens of mW). Leveraging monolayer graphene heaters, we solved this long-standing challenge in the community by showing low switching energy density approaching the fundamental limit. Finally, beyond PICs, we demonstrated phase-only control of free-space wavefront using low-loss PCMs, which can potentially enable non-volatile SLMs.

Despite progress, several outstanding challenges remain in the field. For example, how to extend the operation range to the visible wavelengths where the material loss becomes critical? How to increase the endurance of the PCM-based devices for practical use, ideally > 10^9 cycles? How to achieve a deterministic multilevel operation? How to attain 2π phase shift using PCMs? How to control a large 2D array of phase-change pixels/switches individually? How to fabricate PCM-based photonic devices via foundry processes? In this chapter, we aim to answer these questions by briefly discussing the advances in the field, the limitations, followed by potential solutions to address these limitations. In Table 6.1 we compare the key performance metrics of the state-of-the-art in PCM-based programmable photonics.

Table 6. 1: Performance comparison of the recent work in the field.

	PCMs	Control	μ-heaters	λ (nm)	Endurance	Δφ (π)	Number of levels
Fang, Z. et al. (2021)[9]	Sb_2S_3	Electrical	ITO	1550 and 740	1	0.17	2
Zhang, Y. et al. (2021)**[82]**	GSST	Electrical	Pt	1550	40	-	10
Wang, Y. et al. (2021)**[83]**	GST	Electrical	Ag	755	100	-	2
Delaney, M. et al. (2021)[12]	Sb_2Se_3	Optical	-	1550	600	10	40
Rios, C., et al. (2022)**[84]**	Sb_2Se_3	Electrical	Doped Si	1550	125	0.5	9
Fang, Z. et al. (2022)**[10]**	Sb_2Se_3	Electrical	Graphene	1550	1000	0.014	14
Moitra, P., et al. (2022)**[85]**	Sb_2S_3	Optical	-	700	2	2	2
Chen, R. et al. (2023)**[49]**	Sb_2S_3	Electrical	Si PIN	1310	800	1	32
Zhang, C. et al. (2023)**[86]**	GST	Electrical	ITO	1550	3	0.4	64

6.1 Extending the operation range to the visible

In the early days, PCMs were widely used in rewritable compact disks to store data in a non-volatile manner. They were typically designed to be highly absorptive in the visible wavelength so that they can be easily switched by laser pulses. Later they found applications in electronic memory, where data is stored in the high and low resistance of the memory cell, rendering the optical absorption of the materials entirely irrelevant. It is only recently, with the advent of PCM-integrated photonics[7,8] has the loss become critical. The proximity of the PCMs to the optical mode in a waveguide can lead to a significant loss even for a very short segment of PCM, e.g., crystalline GST typically gives >1 dB/μm insertion loss on a waveguide. Apart from PCM, we also need to pay attention to the loss incurred by the microheaters needed to actuate the phase transition electrically. Fig. 1 shows the transparency

windows of six different PCMs (in their amorphous state) and microheaters, along with the potential applications in different wavelength ranges. These six PCMs represent the most widely reported PCMs in the field of photonics due to their lower optical losses and reversible switching over many cycles. To simplify the discussion, we only plot the transparency window in the lower loss (or wider bandgap) amorphous state because the PCMs need to be transparent in at least one state to be useful. PCMs that are transparent in the amorphous state but lossy in the crystalline state (e.g., GeTe, GST, $Ge_2Sb_2Se_4Te_1$ (GSST), and $Ge_2Sb_2Se_5$ (GSSe) in the near IR) can be used for amplitude modulation such as photonic memory[50]. PCMs transparent in both amorphous and crystalline states (e.g., Sb_2Se_3 and Sb_2S_3 in the near IR) are ideal for phase-only modulation[10], [49]. It can be seen from Fig. 1 that as new PCMs are discovered, there is a general trend of increasing the bandgap of the PCMs to achieve lower losses. The bandgap of the GST can be widened by gradually substituting Tellurium with Selenium, creating GSST and GSSe[11]. Removing the Germanium further widens the bandgap, yielding Sb_2Se_3 which is transparent in both amorphous and crystalline states in the near infrared (IR) wavelengths. Finally, the bandgap can be further increased by replacing the Selenium with the more electron affinitive Sulfur, which leads to Sb_2S_3 – the only PCM that has a transparency window in the visible spectrum. Looking at our material toolbox, we now have a wide range of options for a PCM that can work in the near to mid-IR regime. Meanwhile, doped silicon also makes a reliable, scalable, and transparent microheater for the electrical control of PCMs in this range[20]. Indeed, proof-of-concept PCM-integrated photonic devices have been demonstrated for relevant applications in this regime, including optical computing and optical interconnects for data centers. However, the choices become scarce when the wavelength extends to the visible ($\lambda \sim 400 - 700nm$), where Sb_2S_3 is the only candidate, whose transparency window only partially covers the visible range (~600-700 nm). A transparent PCM in the entire visible

range can unlock several emerging applications from augmented/virtual reality (AR/VR) display to quantum photonics. For example, AR displays require selected pixels to be dimmed so that the displayed image is not overpowered by the ambient light [21]. Such "local dimming" functionality requires reversible sub-*ms* switching between the bistable transparent and opaque states. A PCM transparent (absorptive) in the amorphous (crystalline) state in the visible range will be ideal for achieving unpolarized dimming, compared to the current polarized dimming based on liquid crystals which blocks >50% of the ambient light in the transparent state. Secondly, photonic quantum information technologies require single photons to be routed in a PIC with low loss and energy consumption. Currently, the quantum PIC is generally tuned by thermo-optic phase shifters which are prohibitive in terms of power consumption. A PCM transparent in both states in the visible can provide non-volatile and energy-efficient routing of solid-state single photon emitters (generally ranging from $\sim 400 - 900 nm$) [9]. To push the PCMs' bandgap wider, materials with stronger covalent bond formers, such as Oxygen, may have to replace Sulfur to create semiconductor or metal oxides that have bandgap in the ultra-violet range[22]. It is also worth investigating when the phase-change properties of the material cease to exist as the material bandgap keeps increasing, which can be modelled using density functional theory and molecular dynamics simulations. In terms of electrical control, both graphene and Indium Tin Oxide (ITO) are transparent microheaters in this range (though ITO has lower absorption than graphene).

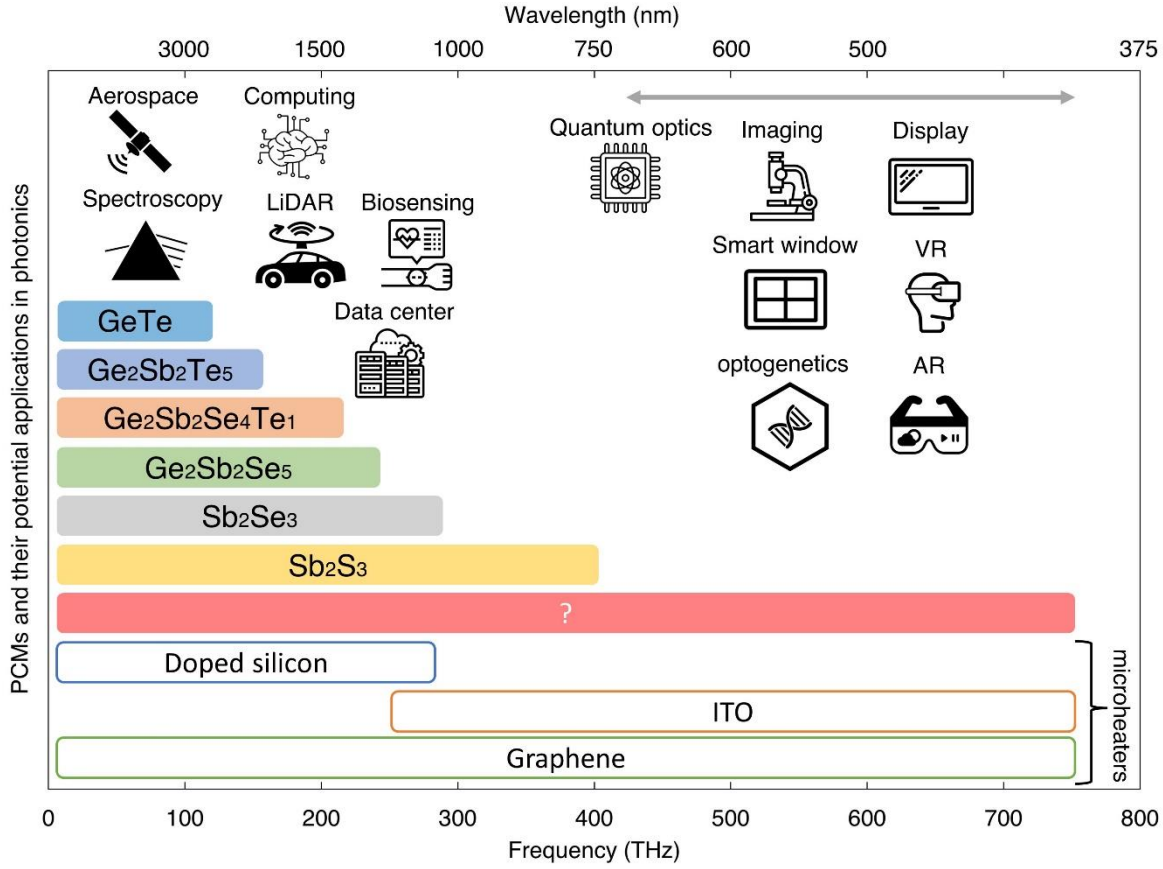

Figure 6. 1: Transparency windows of PCMs and microheaters from visible to mid-IR wavelengths and their potential applications in photonics.

6.2 Increasing the device endurance

Commercialization of PCM-based photonic devices depends heavily on their endurance. Previous commercialized PCM technologies, such as electronic memory, exhibit a typical endurance of > 1 billion cycles[23]. It seems natural that PCM-based photonic devices should also target an endurance of at least 1 billion cycles. In practice, this is a challenging proposition for photonic devices because, depending on the applications, the switching volume of the PCMs is around five to six orders of magnitude larger than in electronic memory (~100 μm^2 vs ~100 nm^2, assuming the same thickness). Such a large switching volume renders many failure mechanisms, which play relatively minor roles in electronic memory, dominant. These include surface oxidation, drastic volume change, elemental

segregation, and dewetting in the molten state[24]. For these reasons, the best record in electrical switching so far has been ~5,000 cycles in PIC[25] and 1,000 cycles in free space [63]. Hence, instead of focusing solely on the formidable challenge of increasing the cyclability from 10^3 to 10^9, we ask: how many cycles do we actually need for relevant applications? First, consider the scenario where a PCM-based non-volatile phase shifter is used to correct the phase error in a Mach-Zehnder interferometer (MZI) or trim a microring's resonance wavelength[49]. Once these calibrations are completed after the fabrication, which can be accomplished within a few switching events, any further adjustments will hardly be required since an on-chip laser normally has a fixed emitting wavelength. In this case, an endurance of 1,000 cycles will be more than enough, which has already been reported[10], [47]. Another relevant application is in-memory optical computing, where PCMs have shown promising results for expressing weights[8]. If used purely for inference, a low endurance may be sufficient. However, for general purpose computing, the weights need to be constantly updated, and very high endurance comparable to the phase-change electronic memory will likely to be necessary for any practical use.

In addition to PICs, PCMs can also be used in tunable meta-optics[6]. For example, a non-volatile spatial light modulator (SLM) will be highly desirable in the scenario where a stable phase mask is required (see Chapter 5). Liquid-crystal-based SLMs commonly suffer from phase jitter and pixel crosstalk, which can be circumvented by controlling the optical phase with PCMs, as no bias is required to maintain the optical phase distribution. Consider static usage, such as laser beam shaping, where the phase mask does not constantly change and assume ~10 reconfigurations per day, an endurance of 10^4 cycles will lead to a lifetime of almost 3 years. However, certain applications of SLMs, such as displays, require constant refreshing of the pixels (> 60 Hz), so high endurance (>10^{10}) may be needed to operate up to 5 years. Similarly, recent works have demonstrated non-volatile beam steering using PCMs in

phase-gradient metasurfaces[82], with potential application in ranging. Ranging requires constant scanning of the laser beam; hence very high endurance (>10^9) will be necessary. Finally, we would like to emphasize that traditional switching metrics, like switching speed, may not be appropriate for evaluating PCM-based photonic devices. These metrics are relevant only when a device is constantly being turned on and off, for example a modulator. In such cases, a switch being turned on and off in nano-second time scale, will last only for 10 seconds, even with an endurance of 10^{10}. Hence, improving switching speed has little or no significance in practical applications.

There are several potential strategies to reach endurance greater than a billion cycles. Two important lessons we can learn from the electronic memory to improve the endurance is to reduce switching volume and use backup devices. Instead of switching a large area of PCMs (>100μm^2), we can pattern the PCMs into discrete subwavelength patches to minimize dewetting and stresses from the drastic volume change. Secondly, backup switches can be used to improve the overall endurance of a group of switches. Once a switch in the group failed, it will be automatically connected to a working one. Such scheme is particularly attractive for PICs but has issues in free space because a wavefront will always interact with all the pixels, including the failed ones.

6.3 Deterministic multilevel operation

The crystallization of PCMs is based on nucleation and growth, which are intrinsically stochastic processes[72]. Partial phase transition will inevitably lead to variation in the optical state as the volume and location of the switched material are slightly different each time. There has been tremendous progress in pushing the number of attainable levels in PCM-based photonics, reaching up to 5-bit operation via optical switching[68] and, more recently, in electrical switching[49] using low-loss PCMs Sb_2S_3, see Table 6.1.

Conventionally, different amplitudes or pulse durations are used to tune the degree of partial phase transition to achieve multi-levels. Recently, it was shown that multilevel operation could be obtained in Sb_2S_3 by exciting it with multiple electrical pulses with the same duration and amplitude[49], leading to an additional degree of freedom in fine tuning the optical states. In this way, the optical states of the devices can be controlled simply by the number of excitation pulses without the need to change the pulse shape. Despite the progress in increasing the optical levels, there has not been an effective solution for the optical state variation caused by the non-deterministic phase transition. For many applications, such as SLMs and optical computing, precise control of the optical levels is necessary. One potential solution is to use many PCM cells and exploit the complete phase transition of each cell. Complete phase transition is found to be highly deterministic as the entire volume of materials is switched. For example, one requires N-1 discrete cells of PCMs on a waveguide to achieve N number of transmission levels. The contrast between the levels can be controlled by the size of the PCM cells. However, such a scheme only works for integrated photonics where light is tightly confined in the waveguide, and the optical mode has a limited spatial extent. In addition, N levels will also require N-1 control signals, leading to complicated electrical routing as N becomes large. In the free space, spatial light modulation requires the light to interact with multiple pixels simultaneously, which collectively generates a phase mask. The light interacting with any individual pixel will only experience a binary switching of phase or amplitude if there is only a complete phase transition. One solution is to stack multiple layers of PCMs along the optical axis, where each layer is individually controlled by microheaters. However, this method will require complicated electrical wiring and suffer from significant optical losses as light passes through layers of PCMs and microheaters. A simple solution for the multilevel control of a 2D array of phase-change pixels will be a promising future research direction.

6.4 2π phase control

In integrated photonics, a maximum of π phase shift is generally enough for modulating MZIs or microrings. Thanks to the large effective index change of PCM-silicon hybrid waveguides, the typical L_π can be as short as a few tens of microns[49], [84]. In free space, however, full 2π phase control is necessary for spatial light modulation. In liquid-crystal-based SLMs, 2π phase shift is achieved by using a very thick (>1μm) LC layer. Switching the same thickness of PCM turns out to be extremely difficult because as PCM becomes thicker, the cooling during amorphization becomes slower, and at some point, the material can no longer hit the critical cooling rate for amorphization. For example, GST is a fast PCM that typically requires a cooling rate of ~1 K/ns to reach the amorphous state and reversible switching is difficult for thickness >30 nm. Instead of using fast PCMs, PCMs with slow phase-change kinetics can be used, such as GSST, Sb_2S_3, and Sb_2Se_3, which also happen to have lower losses. For example, 250-nm-thick GSST can be switched by long pulses of 5 μs (amorphization) and 200 ms (crystallization) to yield large modulation, but at the cost of limited cyclability (40 cycles)[82]. Another approach to enhance the phase shift is via optical resonators such as metasurfaces. Recent work shows that by patterning Sb_2S_3 into a Huygen's metasurface, near 2π phase shift can be obtained in the visible range through the spectral overlap of the electric dipole and magnetic dipole resonances[85]. However, the thick material (160 nm) causes difficulty in reversible switching, and only two cycles have been demonstrated, see Table 1. Using resonant metasurfaces also limits the bandwidth that 2π phase shift is maintained. Hence, although there is no perfect solution yet to achieve 2π phase shift, high endurance, and broadband at the same time, the combination of optical resonance and the slow PCMs could potentially provide a solution towards a larger phase modulation.

6.5 Controlling a 2D array of pixels

Applications that we have envisioned above, from optical computing to SLMs, all require controlling a 2D array of pixels or switches. Although we can use lasers to easily write a 2D array of PCM pixels without any control circuits, electrical switching is essential to realize a fully integrated and scalable platform, which has not been demonstrated in PCM-based photonic devices so far. Thanks to the non-volatile behavior of PCMs, a 2D crossbar array and time multiplexing can be used to address multiple pixels sequentially by one common source. However, writing pixels one by one will be extremely time-consuming if many pixels need to be addressed. We can simultaneously address multiple pixels using 2T1C (two-transistors-one-capacitor) circuit, commonly adopted in CMOS drivers for controlling the pixels in organic light emitting diode panels, see Fig. 6.2. The row selecting bias V_{sel} will switch on transistor T_1, allowing the V_{sig} to be dropped on the gate of transistor T_2 at V_{G2}. The storage capacitor C_s will be charged until V_{G2} equals V_{sig}. We can control how much current is drawn by the microheater for switching PCMs by tuning the V_{sig}; hence, a multilevel operation can be realized at the same pulse voltage V_{DD}. This way, multiple pixels can be switched simultaneously, and the level depends on the applied V_{sig} to each pixel.

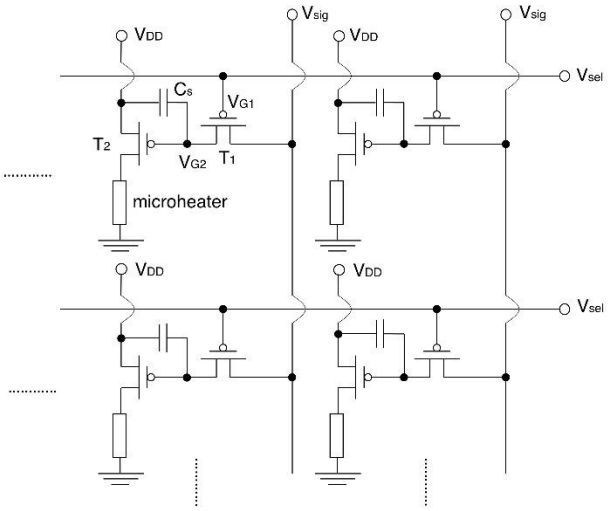

Figure 6. 2: 2T1C circuit to simultaneously address a 2D array of phase-change photonic switches or pixels with a common source of V_{DD}. Four pixels are shown here for simplicity.

6.6 Fabrication via foundry processes

So far, all PCMs-based photonic devices have only been fabricated either completely or partially in the university cleanroom. One recent work has reported the fabrication of silicon waveguides in a foundry, but the deposition, patterning, and encapsulation of PCMs were performed in a back-end-of-the-line process[84]. Foundry fabrication is a crucial step towards the scalability and the ultimate commercialization of PCM-based photonic technology. Large companies like Intel and IBM already have products on the market based on phase-change electronic memory with GST in their fabrication line. One would assume bringing PCMs into silicon photonics foundry would be straightforward. However, foundry compatibility proves to be a more challenging task. In fact, silicon photonics fabrication has very different processes from the memory cell, including material deposition, etching, metallization, and oxide cladding. The potential risks of introducing PCMs into a photonics foundry process, such as contamination, is extremely difficult to evaluate. Working with well-known PCMs such as GST may have an edge on this because the toxicity of the materials is very well-studied, compared to new PCMs such as Sb_2Se_3, where Selenium is highly volatile and toxic. One potential solution will be dedicating a line solely to PCM-based photonics and

demonstrating an application using PCMs that can have a large market will help to draw interest from big semiconductor companies to invest. Electronic memory has set an excellent example for the commercialization of PCMs, which we can all learn from. We believe as silicon photonics becomes more prevalent, more and more materials will become foundry compatible, because it is unlikely that silicon will be a universal solution for all PIC functionalities. For example, III-V semiconductors which were traditionally considered not CMOS compatible have gradually become foundry compatible, motivated by the demand for integrated light sources in silicon. III-V materials require high temperature epitaxial growth followed by transfer to silicon via wafer bonding. It is unlikely that PCMs will be more challenging than III-Vs to integrate with the current foundry process since PCMs can be easily deposited via room-temperature sputtering or evaporation. What motivates the foundries to develop processes for new materials is a large demand from the industries, from which the foundries make the most profit. We believe a near-term solution for scaling PCMs technology is through a back-end-of-the-line process, where foundry fabricated PICs are post-processed in research grade cleanroom for PCMs deposition. This will show that PCM-based photonics is indeed scalable and draw potential interest from the industry in commercializing such technologies.

6.7 Summary

To summarize, we have discussed important open questions in the field of PCM-based programmable photonics. We proposed potential solutions and future research directions. We believe that the visible range hosts enormous opportunities for PCMs with many unexplored applications, from quantum optics to AR/VR. A wide-bandgap PCM that is transparent across the entire visible spectrum will be a game changer. Secondly, we argued that the device endurance should be evaluated based on applications, and similarly the potential applications should be guided by the available endurance. For certain applications, such as trimming, the

state-of-the-art endurance (~10^3) has already met the need, whereas for other applications, such as computing and wavefront manipulation, very high endurance (>10^9) is necessary. Next, we discussed the factors that are currently limiting the precision of optical levels and maximum phase shift and proposed strategies to address these issues. In addition, the ability to control a large 2D array of phase-change pixels or switches will be a crucial step toward scalability and a commercialized prototype. Finally, we addressed another essential building block for scalability: the foundry compatibility of phase-change photonic devices. A dedicated fab line for the PCMs-based photonic devices will be a crucial step before commercialization. Still, before getting there, a scalable prototype must be demonstrated to draw market interest from investors and large semiconductor manufacturers.

Bibliography

[1] Q. Cheng, S. Rumley, M. Bahadori, and K. Bergman, “Photonic switching in high performance datacenters [Invited],” *Opt. Express, OE*, vol. 26, no. 12, pp. 16022–16043, Jun. 2018, doi: 10.1364/OE.26.016022.

[2] Y. Shen *et al.*, “Deep learning with coherent nanophotonic circuits,” *Nature Photon*, vol. 11, no. 7, pp. 441–446, Jul. 2017, doi: 10.1038/nphoton.2017.93.

[3] J. M. Arrazola *et al.*, “Quantum circuits with many photons on a programmable nanophotonic chip,” *Nature*, vol. 591, no. 7848, Art. no. 7848, Mar. 2021, doi: 10.1038/s41586-021-03202-1.

[4] X. Zhang, K. Kwon, J. Henriksson, J. Luo, and M. C. Wu, “A large-scale microelectromechanical-systems-based silicon photonics LiDAR,” *Nature*, vol. 603, no. 7900, Art. no. 7900, Mar. 2022, doi: 10.1038/s41586-022-04415-8.

[5] J. Park *et al.*, “All-solid-state spatial light modulator with independent phase and amplitude control for three-dimensional LiDAR applications,” *Nat. Nanotechnol.*, vol. 16, no. 1, Art. no. 1, Jan. 2021, doi: 10.1038/s41565-020-00787-y.

[6] S. Abdollahramezani *et al.*, “Tunable nanophotonics enabled by chalcogenide phase-change materials,” *Nanophotonics*, vol. 9, no. 5, pp. 1189–1241, May 2020, doi: 10.1515/nanoph-2020-0039.

[7] M. Wuttig, H. Bhaskaran, and T. Taubner, “Phase-change materials for non-volatile photonic applications,” *Nature Photon*, vol. 11, no. 8, pp. 465–476, Aug. 2017, doi: 10.1038/nphoton.2017.126.

[8] Z. Fang, R. Chen, J. Zheng, and A. Majumdar, “Non-volatile reconfigurable silicon photonics based on phase-change materials,” *IEEE Journal of Selected Topics in Quantum Electronics*, pp. 1–1, 2021, doi: 10.1109/JSTQE.2021.3120713.

[9] Z. Fang, J. Zheng, A. Saxena, J. Whitehead, Y. Chen, and A. Majumdar, “Non-Volatile Reconfigurable Integrated Photonics Enabled by Broadband Low-Loss Phase Change Material,” *Advanced Optical Materials*, vol. 9, no. 9, p. 2002049, 2021, doi: https://doi.org/10.1002/adom.202002049.

[10] Z. Fang *et al.*, “Ultra-low-energy programmable non-volatile silicon photonics based on phase-change materials with graphene heaters,” *Nat. Nanotechnol.*, pp. 1–7, Jul. 2022, doi: 10.1038/s41565-022-01153-w.

[11] Y. Zhang *et al.*, “Broadband transparent optical phase change materials for high-performance nonvolatile photonics,” *Nature Communications*, vol. 10, no. 1, Art. no. 1, Sep. 2019, doi: 10.1038/s41467-019-12196-4.

[12] W. Dong *et al.*, “Wide Bandgap Phase Change Material Tuned Visible Photonics,” *Advanced Functional Materials*, vol. 29, no. 6, p. 1806181, 2019, doi: 10.1002/adfm.201806181.

[13] D. Pérez *et al.*, “Multipurpose silicon photonics signal processor core,” *Nature Communications*, vol. 8, no. 1, Art. no. 1, Sep. 2017, doi: 10.1038/s41467-017-00714-1.

[14] A. H. Atabaki, A. A. Eftekhar, M. Askari, and A. Adibi, “Accurate post-fabrication trimming of ultra-compact resonators on silicon,” *Opt. Express, OE*, vol. 21, no. 12, pp. 14139–14145, Jun. 2013, doi: 10.1364/OE.21.014139.

[15] P. Arun and A. G. Vedeshwar, “Phase modification by instantaneous heat treatment of Sb2S3 films and their potential for photothermal optical recording,” *Journal of Applied Physics*, vol. 79, no. 8, pp. 4029–4036, Apr. 1996, doi: 10.1063/1.361832.

[16] X. Shuai and W. Shen, “A facile chemical conversion synthesis of Sb2S3 nanotubes and the visible light-driven photocatalytic activities,” *Nanoscale Research Letters*, vol. 7, no. 1, p. 199, Mar. 2012, doi: 10.1186/1556-276X-7-199.

[17] B. Krishnan, A. Arato, E. Cardenas, T. K. D. Roy, and G. A. Castillo, “On the structure, morphology, and optical properties of chemical bath deposited Sb2S3 thin films,” *Applied Surface Science*, vol. 254, no. 10, pp. 3200–3206, Mar. 2008, doi: 10.1016/j.apsusc.2007.10.098.

[18] R. Parize, T. Cossuet, O. Chaix-Pluchery, H. Roussel, E. Appert, and V. Consonni, “In situ analysis of the crystallization process of Sb2S3 thin films by Raman scattering and X-ray diffraction,” *Materials & Design*, vol. 121, pp. 1–10, May 2017, doi: 10.1016/j.matdes.2017.02.034.

[19] J. Zheng *et al.*, “GST-on-silicon hybrid nanophotonic integrated circuits: a non-volatile quasi-continuously reprogrammable platform,” *Opt. Mater. Express, OME*, vol. 8, no. 6, pp. 1551–1561, Jun. 2018, doi: 10.1364/OME.8.001551.

[20] M. Delaney, I. Zeimpekis, D. Lawson, D. W. Hewak, and O. L. Muskens, “A New Family of Ultralow Loss Reversible Phase-Change Materials for Photonic Integrated Circuits: Sb2S3 and Sb2Se3,” *Advanced Functional Materials*, vol. 30, no. 36, p. 2002447, 2020, doi: https://doi.org/10.1002/adfm.202002447.

[21] Z. Fang and University of Oxford, “Investigation into the properties and electrical switching performance of Ge2Sb2Se4Te1,” 2017.

[22] Z. FANG, T. Gu, J. Hu, J. Li, and Y. Zhang, “Gsst and applications in optical devices,” US20180284492A1, Oct. 04, 2018 Accessed: Nov. 12, 2020. [Online]. Available: https://patents.google.com/patent/US20180284492A1/en

[23] J. Komma, C. Schwarz, G. Hofmann, D. Heinert, and R. Nawrodt, “Thermo-optic coefficient of silicon at 1550 nm and cryogenic temperatures,” *Appl. Phys. Lett.*, vol. 101, no. 4, p. 041905, Jul. 2012, doi: 10.1063/1.4738989.

[24] J. Zheng, S. Zhu, P. Xu, S. Dunham, and A. Majumdar, “Modeling Electrical Switching of Nonvolatile Phase-Change Integrated Nanophotonic Structures with Graphene Heaters,” *ACS Appl. Mater. Interfaces*, vol. 12, no. 19, pp. 21827–21836, May 2020, doi: 10.1021/acsami.0c02333.

[25] M. Delaney *et al.*, “Nonvolatile programmable silicon photonics using an ultralow-loss Sb2Se3 phase change material,” *Science Advances*, vol. 7, no. 25, p. eabg3500, Jun. 2021, doi: 10.1126/sciadv.abg3500.

[26] M. Stegmaier, C. Ríos, H. Bhaskaran, C. D. Wright, and W. H. P. Pernice, “Nonvolatile All-Optical 1 × 2 Switch for Chipscale Photonic Networks,” *Advanced Optical Materials*, vol. 5, no. 1, p. 1600346, 2017, doi: https://doi.org/10.1002/adom.201600346.

[27] J. Zheng *et al.*, “Nonvolatile Electrically Reconfigurable Integrated Photonic Switch Enabled by a Silicon PIN Diode Heater,” *Advanced Materials*, vol. 32, no. 31, p. 2001218, 2020, doi: 10.1002/adma.202001218.

[28] H. Zhang *et al.*, “Miniature Multilevel Optical Memristive Switch Using Phase Change Material,” *ACS Photonics*, vol. 6, no. 9, pp. 2205–2212, Sep. 2019, doi: 10.1021/acsphotonics.9b00819.

[29] N. Farmakidis *et al.*, “Plasmonic nanogap enhanced phase-change devices with dual electrical-optical functionality,” *Science Advances*, vol. 5, no. 11, p. eaaw2687, Nov. 2019, doi: 10.1126/sciadv.aaw2687.

[30] P. Hosseini, C. D. Wright, and H. Bhaskaran, “An optoelectronic framework enabled by low-dimensional phase-change films,” *Nature*, vol. 511, no. 7508, Art. no. 7508, Jul. 2014, doi: 10.1038/nature13487.

[31] H. Taghinejad *et al.*, “ITO-Based Microheaters for Reversible Multi-Stage Switching of Phase-Change Materials: Towards Miniaturized Beyond-Binary Reconfigurable Integrated Photonics,” *arXiv:2003.04097 [physics]*, Mar. 2020, Accessed: Jan. 18, 2021. [Online]. Available: http://arxiv.org/abs/2003.04097

[32] K. Kato, M. Kuwahara, H. Kawashima, T. Tsuruoka, and H. Tsuda, “Current-driven phase-change optical gate switch using indium–tin-oxide heater,” *Appl. Phys. Express*, vol. 10, no. 7, p. 072201, Jun. 2017, doi: 10.7567/APEX.10.072201.

[33] Q. Xu, B. Schmidt, S. Pradhan, and M. Lipson, “Micrometre-scale silicon electro-optic modulator,” *Nature*, vol. 435, no. 7040, Art. no. 7040, May 2005, doi: 10.1038/nature03569.

[34] J. Kim, S. Shrestha, M. Souri, J. G. Connell, S. Park, and A. Seo, “High-temperature optical properties of indium tin oxide thin-films,” *Scientific Reports*, vol. 10, no. 1, Art. no. 1, Jul. 2020, doi: 10.1038/s41598-020-69463-4.

[35] T. Kawashima, T. Ezure, K. Okada, H. Matsui, K. Goto, and N. Tanabe, “FTO/ITO double-layered transparent conductive oxide for dye-sensitized solar cells,” *Journal of Photochemistry and Photobiology A: Chemistry*, vol. 164, no. 1, pp. 199–202, Jun. 2004, doi: 10.1016/j.jphotochem.2003.12.028.

[36] H. Liu *et al.*, “Rewritable color nanoprints in antimony trisulfide films,” *Science Advances*, vol. 6, no. 51, p. eabb7171, Dec. 2020, doi: 10.1126/sciadv.abb7171.

[37] C. Ríos *et al.*, “Multi-Level Electro-Thermal Switching of Optical Phase-Change Materials Using Graphene,” *Advanced Photonics Research*, vol. n/a, no. n/a, p. 2000034, doi: 10.1002/adpr.202000034.

[38] N. Youngblood *et al.*, “Broadly-tunable smart glazing using an ultra-thin phase-change material,” *arXiv:1911.02990 [physics]*, Nov. 2019, Accessed: Nov. 06, 2020. [Online]. Available: http://arxiv.org/abs/1911.02990

[39] J. Zhou, J. Zheng, Z. Fang, P. Xu, and A. Majumdar, “Ultra-low mode volume on-substrate silicon nanobeam cavity,” *Opt. Express, OE*, vol. 27, no. 21, pp. 30692–30699, Oct. 2019, doi: 10.1364/OE.27.030692.

[40] C. Sun *et al.*, “Single-chip microprocessor that communicates directly using light,” *Nature*, vol. 528, no. 7583, Art. no. 7583, Dec. 2015, doi: 10.1038/nature16454.

[41] A. H. Atabaki *et al.*, “Integrating photonics with silicon nanoelectronics for the next generation of systems on a chip,” *Nature*, vol. 556, no. 7701, Art. no. 7701, Apr. 2018, doi: 10.1038/s41586-018-0028-z.

[42] M. Stegmaier, C. Ríos, H. Bhaskaran, and W. H. P. Pernice, “Thermo-optical Effect in Phase-Change Nanophotonics,” *ACS Photonics*, vol. 3, no. 5, pp. 828–835, May 2016, doi: 10.1021/acsphotonics.6b00032.

[43] Y. Chen *et al.*, “Large thermal tuning of a polymer-embedded silicon nitride nanobeam cavity,” *Opt. Lett., OL*, vol. 44, no. 12, pp. 3058–3061, Jun. 2019, doi: 10.1364/OL.44.003058.

[44] J. T. Robinson, K. Preston, O. Painter, and M. Lipson, “First-principle derivation of gain in high-index-contrast waveguides,” *Opt. Express, OE*, vol. 16, no. 21, pp. 16659–16669, Oct. 2008, doi: 10.1364/OE.16.016659.

[45] C. Bradac, W. Gao, J. Forneris, M. E. Trusheim, and I. Aharonovich, “Quantum nanophotonics with group IV defects in diamond,” *Nature Communications*, vol. 10, no. 1, Art. no. 1, Dec. 2019, doi: 10.1038/s41467-019-13332-w.

[46] S. Wu *et al.*, “Monolayer semiconductor nanocavity lasers with ultralow thresholds,” *Nature*, vol. 520, no. 7545, Art. no. 7545, Apr. 2015, doi: 10.1038/nature14290.

[47] R. Chen, Z. Fang, J. E. Fröch, P. Xu, J. Zheng, and A. Majumdar, “Broadband Nonvolatile Electrically Controlled Programmable Units in Silicon Photonics,” *ACS Photonics*, vol. 9, no. 6, pp. 2142–2150, Jun. 2022, doi: 10.1021/acsphotonics.2c00452.

[48] T. Y. Teo, M. Krbal, J. Mistrik, J. Prikryl, L. Lu, and R. E. Simpson, “Comparison and analysis of phase change materials-based reconfigurable silicon photonic directional couplers,” *Opt. Mater. Express, OME*, vol. 12, no. 2, pp. 606–621, Feb. 2022, doi: 10.1364/OME.447289.

[49] R. Chen *et al.*, “Non-volatile electrically programmable integrated photonics with a 5-bit operation.” arXiv, Jan. 01, 2023. doi: 10.48550/arXiv.2301.00468.

[50] C. Ríos *et al.*, “Integrated all-photonic non-volatile multi-level memory,” *Nature Photonics*, vol. 9, no. 11, Art. no. 11, Nov. 2015, doi: 10.1038/nphoton.2015.182.

[51] C. Ríos *et al.*, “In-memory computing on a photonic platform,” *Science Advances*, vol. 5, no. 2, p. eaau5759, Feb. 2019, doi: 10.1126/sciadv.aau5759.

[52] C. Ríos *et al.*, “Multi-Level Electro-Thermal Switching of Optical Phase-Change Materials Using Graphene,” *Advanced Photonics Research*, vol. 2, no. 1, p. 2000034, 2021, doi: https://doi.org/10.1002/adpr.202000034.

[53] S. Raoux, F. Xiong, M. Wuttig, and E. Pop, “Phase change materials and phase change memory,” *MRS Bull.*, vol. 39, no. 8, pp. 703–710, Aug. 2014, doi: 10.1557/mrs.2014.139.

[54] D. K. Loke, J. M. Skelton, T. H. Lee, R. Zhao, T.-C. Chong, and S. R. Elliott, “Ultrafast Nanoscale Phase-Change Memory Enabled By Single-Pulse Conditioning,” *ACS Appl. Mater. Interfaces*, vol. 10, no. 49, pp. 41855–41860, Dec. 2018, doi: 10.1021/acsami.8b16033.

[55] C. R. Dean *et al.*, “Boron nitride substrates for high-quality graphene electronics,” *Nature Nanotech*, vol. 5, no. 10, pp. 722–726, Oct. 2010, doi: 10.1038/nnano.2010.172.

[56] L. Wang *et al.*, “One-Dimensional Electrical Contact to a Two-Dimensional Material,” *Science*, vol. 342, no. 6158, pp. 614–617, Nov. 2013, doi: 10.1126/science.1244358.

[57] C. Xiong, D. M. Gill, J. E. Proesel, J. S. Orcutt, W. Haensch, and W. M. J. Green, “Monolithic 56 Gb/s silicon photonic pulse-amplitude modulation transmitter,” *Optica, OPTICA*, vol. 3, no. 10, pp. 1060–1065, Oct. 2016, doi: 10.1364/OPTICA.3.001060.

[58] C. Ríos *et al.*, “Ultra-compact nonvolatile photonics based on electrically reprogrammable transparent phase change materials,” May 2021, Accessed: May 23, 2021. [Online]. Available: https://arxiv.org/abs/2105.06010v1

[59] S. Schuler *et al.*, “High-responsivity graphene photodetectors integrated on silicon microring resonators,” *Nat Commun*, vol. 12, no. 1, p. 3733, Jun. 2021, doi: 10.1038/s41467-021-23436-x.

[60] F. Wang *et al.*, “Gate-Variable Optical Transitions in Graphene,” *Science*, vol. 320, no. 5873, pp. 206–209, Apr. 2008, doi: 10.1126/science.1152793.

[61] V. Sorianello *et al.*, “Graphene–silicon phase modulators with gigahertz bandwidth,” *Nature Photon*, vol. 12, no. 1, pp. 40–44, Jan. 2018, doi: 10.1038/s41566-017-0071-6.

[62] H. Taghinejad *et al.*, “ITO-based microheaters for reversible multi-stage switching of phase-change materials: towards miniaturized beyond-binary reconfigurable integrated photonics,” *Opt. Express, OE*, vol. 29, no. 13, pp. 20449–20462, Jun. 2021, doi: 10.1364/OE.424676.

[63] N. Youngblood *et al.*, “Reconfigurable Low-Emissivity Optical Coating Using Ultrathin Phase Change Materials,” *ACS Photonics*, vol. 9, no. 1, pp. 90–100, Jan. 2022, doi: 10.1021/acsphotonics.1c01128.

[64] H. R. Fallah, M. Ghasemi, A. Hassanzadeh, and H. Steki, “The effect of deposition rate on electrical, optical and structural properties of tin-doped indium oxide (ITO) films on glass at low substrate temperature,” *Physica B: Condensed Matter*, vol. 373, no. 2, pp. 274–279, Mar. 2006, doi: 10.1016/j.physb.2005.11.159.

[65] M. Nisha, S. Anusha, A. Antony, R. Manoj, and M. K. Jayaraj, “Effect of substrate temperature on the growth of ITO thin films,” *Applied Surface Science*, vol. 252, no. 5, pp. 1430–1435, Dec. 2005, doi: 10.1016/j.apsusc.2005.02.115.

[66] B. L. Zhu *et al.*, “Structural, electrical, and optical properties of F-doped SnO or SnO2 films prepared by RF reactive magnetron sputtering at different substrate temperatures

and O2 fluxes," *Journal of Alloys and Compounds*, vol. 719, pp. 429–437, Sep. 2017, doi: 10.1016/j.jallcom.2017.05.193.

[67] A. I. Khan *et al.*, "Ultralow–switching current density multilevel phase-change memory on a flexible substrate," *Science*, vol. 373, no. 6560, pp. 1243–1247, Sep. 2021, doi: 10.1126/science.abj1261.

[68] X. Li *et al.*, "Fast and reliable storage using a 5 bit, nonvolatile photonic memory cell," *Optica, OPTICA*, vol. 6, no. 1, pp. 1–6, Jan. 2019, doi: 10.1364/OPTICA.6.000001.

[69] J. Feldmann *et al.*, "Parallel convolutional processing using an integrated photonic tensor core," *Nature*, vol. 589, no. 7840, pp. 52–58, Jan. 2021, doi: 10.1038/s41586-020-03070-1.

[70] X. Liang *et al.*, "Toward Clean and Crackless Transfer of Graphene," *ACS Nano*, vol. 5, no. 11, pp. 9144–9153, Nov. 2011, doi: 10.1021/nn203377t.

[71] L. Waldecker *et al.*, "Time-domain separation of optical properties from structural transitions in resonantly bonded materials," *Nature Mater*, vol. 14, no. 10, Art. no. 10, Oct. 2015, doi: 10.1038/nmat4359.

[72] T. Tuma, A. Pantazi, M. Le Gallo, A. Sebastian, and E. Eleftheriou, "Stochastic phase-change neurons," *Nature Nanotech*, vol. 11, no. 8, pp. 693–699, Aug. 2016, doi: 10.1038/nnano.2016.70.

[73] M. Wuttig and N. Yamada, "Phase-change materials for rewriteable data storage," *Nature Materials*, vol. 6, no. 11, Art. no. 11, Nov. 2007, doi: 10.1038/nmat2009.

[74] C. J. Chang-Hasnain and W. Yang, "High-contrast gratings for integrated optoelectronics," *Adv. Opt. Photon., AOP*, vol. 4, no. 3, pp. 379–440, Sep. 2012, doi: 10.1364/AOP.4.000379.

[75] K. Koshelev, S. Lepeshov, M. Liu, A. Bogdanov, and Y. Kivshar, “Asymmetric Metasurfaces with High-Q Resonances Governed by Bound States in the Continuum,” *Phys. Rev. Lett.*, vol. 121, no. 19, p. 193903, Nov. 2018, doi: 10.1103/PhysRevLett.121.193903.

[76] Z. Liu *et al.*, “High-Q Quasibound States in the Continuum for Nonlinear Metasurfaces,” *Phys. Rev. Lett.*, vol. 123, no. 25, p. 253901, Dec. 2019, doi: 10.1103/PhysRevLett.123.253901.

[77] B. Zeng, A. Majumdar, and F. Wang, “Tunable dark modes in one-dimensional ‘diatomic’ dielectric gratings,” *Opt. Express, OE*, vol. 23, no. 10, pp. 12478–12487, May 2015, doi: 10.1364/OE.23.012478.

[78] A. C. Overvig, S. Shrestha, and N. Yu, “Dimerized high contrast gratings,” *Nanophotonics*, vol. 7, no. 6, pp. 1157–1168, Jun. 2018, doi: 10.1515/nanoph-2017-0127.

[79] J. Y. Kim *et al.*, “Full 2π tunable phase modulation using avoided crossing of resonances,” *Nat Commun*, vol. 13, no. 1, Art. no. 1, Apr. 2022, doi: 10.1038/s41467-022-29721-7.

[80] M. Lawrence *et al.*, “High quality factor phase gradient metasurfaces,” *Nature Nanotechnology*, vol. 15, no. 11, Art. no. 11, Nov. 2020, doi: 10.1038/s41565-020-0754-x.

[81] J. Zheng *et al.*, “Nonvolatile Electrically Reconfigurable Integrated Photonic Switch Enabled by a Silicon PIN Diode Heater,” *Advanced Materials*, vol. 32, no. 31, p. 2001218, 2020, doi: https://doi.org/10.1002/adma.202001218.

[82] Y. Zhang *et al.*, “Electrically reconfigurable non-volatile metasurface using low-loss optical phase-change material,” *Nat. Nanotechnol.*, vol. 16, no. 6, Art. no. 6, Jun. 2021, doi: 10.1038/s41565-021-00881-9.

[83] Y. Wang *et al.*, “Electrical tuning of phase-change antennas and metasurfaces,” *Nat. Nanotechnol.*, vol. 16, no. 6, Art. no. 6, Jun. 2021, doi: 10.1038/s41565-021-00882-8.

[84] C. Ríos *et al.*, “Ultra-compact nonvolatile phase shifter based on electrically reprogrammable transparent phase change materials,” *PhotoniX*, vol. 3, no. 1, p. 26, Oct. 2022, doi: 10.1186/s43074-022-00070-4.

[85] P. Moitra *et al.*, “Programmable Wavefront Control in the Visible Spectrum Using Low-Loss Chalcogenide Phase-Change Metasurfaces,” *Advanced Materials*, vol. n/a, no. n/a, p. 2205367, doi: 10.1002/adma.202205367.

[86] C. Zhang *et al.*, “Nonvolatile Multilevel Switching of Silicon Photonic Devices with In2O3/GST Segmented Structures,” *Advanced Optical Materials*, vol. n/a, no. n/a, p. 2202748, doi: 10.1002/adom.202202748.

[87] “Webinar: Four Optics Breakthroughs to Power Enterprise AR.” https://www.magicleap.com/webinar-four-optics-breakthroughs-to-power-enterprise-ar (accessed Jan. 13, 2023).

[88] S. S. Saseendran *et al.*, “MoOx: A transparent phase change material for integrated photonics applications?,” in *2022 IEEE Photonics Conference (IPC)*, Nov. 2022, pp. 1–2. doi: 10.1109/IPC53466.2022.9975594.

[89] G. W. Burr *et al.*, “Phase change memory technology,” *Journal of Vacuum Science & Technology B*, vol. 28, no. 2, pp. 223–262, Mar. 2010, doi: 10.1116/1.3301579.

[90] L. Martin-Monier *et al.*, “Endurance of chalcogenide optical phase change materials: a review,” *Opt. Mater. Express, OME*, vol. 12, no. 6, pp. 2145–2167, Jun. 2022, doi: 10.1364/OME.456428.